

# POPULATION SYNTHESIS MODELS FOR IMF STUDIES

Maia Orsi

A thesis submitted in partial fulfilment of the requirements of  
Liverpool John Moores University  
for the degree of  
Doctor of Philosophy.  
July 9, 2014

The copyright of this thesis rests with the author. No quotation from it should be published without his prior written consent and information derived from it should be acknowledged © M. Orsi 2014.

# Declaration

The work presented in this thesis was carried out in the Astrophysics Research Institute, Liverpool John Moores University. Unless otherwise stated, it is the original work of the author.

Whilst registered as a candidate for the degree of Doctor of Philosophy, for which submission is now made, the author has not been registered as a candidate for any other award. This thesis has not been submitted in whole, or in part, for any other degree.

Maia Orsi  
Astrophysics Research Institute  
Liverpool John Moores University  
IC2, Liverpool Science Park  
146 Brownlow Hill  
Liverpool  
L3 5RF  
United Kingdom

March 2014

# POPULATION SYNTHESIS MODELS FOR IMF STUDIES

MAIA ORSI

Submitted for the Degree of Doctor of Philosophy

ASTROPHYSICS RESEARCH INSTITUTE

March 2014

## Abstract

Population synthesis models (PSMs) are fundamental tools to study the star formation history and IMF of unresolved stellar populations using spectral features. This work presents a new set of PSMs constructed using theoretical isochrones and two state-of-the-art synthetic spectral libraries. The BT-Settl and Munari libraries were chosen for their ability to predict the observed values of Lick-type and IMF-sensitive indices in individual stars of the solar neighbourhood. The BT-Settl library was used to sample the cool main sequence stars and the Munari library for the rest of the evolutionary phases. The PSMs cover a range of metallicities with  $[Fe/H]= 0, -1.31$  and  $-1.81$  for scaled-solar and  $\alpha$ -enhanced metal mixtures.

The models were used to study the behaviour of the IMF indices defined in the literature and the results are in good agreement with what other PSMs have determined. The PSMs in this work predict a strong degeneracy between age, metallicity and IMF. I used the models to study which are the main evolutionary phases contributing to each IMF-sensitive index and found that most indices reach their final integrated values before the turn off. The post-main sequence stars contribute mainly to the continuum of these bands. Uncertainties in the the effective temperature of the isochrones can affect IMF estimates.

The PSMs were applied to extragalactic globular clusters (GCs) and early-type galaxies (ETGs) using data from the literature. I determined the ages, metallicities and IMFs of these systems using index combinations in the optical and infrared. I explored

how the morphology of the Horizontal Branch (HB) and dynamical evolution (which are key uncertainties in the modelling of GCs) can affect the IMF predictions. In a population with a Milky Way IMF, dynamical evolution can make the IMF indices mimic a bottom-light IMF. HB morphology has no impact on the IMF estimates at low  $[\text{Fe}/\text{H}]$ . In the IMF index-index diagrams for GCs, the results are significantly affected by the unknown sodium abundances of these systems. Using the PSMs in this work the best index combination to determine the IMF is CaH1 and TiO<sub>2</sub>. The ETGs and the  $[\text{Fe}/\text{H}]=0$  GCs appear to have a bottom-heavy IMF with  $x \sim 3.0$ . These results are discussed in the work.

# **Publications**

The contents of this thesis have not yet been published by the author.

# Acknowledgements

I am very grateful to my two supervisors, Maurizio Salaris and Phil A. James, for their help and guidance throughout these years and especially in the last few months during the writing of this thesis.

I would also like to thank Derek Homier from ENS Lyon who provided me with synthetic spectra that were not originally available and for running the simulations in record time.

I would like to thank so many friends and family with whom I shared discussions, worries, ideas and good times throughout the length of this PhD. Thanks to the beautiful yoga community in Liverpool which trusts me and always helps me to find back the balance. Thanks to Yoel for always reminding me about the art of laughter.



# Contents

<b>Declaration</b>	<b>iii</b>
<b>Abstract</b>	<b>v</b>
<b>Publications</b>	<b>vi</b>
<b>Acknowledgements</b>	<b>vii</b>
<b>Contents</b>	<b>ix</b>
List of Tables . . . . .	x
List of Figures . . . . .	xi
<b>1 Introduction</b>	<b>1</b>
1.1 Galaxy formation . . . . .	1
1.2 Population Synthesis Models . . . . .	3
1.2.1 The ingredients of Population Synthesis Models . . . . .	4
1.2.2 Star Formation Histories . . . . .	11
1.3 The stellar Initial Mass Function . . . . .	12
1.3.1 What is the Initial Mass Function? . . . . .	12

1.3.2	Methods to study the IMF in unresolved stellar populations . . .	15
1.4	Aims of this work . . . . .	21
<b>2</b>	<b>Constructing population synthesis models with theoretical spectral libraries</b>	<b>23</b>
2.1	The choice of stellar isochrones . . . . .	24
2.2	The choice of theoretical spectral libraries . . . . .	25
2.2.1	Comparison with observed stellar spectra in the optical . . . .	28
2.2.2	Comparison with observed stellar spectra in the infrared . . . .	33
2.3	Final choices and the PSMs ingredients . . . . .	41
2.3.1	Final remarks . . . . .	48
<b>3</b>	<b>Behaviour of IMF-sensitive indices in synthetic SSP models</b>	<b>49</b>
3.1	PSM to generate integrated spectra of SSPs . . . . .	50
3.2	Impact of the coverage of the parameter space on the integrated spectra of SSPs . . . . .	52
3.3	Definition of IMF-sensitive indices . . . . .	55
3.4	Contribution from different evolutionary phases . . . . .	61
3.5	Age and metallicity effects . . . . .	63
3.6	The impact of isochrone uncertainties . . . . .	66
3.6.1	Temperature uncertainties . . . . .	66
3.6.2	Stellar evolution predictions . . . . .	70
3.7	Summary and conclusions . . . . .	73
<b>4</b>	<b>Application to globular clusters and early-type galaxies</b>	<b>75</b>

4.1	Tests on globular clusters . . . . .	76
4.1.1	Age and metallicity estimates . . . . .	77
4.1.2	Dynamical evolution of GC: the model perspective . . . . .	86
4.1.3	Index-index plots to explore the IMF of the M31 GCs . . . . .	93
4.2	Comparison with early-type galaxies . . . . .	103
4.2.1	The data . . . . .	104
4.2.2	Age and metallicity estimates . . . . .	104
4.2.3	IMF derivations and comparison to previous studies . . . . .	107
4.3	Summary and conclusions . . . . .	110
<b>5</b>	<b>Summary &amp; Conclusions</b>	<b>112</b>
5.1	Summary . . . . .	112
5.2	Main results and conclusions . . . . .	114
5.3	Future work . . . . .	115
	<b>Bibliography</b>	<b>117</b>

# List of Tables

1.1	Examples of empirical spectral libraries . . . . .	7
1.2	Examples of high-resolution theoretical spectral libraries . . . . .	8
1.3	Early definitions of IR gravity-sensitive features. Wavelength limits are in Å . . . . .	16
2.1	Parameters of the theoretical spectral libraries used in this work. The synthetic spectra are available at very high-resolution, the BT-Settl libraries have R=500,000 in the optical and R=100,000 in the infrared. The Munari library is available at various resolutions and for this work all the spectra have R= 20,000 across the whole wavelength range. . .	26
2.2	Details of the model atmosphere codes used in the synthetic libraries.	27
2.3	The Lick indices. Wavelength limits and resolution are in Å. The indices H $\delta$ and H $\gamma$ have an F and A definitions which correspond to narrower and wider central passband limits, respectively. The index strengths are measured in EW in Å apart from the molecular bands Mg and CN that are measured in magnitudes. <sup>a</sup> Resolution quoted in terms of FWHM. . . . .	32
2.4	The IR indices. Wavelength limits and indices strengths are in Å. References for the index definitions: (1) Spiniello et al. (2012); (2) Conroy & van Dokkum (2012a); (3) Vazdekis et al. (2012); (4) Cenarro et al. (2001); (5) Diaz et al. (1989); (6) Smith et al. (2012). . . . .	37

3.1	The effect produced on individual indices when adding cool giants to a 13.5 Gyr old population with solar metallicity and Salpeter IMF. The indices were measured in high resolution spectra. The values are in Å except for the the TiO and CaH bands that are in magnitudes. . . . .	53
3.2	The percentage contribution at different wavelengths from each evolutionary phase to the total integrated flux of a 13.5 Gyr population with Salpeter IMF and solar metallicity. . . . .	55
3.3	The percentage contribution at different wavelengths from each evolutionary phase to the total integrated flux of a 5 Gyr population with Salpeter IMF and solar metallicity. . . . .	56
3.4	The percentage contribution at different wavelengths from each evolutionary phase to the total integrated flux of a 13.5 Gyr metal poor [Fe/H]= -1.8 population with Salpeter IMF. . . . .	56
3.5	New optical indices defined by Spiniello et al. (2014). . . . .	57
3.6	The main visible isochrone differences between the BaSTI+ and Padova stellar evolution predictions for a 10 Gyr population. . . . .	70
3.7	The percentage change produced when changing a 5 Gyr isochrone from BaSTI+ to the Padova predictions. The values are calculated by computing the difference between the indices produced by each PSM at a given value of the IMF and are normalized by the value from the BaSTI+ PSM. . . . .	71
4.1	Parameters of the M31 globular clusters used in this work as derived by C+2011. Measured ages have an uncertainty $\pm 2$ Gyr. ** Ages could not be determined because the clusters fall outside their PSM grid, see Section ?? . . . . .	79

# List of Figures

- 1.1 Stellar isochrones from the BaSTI database (Pietrinferni et al., 2004) for four ages: 5, 7, 10 and 13.5 Gyr. The different ages become visible at the turnoff point and sub-giant branch (younger ages have a hotter and more luminous turnoff). The different colours denote different metallicities: the black lines have initial solar chemical composition and the blue lines have a lower metal content (at the same age the metal-poor isochrones have hotter temperatures). . . . . 5
- 1.2 Fractional contribution of different evolutionary phases as a function of age to the total bolometric flux in a simple stellar population with solar metallicity. One panel for each photometric band: U, V, I and K. In the optical the main-sequence phase is the main contributor at all ages and towards longer wavelengths the contribution of later evolutionary phases becomes increasingly dominant. Plot from Cassisi & Salaris (2013) . . . . . 6
- 1.3 Theoretical (B–K)-(J–K) diagram for models of varying age and metallicity. Metallicity is constant along the solid lines and increases from left to right (bluer to redder). Age is constant along the dashed lines and increases from bottom to top. The triangles in the metal-rich population indicate the effect of varying the IMF exponent which is shown for the younger and older ages. Plot from James et al. (2006) ©. . . . 12

- 1.4 Grids of  $H\beta$ ,  $[MgFe]$  and Fe5406 for scaled-solar models (solid lines and circles) of varying age and metallicity. Age varies vertically with older ages presenting weaker  $H\beta$  strengths. Metal content varies horizontally and in both plots stronger lines indicate increasing metallicity. Plot from Percival et al. (2009) ©AAS. Reproduced with permission. 13
- 1.5 The plot illustrates various IMF prescriptions from the literature: Salpeter (1955), Miller & Scalo (1979), Kennicutt (1989), Scalo (1986), Kroupa, Tout & Gilmore (1993), Kroupa (2001), Baldry & Glazebrook (2003) and Chabrier (2003). The examples discussed in the text are the Salpeter single-power law (red dotted line), the Kroupa (cyan) and Chabrier (magenta) predictions; the last two with a visible turn-over at lower masses. Image courtesy of Ivan K. Baldry. . . . . 14
- 1.6 Each panel shows the strength of IMF-sensitive features as a function of velocity dispersion. The measurements were done in stacked spectra from a large sample of ETGs and convolved to the same resolution. The shaded region at the side indicates the population synthesis models predictions for a range of ages (between 5 and 10 Gyr) and metallicities. In this case a Salpeter IMF is given by  $\Gamma=1.35$ . The results and plot are from Ferreras et al. (2013)©. . . . . 18

1.7	The sample of ETGs is grouped by velocity dispersion $\sigma$ colour coded as indicated at the top of the diagram. The panels show the comparison between the empirical ( $M/L_{stars}$ ) and the model predictions assuming a Salpeter IMF ( $M/L_{Salp}$ ). If the galaxies were to have a Salpeter IMF they should lie along the magenta line indicating a ratio of observed and modelled values of 1:1. If they were to match a MW IMF they should align with the green and red lines. The most massive galaxies in their sample show the strongest deviations from these predictions. This result can be interpreted as evidence for IMF variations that indicate either a larger amounts of low-mass stars (IMF exponent: $x = -2.8$ ) or of stellar remnants produced by a bigger population of massive stars ( $x = -1.5$ ). Plot and results from Cappellari et al. (2012)©. . . . .	20
2.1	The BaSTI+ isochrones for a 5 Gyr SSP are shown for the three metallicities that will be employed in the following chapters: solar in black and the two sub-solar metallicities in green and blue. . . . .	25
2.2	Coverage of the empirical data and theoretical spectra. The black crosses are the stellar parameters for the spectra used as calculated by Schiavon (2007), the colour symbols represent the synthetic spectra for the three libraries as indicated in the capture of the figure. . . . .	29
2.3	Optical comparison in dwarf stars with $\log g > 3.5$ . Error bars indicate $\pm 50\text{K}$ uncertainty in the effective temperature. . . . .	30
2.4	Optical comparison in giant stars with $\log g \leq 3.5$ . Error bars indicate $\pm 50\text{K}$ uncertainty in the effective temperature. . . . .	31
2.5	IRTF stars and solar metallicity isochrones for ages: 1, 2, 3, 5, 10 and 13.5 Gyr. The error bars indicate $\pm 100\text{K}$ uncertainties in the effective temperature. . . . .	36
2.6	Infrared comparison in dwarf stars with $\log L/L_{\odot} < 0.67$ . Error bars indicate $\pm 50\text{K}$ uncertainty in the effective temperature. . . . .	38

2.7	Infrared comparison in giant stars with $\log L/L_{\odot} \geq 0.67$ . Error bars indicate $\pm 50\text{K}$ uncertainty in the effective temperature. . . . .	39
2.8	Comparison between a theoretical spectrum from the Munari library and an observed stellar spectrum from the MILES library for a K dwarf. The fluxes were normalized at $5000 \text{ \AA}$ . The stellar parameters are detailed in the figure. . . . .	42
2.9	Comparison between a theoretical spectrum from the Munari library and observed stellar spectrum from the MILES library for K giant. The star HD017361 has $[\text{Mg}/\text{Fe}] = -0.09$ . The fluxes were normalized at $5000 \text{ \AA}$ . . . . .	43
2.10	Grid of synthetic spectra and isochrones for $[\text{Fe}/\text{H}] = 0$ with scaled-solar metal mixture (top panel) and $\alpha$ -enhanced abundances (bottom panel). The two spectral libraries are colour coded as indicated in the plots. The four isochrone ages correspond to 5, 7, 10 and 13.5 Gyr (hottest to coolest TO temperature). . . . .	44
2.11	Grid of synthetic spectra and isochrones for $[\text{Fe}/\text{H}] = -1.31$ (top) and $-1.81$ (bottom), both with $[\alpha/\text{Fe}] = +0.4$ . The total metal abundance $[\text{M}/\text{H}]$ is indicated at the top of each panel. The two spectral libraries are colour coded as indicated in the plots. The four isochrone ages correspond to 5, 7, 10 and 13.5 Gyr (hottest to coolest TO temperature). . . . .	45
2.12	A completed version of the grid of synthetic spectra and isochrones shown in Figure ?? for $[\text{Fe}/\text{H}] = 0$ and scaled-solar metal mixture. The additional spectra included in this version of the PSMs are represented by the blue stars at low surface gravity values. The model grid is composed of two libraries colour coded as indicated in the diagram. . . . .	46
2.13	Comparison between BT-Settl and Munari synthetic spectra at $3500 \text{ K}$ and $\log g = 1.0$ at solar metallicity. Both spectra were normalized at $\lambda = 5000 \text{ \AA}$ . . . . .	47

3.1	Examples of SEDs for the whole available spectral range for a 10 Gyr population with $[Fe/H]=0$ , scaled-solar abundances and different IMF exponents denoted by the colours as indicated in the caption. The original resolution was lowered to the approximate resolution of the Lick indices and the flux was normalized to a maximum value of 1. . . . .	51
3.2	The same spectra shown in Figure ?? for a 10 Gyr population with varying IMF zooming in the spectral regions of the optical IMF-sensitive indices. The central passbands are shaded in yellow and the corresponding blue and red continua appear in grey to the left and right sides of the yellow regions respectively. . . . .	58
3.3	The behaviour of optical and infrared indices as a function of IMF exponent for different ages and metallicities. The x-axis indicates the IMF exponent $x$ (Equation ??) except for $x = 1$ that is used to represent the MW Kroupa multi-power law. The ages are colour-coded as labeled and the plus symbols and triangles represent solar and sub solar metallicity populations respectively. The sub-solar metallicity is quoted in terms of total metal abundance $[M/H]$ because it is $\alpha$ -enhanced by +0.4 and this corresponds to a total value of $[Fe/H] \sim -1.31$ . The TiO and CaH bands are measured in magnitudes while all the other indices are in $\text{\AA}$ . . . . .	60
3.4	Fractional contribution of the evolutionary phases to the integrated value of the IMF-sensitive indices. Along the x-axis we plot the upper cut-off mass used to compute the integrated spectra. The maximum mass $0.98M_{\odot}$ accounts for the whole isochrone. The blue dashed line indicates the turnoff mass ( $\sim 0.93 M_{\odot}$ ) and the solid green line indicates the final integrated value obtained when considering the entire isochrone. Only the NaIb definition is plotted here. . . . .	64

3.5	The integrated value of the indices when a change in the temperature of the whole isochrone is applied shown by the plus signs. The temperature uncertainties are reproduced by adding and subtracting 100, 150 and 200K from the original effective temperature ( $T_{eff}$ ) predicted by the isochrone (when $\Delta T_{eff} = 0$ ). Isochrone points with original temperatures below 3700K are not changed. The dotted lines are the integrated values for different shapes of the IMF using the original temperature predictions of the isochrone. . . . .	68
3.6	The integrated value of the indices when changing the temperature of the red giant branch only are shown by the plus signs. Temperature uncertainties were applied to all stars with $\log g \leq 3.0$ by adding and subtracting 100, 150 and 200K from the original effective temperature ( $T_{eff}$ ) predicted by the isochrone ( $\Delta T_{eff} = 0$ ). The dotted lines are the integrated values for different shapes of the IMF using the original temperature predictions of the isochrone. . . . .	69
3.7	The BaSTI+ and Padova Marigo et al. (2008) isochrones at solar metallicity with ages 5, 10, 7 and 13.5 Gyr. The Padova isochrones predict cooler turnoffs and RGB temperatures for all ages. For simplicity the post-AGB phase from the Padova models is not shown here as it is not taken into account in this work. The different minimum mass between libraries is visible at the low mass end of the main sequence. . . . .	71
3.8	The behaviour of the indices as a function of IMF shape in the two PSMs. The BaSTI models are plotted using plus signs and solid lines and the Padova models are indicated with triangles and dashed lines. All PSMs are at solar metallicity and ages colour-coded as indicated. .	72
4.1	Spectral Energy Distributions (SEDs) of the GC sample. The spectra are plotted in three panels corresponding to the different [Fe/H] as derived by C+2011. The GC SED are colour-coded as indicated in the key, where the names are those from C+2011. . . . .	78

- 4.2 Age and metallicity grid predicted by the PSMs compared to the M31 GCs (stars). Each point or square in the grid represents an SSP with a specific age and metallicity and a Kroupa MW-type IMF. The synthetic high-resolution integrated spectra were convolved with a Gaussian with FWHM= 5Å to match the resolution of the GC spectra. The filled circles represent the set of models for scaled-solar abundances available at [Fe/H]= 0.0 and the filled squares are  $\alpha$ -enhanced models for [Fe/H]= 0.0, -1.31, -1.81, where [ $\alpha$ /Fe]= +0.4. The black-dashed lines denote constant age and the colour dotted-dashed lines denote constant metallicity. In the grid, age increases from the top down and metallicity decreases from right to left. The coloured stars represent the measured indices in the M31 clusters and are colour-coded according to their metallicity as estimated by C+2011. The errors were calculated using the program LECTOR (Vazdekis, 2011). For the younger and older ages of each metallicity, I plotted the model predictions for different exponents of the IMF. The circles with the cross in the middle added to the standard grid represent the effect of changing the IMF-exponent to Salpeter,  $x = 3.0$  and  $x = 3.5$ . For all the SSPs as the IMF changes from Kroupa to  $x = 3.5$  the metallicity indicator [MgFe] gets stronger. The effect on H $\beta$  depends on the metallicity. . . . . 81
- 4.3 Fe5406 and [MgFe] plot to study the  $\alpha$ -abundances of the GCs. At fixed [Fe/H], an  $\alpha$ -enhanced population has larger [MgFe] strength than the scaled-solar mixture. The models and clusters are colour-coded as indicated in the Figure. Models with the same metallicity are joined with a line and each point specifies an SSP with a characteristic age and MW-IMF. Older ages always produced larger Fe5406 strengths. 85

4.4	Comparison between the observed spectrum of a solar globular cluster and the modelled spectrum for a 10 Gyr SSP with Salpeter IMF, $[\text{Fe}/\text{H}]=0$ and scaled-solar metallicity. To facilitate the comparison both spectra have been convolved to $10\text{\AA}$ FWHM. The fluxes were normalized at $5000\text{\AA}$ . . . . .	87
4.5	Comparison between the observed spectrum of a metal poor globular cluster and the modelled spectrum for a 10 Gyr SSP with Salpeter IMF and $[\text{Fe}/\text{H}]=-1.0$ . To facilitate the comparison both spectra have been convolved to $10\text{\AA}$ FWHM. The fluxes were normalized at $5000\text{\AA}$ . . .	88
4.6	The effect of dynamical evolution on the IMF-sensitive indices assuming the range of disruption timescales calculated by Kruijssen & Mieske (2009). The black solid line indicates the predicted behaviour at a given disruption time. The colour-lines indicate the value of the indices for the different IMFs without dynamical evolution. . . . .	91
4.7	SEDs for three of the dynamically-evolved 7 Gyr SSPs, colour-coded as indicated in the lower panel. Highlighted in yellow are the central passbands for the indices as indicated in the figure. The adjoining sidebands are highlighted in grey. The original spectra were convolved to a resolution $\text{FWHM}=5\text{\AA}$ . All indices except CaH1, shown here all become stronger as $t_{95\%}$ becomes shorter. . . . .	92
4.8	Optical index-index diagrams used to study the IMF. Each symbol represents an SSP with a given age, metallicity and IMF as indicated in the top panel. The dotted line indicates the effect of dynamical evolution on a 7 Gyr, solar metallicity SSP with Salpeter IMF. The cyan line indicates the effect of a blue HB in a 13.5 Gyr population with $[\text{Fe}/\text{H}]=-1.8$ . . . . .	95

4.9	Infrared index-index diagrams used to study the IMF. Each symbol represents an SSP with a given age, metallicity and IMF as indicated in the top panel. The dotted line indicates the effect of dynamical evolution on a 7 Gyr, solar metallicity SSP with Salpeter IMF. The cyan line indicates the effect of a blue HB in a 13.5 Gyr population, $[\text{Fe}/\text{H}] = -1.8$ for all IMFs. . . . .	97
4.10	Optical index-index diagrams used to study the IMF of the M31 GCs. The models are labeled in the top panel and the clusters are colour-coded as indicated in each plot. The lines join SSPs with the same age and varying IMF. Each symbol from the model grid represents an SSP with a given age, metallicity and IMF as indicated in the top panel. . .	100
4.11	Infrared index-index diagrams used to study the IMF of the M31 GCs. The models are labeled in the top panel and the clusters are colour-coded as indicated in each plot. The lines join SSPs with the same age and varying IMF. Each symbol from the model grid represents an SSP with a given age, metallicity and IMF as indicated in the top panel. . .	102
4.12	NaD and $[\text{MgFe}]$ for the models and clusters colour-coded as indicated in the figure. Models with the same age are joined with a line and each point specifies an SSP with a characteristic age and IMF. Steeper IMF slopes always produce larger NaD values. . . . .	103
4.13	Age and metallicity grid for the sample of ETGs. The data is colour-coded according to the velocity dispersion $\sigma$ and the colour-scheme of the models is indicated in the plot. The circles with the crosses inside indicate the effect of changing the IMF from MW-type to bottom-heavy ( $x = 3.5$ ). . . . .	105
4.14	To study the $\alpha$ -enhancement of the stacks. The colour-scheme of the models is described in the bottom panel. The circles with the crosses inside indicate the effect of changing the IMF from MW-type to bottom-heavy ( $x = 3.5$ ). . . . .	106

4.15 Optical index-index diagrams used to study the IMF of the stacks. The age symbols and colour-scheme of the models are described in the bottom panel. Only  $[Fe/H]=0$  models are shown for scaled-solar and  $\alpha$ -enhanced metal mixtures. The lines join SSPs with the same age and varying IMF. The error bars in the stacks are smaller than the symbol size. . . . . 109

# Chapter 1

## Introduction

### 1.1 Galaxy formation

The preferred cosmological scenario to explain the formation and evolution of cosmic structures is the Cold Dark Matter model with cosmological constant  $\Lambda$  ( $\Lambda$ CDM). The model has been successfully supported by recent spectroscopic observations of Type Ia Supernovae with measurements of their luminosity demonstrating an accelerating cosmic expansion (Riess et al., 1998). Another piece of key evidence was given by measurements of temperature variations in the Cosmic Microwave Background (CMB) radiation (Bennett et al., 2003). The temperature fluctuations imprinted in the CMB can be interpreted as today's signatures of the initial density perturbations that were present in the early universe (redshift  $z \sim 1000$ ) when matter and radiation decoupled. At this moment in time the temperature had dropped sufficiently to enable the growth of primordial inhomogeneities through gravitational instabilities (Silk, 1968).

The initial inhomogeneities are regarded as the seeds of structure formation. In a  $\Lambda$ CDM universe structures grow hierarchically from primordial gravitational instabilities (regions in space that are denser than the surroundings) in a two-fold process. The first stage of this mechanism is a dissipationless growth in which dark matter, which has no pressure and cannot lose energy via electromagnetic interactions, collapses to-

wards denser regions contributing to their growth. The process then evolves into a non-linear aggregation of matter giving rise to the formation of dark matter haloes. Haloes are stable structures supported by the random motions of the particles.

Dark matter haloes continue to grow hierarchically through merging episodes where smaller haloes merge to produce increasingly larger structures. At this stage, dark matter (DM) dominates gravity and baryons start to fall into the large DM haloes. White & Rees (1978) argued that after the DM halo formed through a dissipationless process, a dissipative cooling of the gas must follow to explain the luminous mass of elliptical galaxies and the central bulges of spiral galaxies.

A complete description of the formation and evolution of structures in the universe requires a detailed description of the evolution of the baryons. When the gaseous baryonic matter falls into the potential well it is heated in shocks to the virial temperature of the halo and its pressure prevents further collapse of the DM halo. The gas in the DM halo will eventually cool down through various mechanisms that depend on the local conditions and the temperature of the gas, see e.g. Baugh (2006). Radiative cooling of the baryons and dissipation are needed in order to enable further collapse of the gas that eventually reaches the appropriate conditions for star formation to take place.

One of the major difficulties in modelling from first principles how galaxies form and evolve is related to the physics that drives the evolution of the baryonic component i.e. gas cooling in dark matter haloes, star formation, feedback mechanisms that either remove cold gas from a disk or suppress gas cooling and chemical evolution. Another way to approach this problem and provide independent constraints on the formation and evolution of the luminous component of galaxies is to directly study the stellar populations within. Stellar populations can be regarded as the fossil records of the formation process. We can reveal the assembling history of a galaxy by unfolding the characteristics of the stellar component. In other words, we can study the evolution of the baryonic matter in galaxies by determining its Star Formation History (SFH). The SFH informs us about the distribution of age, chemical composition and stellar mass content of the stellar population.

The amount of evolutionary information we can gather from a stellar population is encoded in the radiation emitted by its stars that add together to produce the total luminosity of the galaxy. A population for which the total luminosity can be broken down into its individual constituents is denoted as “resolved”, while a system from which we can only observe the integrated light we refer to as an “unresolved” stellar population. Theoretical predictions of integrated properties of stellar populations are derived by means of Population Synthesis Models.

## 1.2 Population Synthesis Models

The aim of Population Synthesis Models (PSM) is to predict the integrated flux distribution emitted by a stellar population with an arbitrary SFH (Bruzual & Charlot, 2003). Assuming an age and initial chemical composition we can calculate the theoretical spectral energy distribution of a stellar population by integrating the contributions of the individual stars:

$$F_{\lambda}(t, Z) = \int_{M_l}^{M_u} f_{\lambda}(M, t, Z)_{\star} \Phi(M) dM \quad (1.1)$$

$F_{\lambda}(t, Z)$  represents the integrated flux of the population of age  $t$  and initial chemical composition denoted by the metal mass fraction  $Z$  (see section 1.2.1). The flux of the individual stars is given by  $f_{\lambda}(M, t, Z)_{\star}$ , where  $M$  is the mass of the star. The integration limits are specified by  $M_u$  which is the upper limit of the massive stars still evolving at age  $t$  and  $M_l$  which is the cut-off mass at low masses. The term  $\Phi(M)$  specifies the Initial Mass Function (explained in Section 1.3).

Equation 1.1 is used to compute the integrated flux of a population where all the stars are born at the same time with the same initial chemical composition ( $t$  and  $Z$  are the same for any star); this type of population is dubbed a Simple Stellar Population (SSP). SSP predictions can be used to model more complex populations with an extended star formation history. Analytically, this is the equivalent to a linear combination of SSP models weighted by the star-formation rate (number of stars created per time interval)

and assuming a chemical evolution profile.

The basic principle of PSM is that we can apply the knowledge from stellar evolution and libraries of stellar spectra to predict how a population will appear to us given a certain age and initial conditions (chemical composition and initial mass function). This method was initially developed by Tinsley (1968) and since then has provided a fundamental tool to unravel the properties and assembling history of stellar populations. The work in this thesis presents a new set of PSMs to study the Initial Mass Function (IMF) of stellar populations, focusing on the low-mass star distribution.

The two main ingredients to construct population synthesis models are:

- Stellar isochrones that predict the bolometric luminosity, effective temperature and surface gravity of stars in an SSP
- Stellar spectra which associate each point along the isochrone with a specific flux distribution

### 1.2.1 The ingredients of Population Synthesis Models

#### Stellar Isochrones

An isochrone is a snap-shot of all the stars in an SSP at a given point in time. In an isochrone all the stars have the same age  $t$  and initial chemical composition  $Z$ . For each star in the population, the isochrone predicts the effective temperature, bolometric luminosity and surface gravity. At fixed  $t$  and  $Z$ , the location of a star in the isochrone is determined by its initial mass  $M$ . The number of stars with a characteristic mass is initially determined by the IMF (this topic is further explained in Section 1.3). This information is essential to a population synthesis model in order to assign a flux distribution  $f_\lambda(M, t, Z)_*$  to each star in the SSP.

The position and shape of an isochrone in the Hertzsprung-Russell Diagram (HRD) are specific to the age and chemical composition of the population. The age of the population specifies the temperature of the turnoff point which is the termination of

the hydrogen-burning phase. The chemical composition can shift the whole track along the temperature axis towards cooler or hotter temperatures because the higher the metal content the lower the temperature of the stars. This is illustrated in Figure 1.1.

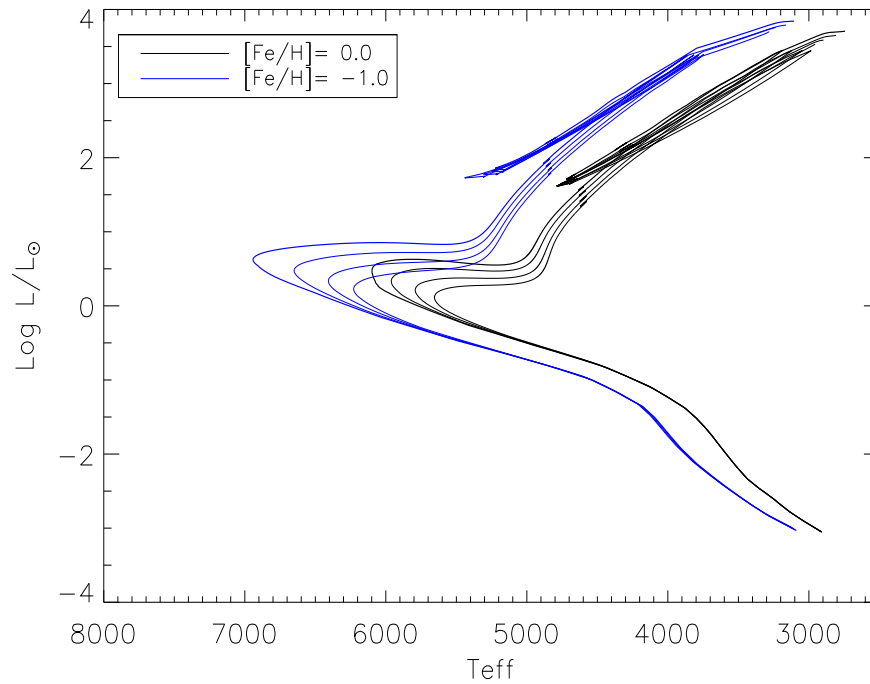


Figure 1.1: Stellar isochrones from the BaSTI database (Pietrinferni et al., 2004) for four ages: 5, 7, 10 and 13.5 Gyr. The different ages become visible at the turnoff point and sub-giant branch (younger ages have a hotter and more luminous turnoff). The different colours denote different metallicities: the black lines have initial solar chemical composition and the blue lines have a lower metal content (at the same age the metal-poor isochrones have hotter temperatures).

The stellar evolutionary phases commonly covered by the isochrone libraries available in the literature are: 1. hydrogen-burning phase or Main Sequence (MS); 2. Sub-Giant Branch (SGB); 3. Red Giant Branch (RGB); 4. core helium-burning phase and 5. Asymptotic Giant Branch (AGB). The contribution of different evolutionary phases to the total flux of a population depends on its age (Figure 1.2).

The choice of the isochrone library to use in the PSM is made according to the best sampling of evolutionary stages and flexibility to cover the parameter space (stellar mass range, SSP ages and chemical composition).

The work in this thesis focuses on old stellar populations, i.e. isochrones older than

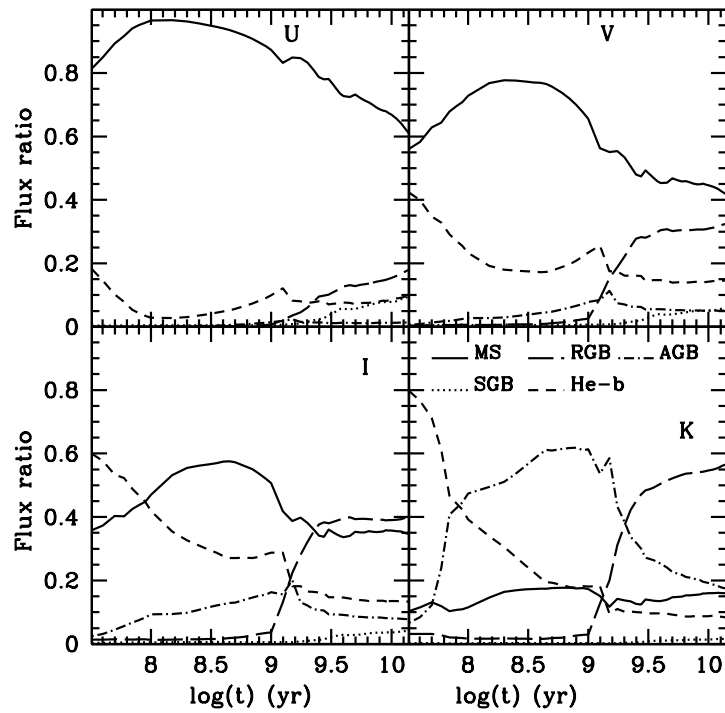


Figure 1.2: Fractional contribution of different evolutionary phases as a function of age to the total bolometric flux in a simple stellar population with solar metallicity. One panel for each photometric band: U, V, I and K. In the optical the main-sequence phase is the main contributor at all ages and towards longer wavelengths the contribution of later evolutionary phases becomes increasingly dominant. Plot from Cassisi & Salaris (2013)

1 Gyr in which only the low-mass stars ( $\leq 2M_{\odot}$ ) are still evolving. The isochrone libraries used in this thesis present up-to-date stellar evolution calculations. The main details are discussed in the next chapter (Section 2.1).

## Spectral Library

Population synthesis models are used to derive the spectral and chemical evolution of a population. The other fundamental ingredient needed to derive spectra, magnitudes and colours from the isochrone predictions is the library of stellar spectra. A library of stellar spectra is a collection of stellar spectra where each spectrum is defined in terms of its surface gravity, effective temperature and metallicity. There are a number of spectral libraries available in the literature and the first choice to make is between empirical and theoretical libraries.

Empirical libraries provide a database of observed stellar spectra. They are an excellent tool to produce integrated spectra of a modelled SSP because they are based on real stars. Examples of some of the most commonly used empirical libraries are given in Table 1.1.

Empirical Library	Spectral range (Å)	Resolution in FWHM (Å)
Miles (Sánchez-Blázquez et al., 2006)	3520 - 7500	2.5
Stelib (Le Borgne et al., 2003)	3200 - 9300	3
IRTF (Rayner et al., 2009)	8000 - 25000	variable, $\lambda/\Delta\lambda=2000$
Indo-US (Valdes et al., 2004)	3460 - 9460	1

Table 1.1: Examples of empirical spectral libraries

Empirical libraries are constructed upon observations of stars in the solar neighbourhood and they provide a restricted coverage of the parameter space (metallicity, temperature and surface gravity). They are the best choice to study stellar populations with properties similar to those found in the solar vicinity (the observed spectra can reproduce accurately the spectral features) but become less accurate for the modelling of populations that have different chemical abundances and enrichment histories, such as giant elliptical galaxies or globular clusters (see also Section 1.2.1) (Worthey et al., 1992).

At the same time and in spite of substantial improvements achieved in the quality of the spectra through increasingly advanced instrumentation, the spectral resolution and wavelength range coverage are intrinsic limitations to empirical libraries. Other systematic errors that would affect the computation of integrated spectra in SSP models based on empirical libraries, are uncertainties in the flux calibration and in the derivation of atmospheric parameters (chemical composition and surface gravities) from observations (Martins & Coelho, 2007).

The other alternative is theoretical spectral libraries that are derived from stellar atmospheric models, which predict the outgoing flux. Examples of some synthetic libraries from the literature are given in Table 1.2

A classical stellar atmosphere model is based on a plane-parallel approximation in hydrostatic equilibrium. Using the equations of hydrostatic equilibrium, radiative transfer

Table 1.2: Examples of high-resolution theoretical spectral libraries

Theoretical Library	Spectral range (Å)	[M/H]	[ $\alpha$ -enhancement]
Munari (Munari et al., 2005)	2500 - 10500	-2.5 to +0.3	yes
Martins (Martins et al., 2005)	3000 - 7000	-1.0 to +0.3	no
MARCS (Gustafsson et al., 2008)	1300 - 20000	-4.5 to +1.0	yes
BT-Settl (Allard et al., 2012)	10 - 25000	-2.5 to +0.5	yes

and an equation of state for the gas, the models are constructed from iterative calculations of the temperature, pressure (gas, electron and radiation), convective velocity and flux distribution at different depths within the atmosphere (Kurucz, 1970). To account for the absorption lines in the emergent flux the models apply a specific treatment of the opacity in the photosphere and selected atomic and molecular line lists.

The main uncertainties of synthetic libraries come from the approximations in the modelling of stellar atmospheres. For example in the treatment of convection according to the mixing-length theory there are a number of free parameters that are introduced to model the physical properties of the gas molecules and their mean-free path (Salaris & Cassisi, 2005). Other assumptions in stellar atmosphere modelling are:

- One-dimensional atmospheres: new 3D models have started to be developed but there is as yet no available spectral library based on them.
- Plane-parallel geometry: this simplification fails to predict realistic models of cool giant stars especially. These stars need to be modelled using spherical symmetry and some new libraries already implement this approach (e.g. BT-Settl, MARCS).
- Local-thermodynamical equilibrium (LTE): this assumption implies that gas and radiation pressure temperature are in equilibrium and neglects atomic transitions by radiation. This simplification becomes less robust when modelling the atmospheres of hotter stars. The solution is to apply non-LTE effects (statistical equilibrium) which numerically is more complex. LTE or N-LTE affect the line broadening parameters of spectral features.

Other uncertainties that play a crucial role in the derivation of theoretical spectra from

model atmospheres are the accuracy of the radiation opacities and completeness of the line-lists.

The main advantage of synthetic spectra is their flexibility: they can be used to compute fluxes for a vast range of stellar masses, temperatures and chemical compositions. We can also overcome the problem of resolution since synthetic spectra are available at very high resolutions and with a continuous wavelength coverage. Theoretical libraries provide the flexibility we need to study the star formation histories of a broad range of stellar populations.

Martins & Coelho (2007) reviewed the advantages and drawbacks of empirical and theoretical libraries. They found that the main flaws of theoretical spectra are seen in the modelling of cool giant stars and generally in the bluer parts of the spectrum. They suggested that improvements in the predictions from theoretical libraries may be achieved from more accurate atomic and molecular line lists.

This thesis explores the use of high-resolution theoretical libraries for population synthesis models. The models in this thesis are based on recent model atmosphere calculations presented in Allard et al. (2012) that are particularly good at representing the atmospheres of low-mass stars. The advantages listed above constitute one of the main motivations for this work.

### **Metallicity**

The chemical composition is a fundamental property of a stellar population that can be used to study its formation process. When we model a stellar population we assume an initial chemical composition for the isochrone and spectral library. At fixed age distribution and IMF, the final integrated spectrum is affected by the initial chemical composition. By comparing observed integrated colours or spectral features of a population with the modelled values we can derive estimates of the initial chemical composition of the population.

From the PSM models perspective, the chemical composition of a population is defined

in terms of  $Z$ . The total chemical composition is given by the fractional contribution of hydrogen  $X$ , helium  $Y$  and the heavy elements (metals)  $Z$ . For each value of  $Z$  the helium mass fraction  $Y$  is calculated using the helium-enrichment ratio  $\Delta Y/\Delta Z \sim 1.4$  obtained using the primordial abundances for  $Y$  and  $Z$  (0.245 and 0, respectively) and the solar initial values ( $Y_{\odot} = 0.28$ ,  $Z_{\odot} = 0.02$ ) (Pietrinferni et al., 2004).

On the other hand, from the observational point of view, the metallicity is generally defined in terms of the iron to hydrogen abundance  $[\text{Fe}/\text{H}]$ . The iron abundance is used as a metallicity indicator since it can be measured relatively easy from the prominent features it produces in the spectra (Salaris & Cassisi, 2005). In the Sun  $[\text{Fe}/\text{H}] = 0$  by definition and if the same heavy-element distribution applies (scaled-solar) the  $[\text{Fe}/\text{H}]$  ratio can be computed as follows:

$$[\text{Fe}/\text{H}] = \log(Z/X)_{\star} - \log(Z/X)_{\odot} \quad (1.2)$$

At fixed metal content  $Z$  the metal mixture can have a different distribution than solar. This is the case of  $\alpha$ -enhanced metallicities typical of old stellar populations in which larger abundance ratios of the  $\alpha$  elements (O, Ne, Mg, Si, S, Ca and Ti) with respect to iron are seen.

Supernova events are believed to be the main contributors to the metal content of the interstellar medium from which stars are formed. The  $\alpha$ -elements are mainly produced by short-lived massive stars in type II supernovae events. On the other hand, the main production of iron-peak elements is during supernovae type Ia events produced in binary systems and which require longer timescales since at least one of the stars has to evolve into a white dwarf. The difference in the production timescales of the elements together with their abundances can be used to trace back the formation timescale of a stellar population. Populations that have low metal content and  $\alpha$ -enhanced metallicities are believed to have formed their stars in a quick and early burst during their evolution. The  $\alpha$ -enhancement increases linearly with decreasing metallicity.

For  $\alpha$ -enhanced metal mixtures we can define the total metal abundance  $[M/H]$ :

$$[M/H] \approx [Fe/H] + \log(0.694 \times 10^{(\alpha/Fe)} + 0.306) \quad (1.3)$$

In this thesis metallicities other than solar will be referred to in terms of  $[M/H]$  which is the way theoretical spectra are labelled.

## 1.2.2 Star Formation Histories

The main purpose of population synthesis models is to constrain star formation histories (SFHs). PSMs constitute a fundamental tool to interpret the observed colours and spectral energy distributions of unresolved stellar populations. Using the predicted integrated flux it is possible to identify combinations of broadband colours, e.g. James et al. (2006), or individual absorption features (Worthey, 1994) that are sensitive to the age and initial chemical composition of the underlying unresolved stellar component. A fundamental problem in the study of SFH is the degeneracy among certain parameters of the population on the final observed properties. Many colours and absorption features respond in a similar way to changes in the age and metallicity, which is known as the age and metallicity degeneracy. In order to derive accurate SFH it is mandatory to use combinations of colours and spectral features that can disentangle age and metallicity effects.

An example of a good combination of colours that can break the age-metallicity degeneracy is shown in Figure 1.3. (B–K) is very sensitive to the age of the population and mildly sensitive to the metallicity, whereas (J–K) is very sensitive to the metallicity of the stars. This is a good combination to disentangle these two effects because the response to changes in age and metallicity are approximately orthogonal to each other. Another example using absorption line features is shown in Figure 1.4 where  $H\beta$  is used to trace the age of the population and  $[MgFe]$  and Fe5406 are employed as good indicators of the metallicity of the population.

By comparing the predicted colours and spectral features to the observed values it is

possible to derive the SFH (age, chemical composition and, as it will be explained later, the initial stellar mass function) of galaxies and stellar clusters that put strong constraints on their formation mechanisms.

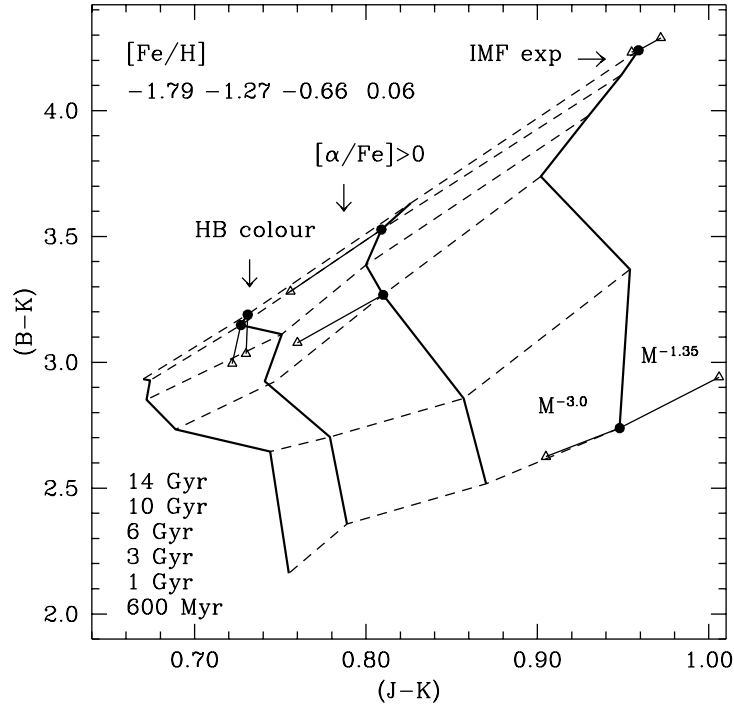


Figure 1.3: Theoretical (B–K)–(J–K) diagram for models of varying age and metallicity. Metallicity is constant along the solid lines and increases from left to right (bluer to redder). Age is constant along the dashed lines and increases from bottom to top. The triangles in the metal-rich population indicate the effect of varying the IMF exponent which is shown for the younger and older ages. Plot from James et al. (2006) ©.

## 1.3 The stellar Initial Mass Function

### 1.3.1 What is the Initial Mass Function?

The Initial Mass Function (IMF) is essential to the modelling of stellar populations. In order to compute the integrated flux of a population (Equation 1.1) the modeller needs to adopt some prescribed form of the IMF. The IMF determines the number of stars in a mass interval ( $M, M + dM$ ) born during a single episode of star formation. It is a fundamental ingredient for the modelling of SSP and it is crucial to determine the

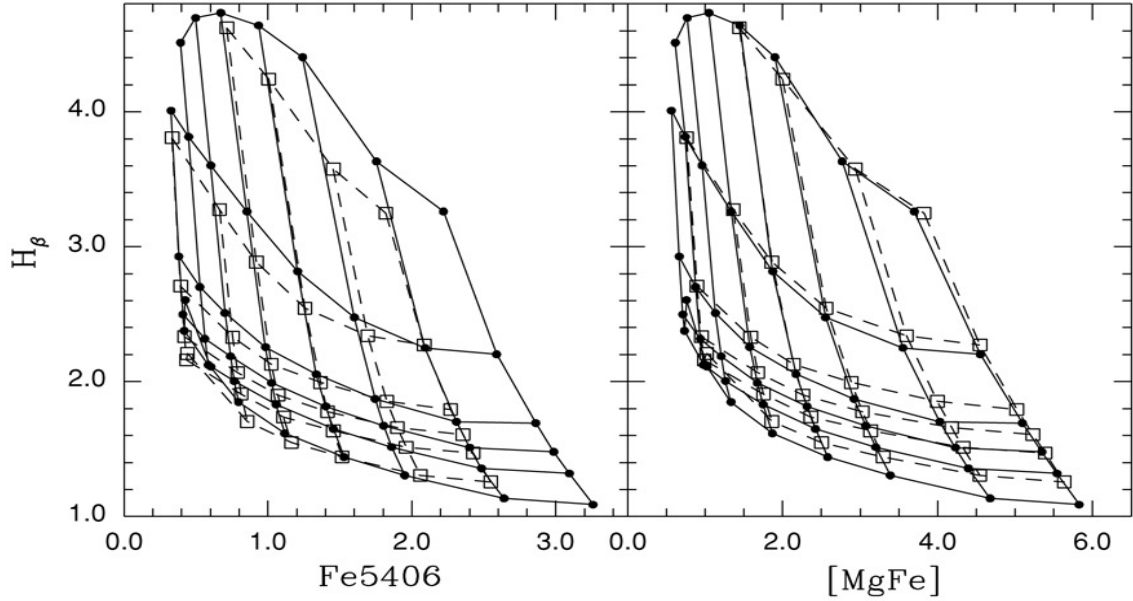


Figure 1.4: Grids of  $H\beta$ ,  $[MgFe]$  and  $Fe5406$  for scaled-solar models (solid lines and circles) of varying age and metallicity. Age varies vertically with older ages presenting weaker  $H\beta$  strengths. Metal content varies horizontally and in both plots stronger lines indicate increasing metallicity. Plot from Percival et al. (2009) ©AAS. Reproduced with permission.

chemical enrichment of the interstellar medium (Kennicutt, 1998). The IMF together with the evolutionary timescales given by the theory of stellar evolution will determine the fraction of stars evolving at specific locations along the isochrone. This means that the IMF will effectively determine the predicted luminosity and chemical enrichment of a stellar population by specifying the number of stars that evolve into the AGB phase and explode as supernovae.

The shape of the IMF cannot be derived from first principles because of a lack of well established theories of star formation. The IMF is an empirical function that can be measured locally by performing star counts of field stars or resolved stellar systems. Using relationships derived from stellar evolution between mass, age and luminosity it is possible to derive mass estimates from the absolute luminosities of the stars. Salpeter (1955) pioneered this technique by counting the number of field stars per mass interval present in a volume of space. He came up with the first definition of the Galactic mass function described as a power-law:

$$dN = cm^{-x}dm \quad (1.4)$$

where  $dN$  is the number of stars born with mass  $m$  in the interval  $m + dm$  and  $c$  is a normalization constant. In the Salpeter case  $x = 2.35$ .

After the first IMF formulation it was suspected that the mass function could not be described by a single power-law across all mass intervals. In the last three decades a lot of effort has been devoted to constrain the shape of the IMF further and improvements have been made towards the low-mass regime below  $1M_{\odot}$ . Several new estimates have been published (see Figure 1.5) culminating with the works of Kroupa (2001) and Chabrier (2003). These works replace the Salpeter IMF by a multi-segment power law and an exponential functional form respectively. They both essentially predict a turn-over at lower masses with shallower slopes for stars below  $0.8M_{\odot}$  (Figure 1.5). These two are the most popular prescriptions currently used in the literature and the difference between their overall predictions is negligible within observational errors (Dabringhausen et al., 2008).

In this work I will refer to the Kroupa (2001) IMF as the Milky Way type IMF. The Milky Way (MW) IMF is described by a variation of  $x$  in Equation 1.4 with respect to the mass interval under consideration:

$$x_0 = 0.3, 0.01 \leq m/M_{\odot} < 0.08$$

$$x_1 = 1.3, 0.08 \leq m/M_{\odot} < 0.5$$

$$x_2 = 2.3, 0.5 \leq m/M_{\odot}$$

The importance of accurate IMF determinations should also be highlighted from the star formation perspective. Correct understanding of the behaviour of the IMF in different scenarios can be used to study the physics of star formation. For many decades researchers have been studying possible IMF variations as a function of environment (metallicity, density) by performing star-counts in stellar clusters. In comparison to field stars, cluster stars are believed to have little spread in their ages and metallicities which makes them ideal targets for the study of the IMF. Numerous studies have been done in young and old clusters in our galaxy and the local group [e.g. Sagar (2002); De Marchi et al. (2010); see Bastian, Covey & Meyer (2010) for a comprehensive review

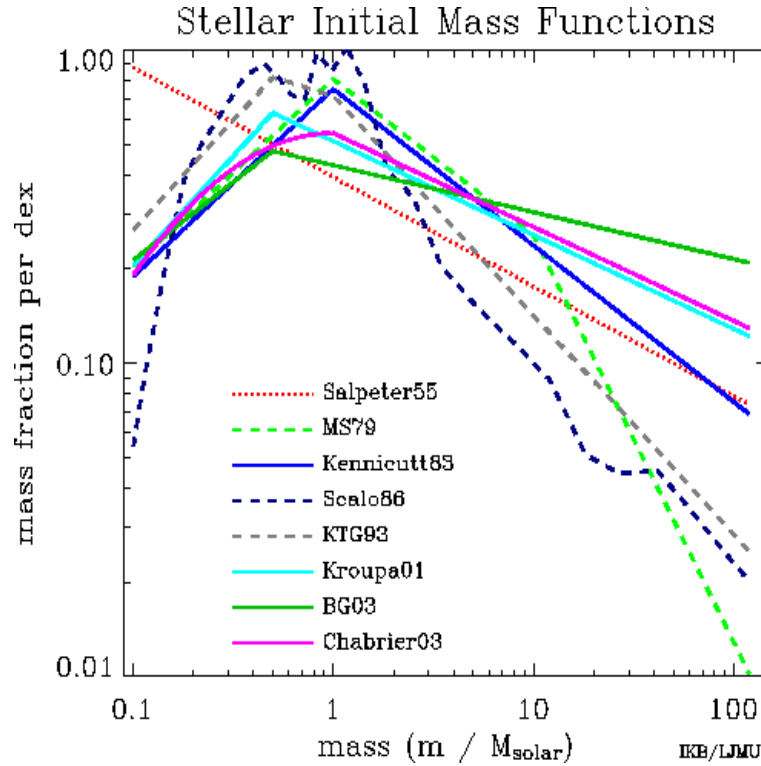


Figure 1.5: The plot illustrates various IMF prescriptions from the literature: Salpeter (1955), Miller & Scalo (1979), Kennicutt (1989), Scalo (1986), Kroupa, Tout & Gilmore (1993), Kroupa (2001), Baldry & Glazebrook (2003) and Chabrier (2003). The examples discussed in the text are the Salpeter single-power law (red dotted line), the Kroupa (cyan) and Chabrier (magenta) predictions; the last two with a visible turn-over at lower masses. Image courtesy of Ivan K. Baldry.

of many recent studies in the nearby universe]. These IMF studies in cluster environment perform stellar counts to determine the present-day mass function (PDMF). The cluster IMF can then be inferred from the PDMF by taking into account the effects of dynamical evolution (mass segregation in tidal environments and consequential loss of low-mass stars) and the age of the cluster. Although some studies have detected variations from the field mass function (represented by a Salpeter, Kroupa or Chabrier IMF), most deviations can also be explained by uncertainties and biases in the data: sample incompleteness, systematic errors in the observations, unknown dynamical evolution of the cluster, unresolved binaries (Scalo, 2004). In spite of these findings there is as yet no substantial evidence for systematic variations of the IMF in the local group.

Measurements of the mass function from stellar counts is a difficult technique limited to Galactic star clusters and extragalactic systems in the local group (and even these

systems pose observational difficulties, especially for low luminosity stars). Alternative ways to study the IMF in distant unresolved systems involve the use of population synthesis models.

### 1.3.2 Methods to study the IMF in unresolved stellar populations

When we model a stellar population we make an *a priori* assumption of the functional form of the IMF. Spectroscopic observations and dynamical-mass measurements from unresolved stellar populations can be used to constrain the IMF by comparing against predictions from population synthesis models of known IMF.

#### Absorption features in near-infrared spectra

One way to study the IMF in unresolved stellar populations is to look for signatures of the stellar mass in the integrated light. It has been known for many decades that there are a series of near-infrared spectral indices dubbed “gravity-sensitive features” that can be used to study the ratio of giant-to-dwarf stars in a population. These near-infrared features (Table 1.3) are sensitive to the temperature and luminosity of the stars which effectively tell us about their masses. Using the dwarf-sensitive absorption lines it is possible to probe the fraction of low-mass stars in a population which, despite dominating the mass budget, contribute very little to the total integrated flux and therefore are hard to quantify. This method presents great potential to study one of the fundamental problems in astronomy: what fraction of the stellar mass in a population is in the form of low-mass stars. The main caveat of this approach is that the indices are also sensitive to the metallicity and age of the stars. In order to derive IMF estimates using this technique it is necessary to place strong constraints on the other parameters of the population.

The first studies to use this technique date back to the seventies, e.g. Spinrad & Taylor (1971), Cohen (1978), Faber & French (1980) and references therein. These studies measured the near-infrared (NIR) features in the galactic nuclei of M31 and M32 and

Table 1.3: Early definitions of IR gravity-sensitive features. Wavelength limits are in Å

Spectral feature	Blue continuum	Central passband	Red continuum	Indicator
NaI doublet	8169 - 8171	8172 - 8209	8209 - 8211	dwarfs
TiO <sub>1</sub>	8350 - 8400	8450 - 8700	8750 - 8800	giants
CaII triplet	8637 - 8646	8653 - 8668	8847 - 8854	giants
FeH (Wing-Ford band)	9891 - 9895	9895 - 9958	9958 - 9962	dwarfs

compared them to observed values in local stars and model predictions. Spinrad & Taylor (1971) found strong NaI lines in the nucleus of M31 and interpreted this result to be a signature of a dwarf-enriched population. Cohen (1978) also measured strong NaI features in the centre of M31 in comparison to M32 but concluded it was due to a metallicity enhancement. Faber & French (1980) agreed with Cohen in that the nucleus of M31 is significantly metal-rich in comparison to M32 but found that the observed NaI strengths could not just be due to metallicity effects and could also be indicating an excess of M dwarfs. Carter et al. (1986) repeated the experiment for a larger sample of nearby giant elliptical galaxies over larger radial distances from the centre of the galaxy. In agreement with previous studies they found that NaI was strong in the galactic centres and decreased towards larger radii. They explained the observed NaI gradient as a metallicity-gradient and although they did not rule out a gradient in the dwarf mass fraction, they could not resolve these two effects from their data.

The first attempts of using gravity-sensitive features as IMF indicators were limited by the shortcomings of the data and the models. The observations and models available at the time were not able to break the degeneracy between dwarf-enriched populations, metallicity and age effects. The technique was later reviewed by Schiavon et al. (2000) who studied the behaviour of the NIR indices in the context of population synthesis models. They constructed stellar population models using high-resolution theoretical spectra and confirmed trends between index strengths, age, metallicity and IMF exponent. They highlighted the need of optical features to break the age, metallicity and IMF degeneracy.

After over three decades of the spectral studies performed in M31 and M32, the technique picked up increasing interest again with a recent investigation by van Dokkum

& Conroy (2010). They studied a sample of four massive early-type galaxies (ETGs) in the Virgo cluster using NaI and FeH features as IMF indicators. They compared the observed index strengths with predictions from a new set of population synthesis models and found their measured values to match model predictions for a dwarf-enriched population. van Dokkum & Conroy took these results as evidence of IMF variations in massive ETGs but did not provide any constraints on the age and metallicity of the galaxies.

In a later paper Conroy & van Dokkum (2012a) (from now on CvD12) presented their new set of population synthesis models based on the IRTF empirical library. This publication has triggered numerous IMF investigations in larger samples of ETGs, e.g. Spiniello et al. (2012); Conroy & van Dokkum (2012b); Smith et al. (2012); and references therein. At the same time Vazdekis et al. (2012) developed MIUSCAT which is another set of population synthesis models that can be used to study the IMF, e.g. Ferreras et al. (2013). MIUSCAT is based on a combination of empirical spectral libraries.

The more recent IMF studies use the NIR features to explore the dwarf population and optical indices from the Lick system to derive metallicities and ages (Worthey et al., 1994). There has been substantial effort devoted to remove the age and metallicity degeneracies by exploring different index combinations that can disentangle these effects. Many of these results [Spiniello et al. (2012); Conroy & van Dokkum (2012b); Ferreras et al. (2013); Spiniello et al. (2014)] have found a correlation between galaxy mass, or velocity dispersion  $\sigma$ , and the fraction of dwarf stars. Recent results suggest that the most massive elliptical galaxies host larger fractions of low-mass stars (an example of these findings is in Figure 1.6).

The work presented in this thesis aims to construct population synthesis models for this type of study. The main difference between the models presented in this work and those already available in the literature (MIUSCAT and Conroy & van Dokkum (2012a)) is the use of theoretical spectral libraries. Although this was first done by Schiavon et al. (2000) recent developments in theoretical model atmospheres, especially in the low-mass regime (Allard et al., 2012), were a motivation to repeat this experiment with

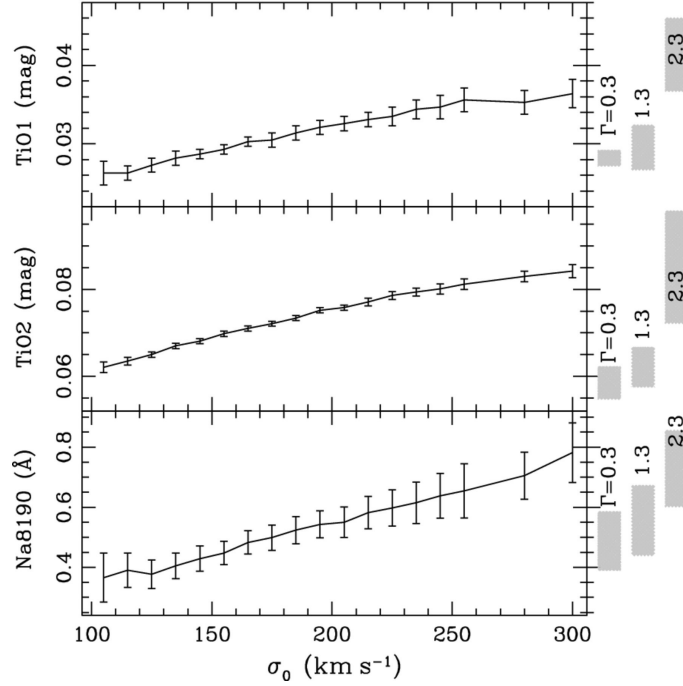


Figure 1.6: Each panel shows the strength of IMF-sensitive features as a function of velocity dispersion. The measurements were done in stacked spectra from a large sample of ETGs and convolved to the same resolution. The shaded region at the side indicates the population synthesis models predictions for a range of ages (between 5 and 10 Gyr) and metallicities. In this case a Salpeter IMF is given by  $\Gamma=1.35$ . The results and plot are from Ferreras et al. (2013)©.

state-of-the-art synthetic spectral libraries.

### Dynamical Mass-to-Light ratios

Another way to study the IMF in unresolved stellar populations that involves the use of population synthesis models is to use the mass-to-light ratios derived from observations and compare them with model predictions. The empirical  $(M/L)_{Dyn}$  can be obtained by measuring the dynamical mass of a stellar population from its kinematics. The modelled  $(M/L)_{PSM}$  is obtained by integrating the IMF along the whole mass range of the isochrone. The comparison can be used to estimate the IMF of the unresolved stellar component by matching it with the results from population synthesis models of known IMF.

Under the assumption of a universal initial mass function described by either a Kroupa

or Salpeter IMF, observed mismatches between the empirical mass-to-light ratios and the predicted values from the models, namely when  $(M/L)_{Dyn} \geq (M/L)_{PSM}$ , can be attributed to larger dark matter fractions (Treu et al., 2010). Considering the recent suggestions that the IMF might not be universal, numerous studies have interpreted mismatches between the empirical and modelled mass-to-light ratios to study possible IMF variations, e.g. Treu et al. (2010); Cappellari et al. (2012); Dutton et al. (2012), and references therein.

An example of this method is shown in Figure 1.7 with the results from Cappellari et al. (2012). In this work they obtained kinematics for a sample of 260 ETGs and fitted the data (stellar distribution and kinematics) to six dynamical models which include a stellar component and spherical dark matter halo. The unknown profile of the dark matter halo constitutes one of the main uncertainties of this method. To explore this issue they employed various halo models with different dark matter density profiles, some of which were constructed to fit the data and others that were derived from pure numerical simulations, such as the commonly used NFW profile (Navarro, Frenk & White, 1996). They derived mass-to-light ratios for the galaxy sample for each of the dynamical models (shown in the panels of figure 1.7) and found similar trends of varying IMF with increasing galaxy mass for all the halo assumptions of dark matter mass fraction and density profile.

This method to study the IMF cannot be used to determine the specific shape of the initial mass function. Apart from the intrinsic uncertainties introduced by the unknown profile and mass of the dark matter halo, the other main limitation of this method is that it cannot distinguish between a giant-rich population (a “top-heavy” IMF where the *invisible* mass is in the form of stellar remnants) from a dwarf-enriched population (“bottom-heavy” IMF where most of the mass is in the form of dwarf stars that do not contribute much to the luminosity).

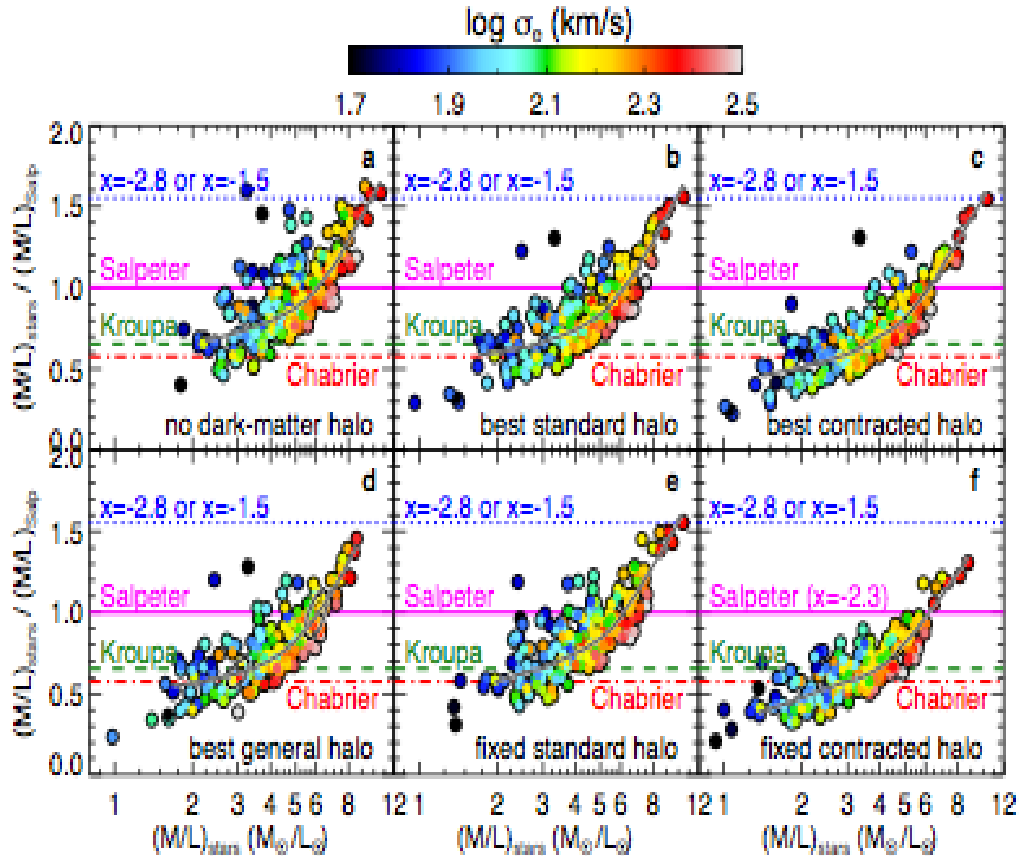


Figure 1.7: The sample of ETGs is grouped by velocity dispersion  $\sigma$  colour coded as indicated at the top of the diagram. The panels show the comparison between the empirical  $(M/L)_{stars}$  and the model predictions assuming a Salpeter IMF  $(M/L)_{Salp}$ . If the galaxies were to have a Salpeter IMF they should lie along the magenta line indicating a ratio of observed and modelled values of 1:1. If they were to match a MW IMF they should align with the green and red lines. The most massive galaxies in their sample show the strongest deviations from these predictions. This result can be interpreted as evidence for IMF variations that indicate either a larger amounts of low-mass stars (IMF exponent:  $x = -2.8$ ) or of stellar remnants produced by a bigger population of massive stars ( $x = -1.5$ ). Plot and results from Cappellari et al. (2012)©.

## **1.4 Aims of this work**

The principal aim of this work is to construct population synthesis models using libraries of synthetic spectra to employ in IMF studies like those described in Section 1.3.2. This study has the intention of providing a better understanding of theoretical spectra for population synthesis models for IMF studies.

The next chapter tests the suitability of three state-of-the-art theoretical spectral libraries, two of which have not been used before in the context of population synthesis models, by comparing them with observations of stars in the solar neighbourhood.. Theoretical spectra provide more flexibility to cover the parameter space in comparison to empirical libraries which can be more limited (ranges of stellar mass and metallicities). Chapter 2 describes the ingredients of the models, isochrones and spectral library.

With PSMs it is interesting to study the effects of changing the ingredients on the final predictions. In Chapter 3 I explore the behaviour of the IMF sensitive indices as a function of age and metallicity and the contribution of the different evolutionary phases to the final integrated values of these indices. The effects of changing the library of stellar isochrones will be considered.

In Chapter 4 I use the models to analyse spectra of globular clusters in M31 and a large sample of ETGs. This chapter also includes a comparison to predictions derived with other PSMs from the literature. A summary and final conclusions are included in Chapter 5.

## **Chapter 2**

# **Constructing population synthesis models with theoretical spectral libraries**

In this chapter I describe the main ingredients used to construct the population synthesis models presented in this work and what motivated these choices. The library of stellar isochrones employed provides a suitable coverage of the parameter space (stellar mass, temperature, luminosity and chemical composition) to use in population synthesis models and their predictions have been tested successfully against observations of individual stars or clusters.

The theoretical spectral libraries were chosen again to cover the required ranges of effective temperature and metallicity, and their capacity to represent their empirical counterpart. To assess the accuracy of the synthetic spectral libraries I studied the behaviour of line indices in the optical and infrared wavelengths. In this chapter I present comparisons between theoretical and empirical spectra. The empirical spectra were taken from the literature and the stellar parameters corresponding to each spectrum (necessary to find their theoretical counterpart) were either obtained from the literature or derived using colour-transformations or stellar evolution theory. The chapter concludes with the final choices made based on the results found.

## 2.1 The choice of stellar isochrones

The main purpose of this new set of population synthesis models is to study the IMF with especial interest in the mass function at lower masses. For this reason the best isochrones to use in this work should be able to sample the low main sequence stars towards the coolest temperatures.

The preferred choice of isochrones for this work is a combination of BaSTI evolutionary tracks (Pietrinferni et al., 2004) for all masses above  $0.5M_{\odot}$  together with Cassisi et al. (2000) for the range between  $0.5$  and  $0.1M_{\odot}$ . I call this combination BaSTI+. The isochrones are available at scaled-solar metallicities  $[M/H]=0, -1.0$  and  $-1.5$ . This work focuses on old stellar populations with isochrone ages of 5, 7, 10 and 13.5 Gyr. Some examples of BaSTI+ are plotted in Figure 2.1.

BaSTI isochrones are available for a wide range of chemical compositions and ages and they were constructed using the latest updates in stellar physics (radiative opacities, equation of state). They have been successfully tested against empirical CMDs in Pietrinferni et al. (2004). They compared the isochrone colour predictions to observations of main sequence dwarf stars from the solar neighbourhood with estimated distances, covering a range in metallicity:  $-0.35 \leq [Fe/H] \leq +0.36$ . For larger samples of stars they used Galactic open clusters (the Hyades, NGC2420, M67, NGC188) for which they had estimates of the reddening, metallicity and distance modulus. In both cases they found good agreement between the theoretical colour predictions and the empirical CMDs.

Cassisi et al. (2000) calculated models for very low mass stars using state-of-the-art stellar physics. They constructed isochrones and tested their predictions against CMDs of low mass stars in Milky Way globular clusters for a range of metallicities. They found good agreement between model predictions and the observed colours of the stars.

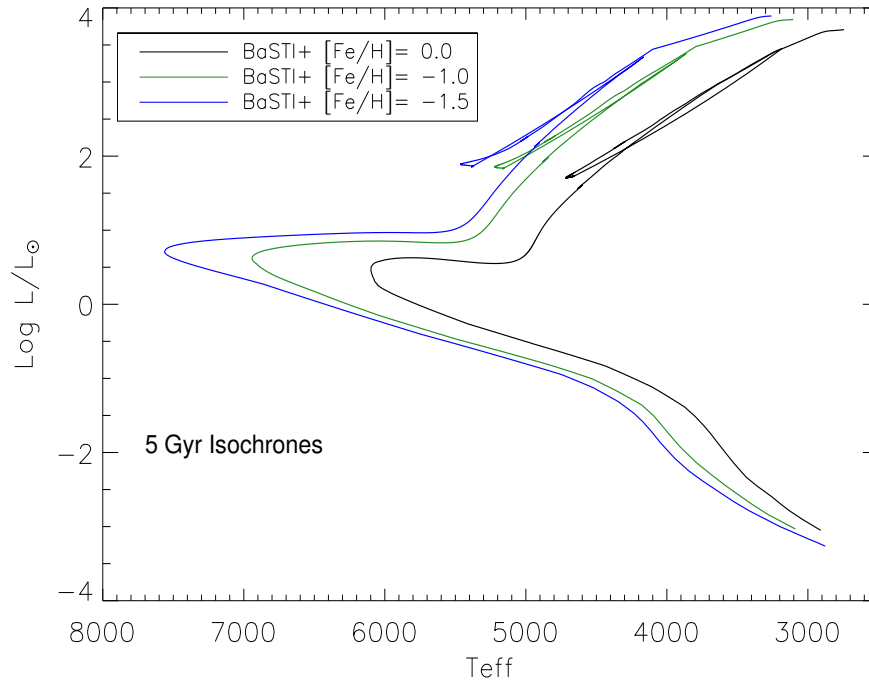


Figure 2.1: The BaSTI+ isochrones for a 5 Gyr SSP are shown for the three metallicities that will be employed in the following chapters: solar in black and the two sub-solar metallicities in green and blue.

## 2.2 The choice of theoretical spectral libraries

The two spectral libraries that constitute the core of this work are Munari et al. (2005) and BT-Settl (Allard et al., 2012). The main details of the parameter space they cover appear in Table 2.2. The Munari spectral library has been used in population synthesis models by Percival et al. (2009) who produced fully synthetic PSMs using BaSTI isochrones and tested them against observations of an extensive sample of resolved Galactic globular clusters. They employed metallicity estimates from spectroscopy and ages from fitting theoretical isochrones to the observed CDMs and compared these results with the model predictions. They found good agreement between the observed values and model predictions. Their study focused in the optical regime (3350-6430 Å) whereas this present work extends the range towards the near infrared wavelengths.

The BT-Settl libraries are well known to be the best available libraries to model the spectra of very low mass stars. There are two versions of the BT-Settl spectral library:

Library	Teff	Log g	[M/H]	Spectral range (Å)
Munari et al. (2005)	3500 - 47000	0.0 - +5.0	-2.5 - +0.5	2500 - 10500
BT-Settl (Allard et al., 2012) GVS	2500 - 12000	-0.5 - +5.5	-2.5 - +0.5	500 - 55000
BT-Settl (Allard et al., 2012) CAF	2500 - 12000	+0.5 - +6.0	-2.5 - +0.5	500 - 55000

Table 2.1: Parameters of the theoretical spectral libraries used in this work. The synthetic spectra are available at very high-resolution, the BT-Settl libraries have  $R=500,000$  in the optical and  $R=100,000$  in the infrared. The Munari library is available at various resolutions and for this work all the spectra have  $R=20,000$  across the whole wavelength range.

the BT-Settl GVS based on Grevesse et al. (1993) solar abundances and the latest version, BT-Settl CAF that uses abundances from Caffau et al. (2011). Apart from the solar abundances assumed, the other main difference between these two versions is the model atmosphere code. The BT-Settl CAF is the most recent version of the library computed under an improved model atmosphere code that adopts the latest input physics and opacities (Allard et al., 2011, 2012). For this work however, it was also possible to compute *new* spectra just for the dwarf stars using the latest physics and GVS solar abundances. The spectra were calculated through the online Phoenix web simulator (<http://phoenix.ens-lyon.fr/simulator/index.faces>) after private communication with F. Allard. This has enabled us to explore the effect of using the latest code on the synthetic spectra.

The BT-Settl libraries have been used to derive stellar parameters of M dwarfs in the solar neighbourhood showing good matches between observed and modelled spectra (Rajpurohit et al., 2012, 2013). In spite of being the best available models for very low mass stars, neither of the two versions of the BT-Settl library have ever been applied in population synthesis models. This was a main motivation to experiment with these libraries in the context of population modelling, since this work is especially concerned with the low mass star fraction in a population.

To study the accuracy of the synthetic libraries I compared measurements from absorption line indices in the theoretical spectra with those observed in single stars. The empirical spectra were obtained from Schiavon (2007) for the optical analysis and the IRTF library (Rayner et al., 2009) for the infrared wavelengths.

The index strengths are calculated from the flux distribution using specific index defini-

	Munari	BT-Settl
Model atmosphere code	Kurucz (1979)	Phoenix (Hauschildt et al., 1999)
Line lists	Kurucz (1992), Schwenke (1998)	Barber et al. (2006), Plez (1998)
Solar abundances	Grevesse & Sauval (1998)	Grevesse et al. (1993) / Caffau et al. (2011)

Table 2.2: Details of the model atmosphere codes used in the synthetic libraries.

tions (Tables 2.3 and 2.4). Each spectral feature is characterized by a central passband flanked by two pseudocontinuum sidebands to the red and blue neighbouring continua of the feature. To measure the strength of the index, the mean value of the flux at the two sidebands is calculated and a straight line that connects the midpoint of the two sidebands at their average flux level is drawn. This line defines the continuum flux level from which the index value is determined by calculating the difference in the spectrum level between the line and the flux level at the central passband. Equivalent widths of narrow atomic lines are measured in Å units using the equation from Worthey et al. (1994):

$$EW = \int_{\lambda_1}^{\lambda_2} \left( 1 - \frac{F_{I,\lambda}}{F_{C,\lambda}} \right) d\lambda \quad (2.1)$$

and broad molecular bands are calculated in magnitudes:

$$mag = -2.5 \log \left[ \frac{1}{\lambda_2 - \lambda_1} \int_{\lambda_1}^{\lambda_2} \left( \frac{F_{I,\lambda}}{F_{C,\lambda}} \right) d\lambda \right] \quad (2.2)$$

where  $\lambda_1$  and  $\lambda_2$  define the wavelength limits of the central passband.  $F_{I,\lambda}$  is the observed flux per unit wavelength in the index passband and  $F_{C,\lambda}$  is the flux level of the continuum defined by the straight line connecting the sidebands.

Theoretical libraries provide high-resolution spectra that were convolved to match the resolution of the empirical spectra. The spectra were convolved with a Gaussian function of a given full width at half maximum (FWHM) using the IDL code *gaussfold*. The gaussian FWHM is calculated based on:

$$FWHM_{gaussian} = \sqrt{(FWHM_{desired}^2 - FWHM_{actual}^2)}$$

where  $FWHM_{desired}$  is the desired resolution and  $FWHM_{actual}$  is the actual resolution of the theoretical spectra.

The following two subsections describe the comparisons in the optical and infrared. The last section of the chapter presents the new population synthesis models based on the previous results.

## 2.2.1 Comparison with observed stellar spectra in the optical

### The data

The empirical data used for this analysis were taken from Schiavon (2007) who used the original stellar spectra from the library of Jones (1999). The Jones empirical library has stellar spectra for 684 stars in the wavelength range 3820-5410Å (with a gap between 4500 and 4780 Å) and a resolution of 1.8 Å. Using the stellar parameters derived by Schiavon (effective temperature  $T_{eff}$ , surface gravity  $\log g$  and metallicity [Fe/H]), it was possible to assign theoretical spectra to represent the empirical sample selected for this study. For details on the methods used to derive these parameters please refer to Section 2.3 of Schiavon (2007).

For this test I selected a sample of stars around solar metallicity with [Fe/H]=0.0±0.1. The sample was then divided among dwarfs (stars with  $\log g > 3.5$ ) and giants ( $\log g \leq 3.5$ ). Figure 2.2 shows the parameter space covered by the selected sample of stars and the grid of synthetic spectra. The synthetic spectra are available at specific values of the temperature and surface gravity generating a grid with  $\Delta T_{eff} = 100\text{K}$  or  $250\text{K}$  depending on the theoretical library and  $\Delta \log g = 0.5$  between models. To represent each star from the sample the closest synthetic spectrum available was selected within 100K and 0.25 dex of the stellar  $T_{eff}$  and  $\log g$ , respectively.

### The indices

The optical comparison is based on the Lick/IDS indices, a total of 21 absorption-line features that have been identified in the spectra of Galactic stars throughout numerous observations devoted to understand the prominent absorption lines observed in the integrated light of galaxies. These observations were carried out at the Lick Observatory over three decades since 1972 using the Cassegrain spectrograph and Image Disc-

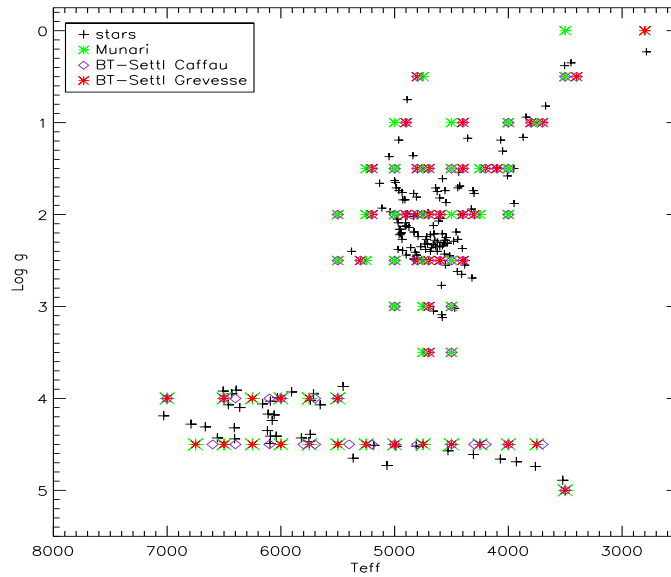


Figure 2.2: Coverage of the empirical data and theoretical spectra. The black crosses are the stellar parameters for the spectra used as calculated by Schiavon (2007), the colour symbols represent the synthetic spectra for the three libraries as indicated in the capture of the figure.

tor Scanner (IDS). The Lick indices have been presented in a number of papers and the definitions used in this work (Table 2.3) are those from Worthey et al. (1994) and Worthey & Ottaviani (1997). The iron and magnesium lines are typically used to study the chemical composition of stars. The Balmer lines ( $H\beta$ ,  $H\gamma$  and  $H\delta$ ) are mainly sensitive to the temperature of the turnoff stars and as such are good indicators of the age of a population.

In the original system the Lick/IDS indices are measured at resolutions between 8.4 and 10.9 Å in FWHM. All the theoretical spectra included in this analysis were convolved to match the corresponding resolution of the indices.

## Results

The indices listed in Table 2.3 were measured in all the theoretical spectra available and compared with the empirical equivalent widths from Schiavon (2007). The results are plotted in Figure 2.3 for the dwarf sample and in Figure 2.4 for the giant stars. The plots are colour coded as indicated in the first panel of each figure. The indices Fe5406 and Mg1 show only the trend observed in the theoretical libraries because there were no empirical data published for these indices. For the  $H\delta$  and  $H\gamma$  indices, only

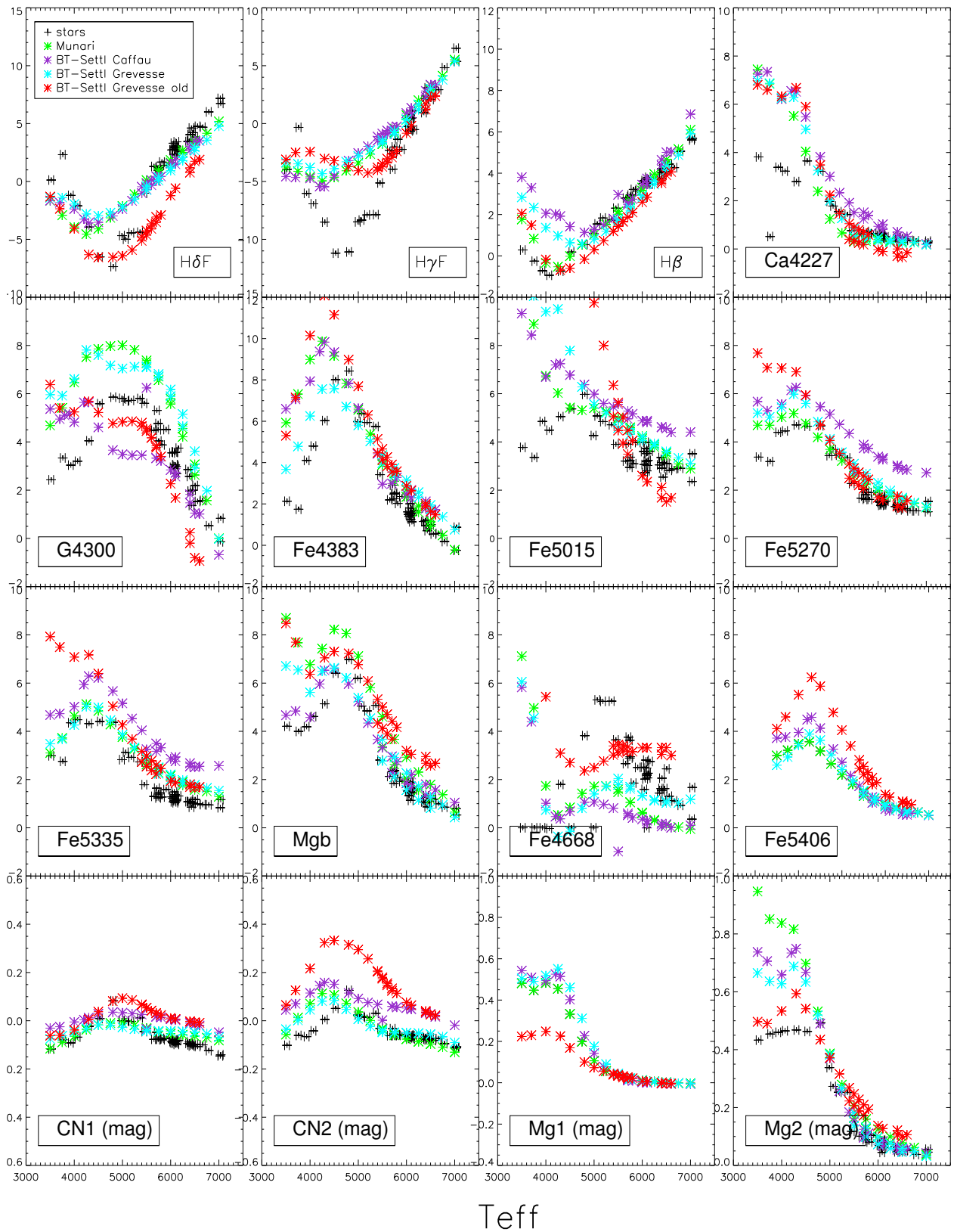


Figure 2.3: Optical comparison in dwarf stars with  $\log g > 3.5$ . Error bars indicate  $\pm 50\text{K}$  uncertainty in the effective temperature.

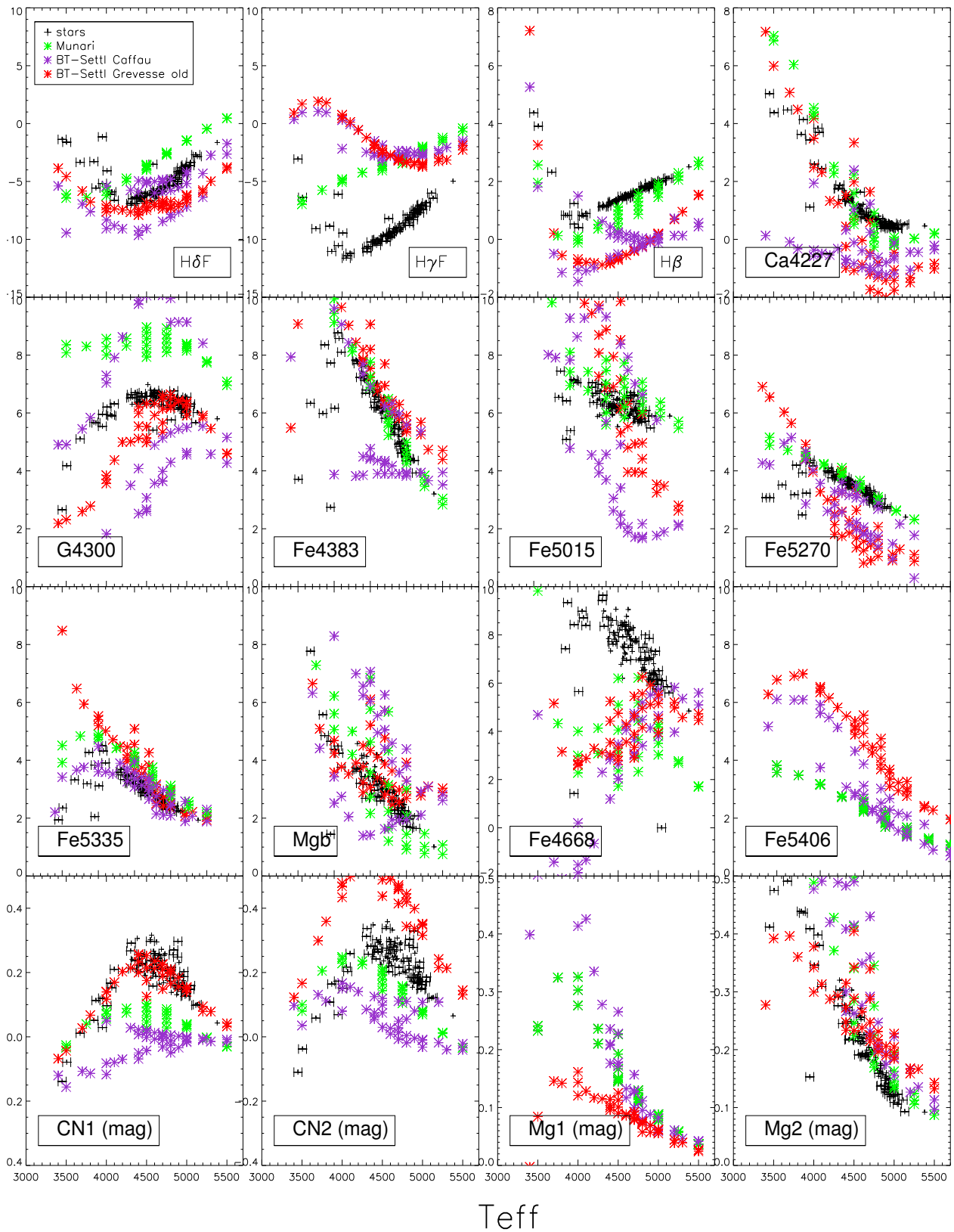


Figure 2.4: Optical comparison in giant stars with  $\log g \leq 3.5$ . Error bars indicate  $\pm 50\text{K}$  uncertainty in the effective temperature.

Index	Blue continuum	Central passband	Red continuum	Resolution <sup>a</sup>
H $\delta$ A	4041.600 4079.750	4083.500 4122.250	4128.500 4161.000	10.9
H $\gamma$ A	4283.500 4319.750	4319.750 4363.500	4367.250 4419.750	9.5
H $\delta$ F	4057.250 4088.500	4091.000 4112.250	4114.750 4137.250	10.9
H $\gamma$ F	4283.500 4319.750	4331.250 4352.250	4354.750 4384.750	9.5
Ca4227	4212.250 4221.000	4223.500 4236.000	4242.250 4252.250	10.3
G4300	4267.625 4283.875	4282.625 4317.625	4320.125 4336.375	9.7
Fe4383	4360.375 4371.625	4370.375 4421.625	4444.125 4456.625	9.3
H $\beta$	4827.875 4847.875	4847.875 4876.625	4876.625 4891.625	8.4
Fe5015	4946.500 4977.750	4977.750 5054.000	5054.000 5065.250	8.4
Mg1	4895.125 4957.625	5069.125 5134.125	5301.125 5366.125	8.4
Mg2	4895.125 4957.625	5154.125 5196.625	5301.125 5366.125	8.4
Mgb	5142.625 5161.375	5160.125 5192.625	5191.375 5206.375	8.4
Fe5270	5233.150 5248.150	5245.650 5285.650	5285.650 5318.150	8.4
Fe5335	5304.625 5315.875	5312.125 5352.125	5353.375 5363.375	8.4
Fe5406	5376.250 5387.500	5387.500 5415.000	5415.000 5425.000	8.4
Fe4668	4612.750 4631.500	4635.250 4721.500	4744.000 4757.750	8.7
CN1	4081.375 4178.375	4143.375 4178.375	4245.375 4285.375	10.3
CN2	4085.125 4097.625	4143.375 4178.375	4245.375 4285.375	10.3

Table 2.3: The Lick indices. Wavelength limits and resolution are in  $\text{\AA}$ . The indices H $\delta$  and H $\gamma$  have an F and A definitions which correspond to narrower and wider central passband limits, respectively. The index strengths are measured in EW in  $\text{\AA}$  apart from the molecular bands Mg and CN that are measured in magnitudes. <sup>a</sup> Resolution quoted in terms of FWHM.

the narrower central passband (definition F in Table 2.3) is included in the comparison. The F-definition is more effective to measure the absorption produced by F stars, whereas the A-definition is more sensitive to the absorption produced by the hotter A stars (Worthey & Ottaviani, 1997). The analysis of the results focuses on the four optical indices that are used later on in this work for the study of stellar populations: H $\beta$ , Fe5270, Fe5335 and Mgb.

In the dwarf regime overall, the libraries that present the best fits are the Munari and the new BT-Settl GVS. The new BT-Settl GVS clearly improves the fits to the data with respect to the older version of the library (predictions shift from red to cyan). All the theoretical libraries reproduce better the empirical data at temperatures above 5000K and the strengths of most indices are overpredicted at temperatures below 4500K. The cool dwarfs are also the fainter stars for which the spectra might have lower signal-to-noise ratio or more uncertainties in the flux calibration. The Balmer lines exhibit a steep behaviour as a function of temperature that is well represented by the theoretical libraries. The main contribution to the integrated value of H $\beta$  in an old population ( $\sim 10$  Gyr) is given by turn off main sequence stars at around 6000K and at this temper-

ature the fits from the theoretical libraries are very good. The Munari and new BT-Settl GVS produce the best fits to the *Mgb* band and the iron lines Fe5270 and Fe5335 that are used as metallicity indicators.

In the giant regime the Munari library presents the best fits to the data. It is the only library that can fit the empirical values of  $H\beta$  and makes very good predictions for all the iron lines, including the ones relevant to this work (Fe5270 and Fe5335). In the *Mgb* the Munari predictions present some scatter but still lie over the empirical values. Both BT-Settl libraries (CAF and old GVS) fail to represent the empirical data in most of the indices shown.

Based on the optical results the best spectral libraries to model the spectra of main sequence stars are the new version of the BT-Settl GVS and the Munari. The best choice to model the giant regime is clearly the Munari spectra.

## 2.2.2 Comparison with observed stellar spectra in the infrared

### The data

The stellar spectra used to study the infrared regime were taken from the IRTF empirical spectral library (Rayner et al., 2009). The library consists of 210 cool stellar spectra obtained with a medium-resolution spectrograph at the 3.0 m NASA InfraRed Telescope Facility (IRTF). The stars observed are from the solar neighbourhood and have metallicities around solar. The spectral range is from 8000 to 25000 Å and the spectra have a resolution  $R=2000$ . All the spectra are flux calibrated using the Two Micron All Sky Survey (2MASS) photometry. The library provides apparent  $VJK$  magnitudes and colour excess  $E(B - V)$  from which the interstellar extinction in  $VJK$  can be derived using the extinction laws from the literature.

For this work I selected a sample of cool stars with spectral classes: F, G, K, M, L and T that exclude all variable and peculiar stars. The distances for these stars were calculated using Hipparcos parallax measurements from the SIMBAD database (van Leeuwen, 2007). All the stars in this sample have parallax errors below 30%. A correc-

tion for the observation selection bias (the Lutz-Kelker bias) was applied according to Sandage & Saha (2002). Lutz-Kelker bias corrects for systematic errors in the parallax measurements which affect the absolute magnitudes. In this case the percentage error in the parallax measurements was so small that the correction bias was negligible.

From the stellar spectra different techniques were used to derive values for the effective temperature and bolometric luminosity of the stars. The methods are described below.

#### LOW MAIN SEQUENCE STARS: M, L AND T DWARFS

The temperature and bolometric luminosities of L and T dwarfs were obtained from Golimowski et al. (2004). The authors use  $JHK$  spectra of a sample of cool dwarfs, together with parallax measurements and estimates of the bolometric correction in the  $K$  band from photometry to calculate the absolute bolometric luminosity. They derive values for the effective temperature using the relationship between  $T_{eff}$  and luminosity from evolutionary models of dwarf stars from Burrows et al. (1997), Baraffe et al. (1998) and Chabrier et al. (2000). Their stars contained most of the L and T dwarfs from the IRTF library selected for this work except for five stars. These five missing stars were assigned values for the bolometric luminosity and effective temperature from stars of the same spectral type in the Golimowski sample.

The effective temperatures of the M dwarfs were calculated from observed colour- $T_{eff}$  calibrations in  $(V - K)$  by Casagrande et al. (2008) who derived an empirical temperature scale for late-type cool dwarfs. They studied a sample of 340 nearby M-type dwarf stars for which they obtained high quality optical and infrared photometry to derive stellar parameters using the Infra Red Flux Method (IRFM). The IRFM is a semi-empirical method to calculate the effective temperature of a star using the ratio  $R_{obs}$  of its total observed bolometric flux  $F_{Bol}$  and the monochromatic flux at a given wavelength  $F(\lambda_{IR})$ . The IRFM method is based on the relations (Alonso et al., 1996a):

$$R_{obs} = \frac{F_{Bol}}{F(\lambda_{IR})} = \frac{\sigma T_{eff}^4}{F_{mod}(\lambda_{IR}, T_{eff}, [Fe/H], g)} = R_{theo}(\lambda_{IR}, T_{eff}, [Fe/H], g)$$

To derive the effective temperature of the star, the empirical ratio  $R_{obs}$  is matched to

its theoretical counterpart  $R_{theo}$ . For a given chemical composition  $[Fe/H]$  and gravity  $g$  of the star, the theoretical ratio  $R_{theo}(\lambda_{IR}, T_{eff}, [Fe/H], g)$  is calculated to find the matching value of  $R_{obs}$ .

The luminosities of the M dwarfs were calculated from their bolometric magnitudes using the empirical relations from Casagrande et al. (2008) in the  $K$  band. The bolometric magnitude ( $M_{bol}$ ) was obtained from their linear fits:  $M_{bol} = 2.07 + 1.08 \times m_K$  and the luminosity was derived using its relationship to  $M_{bol}$ :

$$M_{bol} = -2.5 \log \frac{L}{L_{\odot}} + M_{bol,\odot} \quad (2.3)$$

assuming the bolometric magnitude of the Sun  $M_{bol,\odot}$  is equal to 4.72.

#### MAIN SEQUENCE AND GIANT STARS: F, G AND K

The main sequence stars were defined to be those with  $(J - K) < 0.5$  and  $M_K > 2.0$ . The effective temperatures of the main sequence stars were derived using the empirical calibrations of colour-effective temperature from Alonso et al. (1996b) in  $(V - K)$ . Their colour relations were derived using the IRFM described above. To use these calibrations in the TCS (Telescopio Carlos Sanchez) filter system the transformations from 2MASS system were done using the system transformations in Carpenter (2001). The luminosities were derived from the bolometric magnitudes in the  $V$ -band using Equation 2.3. The Bolometric Corrections ( $BC_V$ ) were obtained from Alonso et al. (1996b).

For the Red Giant Branch stars the effective temperature was derived from colour-temperature relations in  $(J - K)$  from Alonso et al. (1999). The colours had to be transformed from TCS filter system to the ESO (European Southern Observatory) system using the transformations from Carpenter (2001). The bolometric corrections in the  $V$  band were obtained from the same paper to derive the bolometric magnitudes and luminosities of the stars.

The final assigned values for the effective temperature and luminosities of the IRTF stars appear in Figure 2.5. In order to compare these spectra with their theoretical coun-

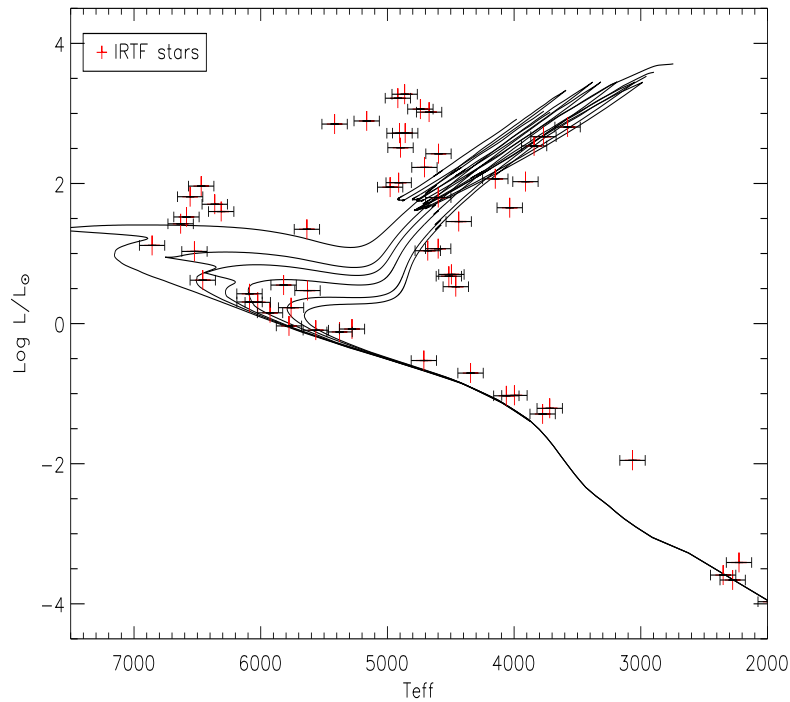


Figure 2.5: IRTF stars and solar metallicity isochrones for ages: 1, 2, 3, 5, 10 and 13.5 Gyr. The error bars indicate  $\pm 100\text{K}$  uncertainties in the effective temperature.

terparts it was necessary to derive an estimate of the surface gravity of the stars. This was done by approximating the IRTF derived temperatures to the stellar isochrones in the plot. The technique was to find the nearest isochrone point in the HRD with the same (or closest) effective temperature of the star and assign its value of the surface gravity to the star. This method is not intended to derive accurate stellar parameters but it was rather used as an approximation to derive estimates within a range. A table with the stellar parameters derived for the IRTF stars in this sample including the surface gravities assigned to each star appear in the appendix.

The theoretical spectra included in the comparison had values of  $T_{eff}$  within 100K of the empirical value and  $\log g$  within 0.25 dex from the derived IRTF values. All the theoretical spectra were convolved to match the resolution of the IRTF spectra where  $\sigma \sim 64 \text{ km/s}$ .

### The indices

The infrared (IR) absorption lines used for this part of the comparison are listed in

Index	Blue continuum	Central passband	Red continuum	Reference
NaI a	8150.00 8168.40	8168.50 8234.12	8235.00 8250.00	1
NaI b	8170.00 8177.00	8177.00 8205.00	8205.00 8215.00	2
NaI c	8164.00 8173.00	8180.00 8200.00	8233.00 8244.00	3
CaII0.86i	8474.00 8484.00	8484.00 8513.00	8563.00 8577.00	4
CaII0.86ii	8474.00 8484.00	8522.00 8562.00	8563.00 8577.00	4
CaII0.86iii	8619.00 8642.00	8642.00 8682.00	8700.00 8725.00	4
MgI0.88	8777.40 8789.40	8801.90 8816.90	8847.40 8857.40	5
FeH0.99	9855.00 9880.00	9905.00 9935.00	9940.00 9970.00	2
CaI (Smith12)	10300.00 10320.00	10337.00 10360.00	10365.00 10390.00	6
NaI1.14	11360.00 11370.00	11372.00 11415.00	11417.00 11427.00	2
KI1.17i	11667.00 11680.00	11680.00 11705.00	11710.00 11750.00	2
KI1.17ii	11710.00 11750.00	11765.00 11793.00	11793.00 11810.00	2
CaI1.98i	19740.00 19765.00	19770.00 19795.00	19800.00 19840.00	2
CaI1.98ii	19800.00 19840.00	19845.00 19880.00	19885.00 19895.00	2
NaI2.21	22035.00 22045.00	22047.00 22105.00	22107.00 22120.00	2
CO2.30i	22860.00 22910.00	22932.00 22982.00	23020.00 23070.00	2
CO2.30ii	23150.00 23200.00	23220.00 23270.00	23300.00 23350.00	2

Table 2.4: The IR indices. Wavelength limits and indices strengths are in Å. References for the index definitions: (1) Spiniello et al. (2012); (2) Conroy & van Dokkum (2012a); (3) Vazdekis et al. (2012); (4) Cenarro et al. (2001); (5) Diaz et al. (1989); (6) Smith et al. (2012).

Table 2.4. The list combines a number of features defined in several papers from the literature (references in the table) and were chosen because they have been used in previous studies of the IMF or in giant-to-dwarf ratio indicators.

The NaI doublet is a popular IMF indicator and this comparison includes three different definitions: a, b and c, that differ in the limits of the central passband and/or continuum sidebands. This is one of the main features discussed in this work. The other sodium indices in the list (NaI1.14 and NaI2.21) have been used in the literature as dwarf indicators and they are also sensitive to the Na/Fe content. The FeH0.99 feature is another of the indices initially used to study the IMF. This index is stronger in stars in the low main sequence but the strengths are relatively low in comparison with NaI and therefore harder to measure.

The indices CaII0.86 (also called CaT), KI1.17, CaI1.98 and CO2.30 have multiple features and the final equivalent width is calculated by adding the contribution of each absorption line. The CaT and CO2.30 lines are stronger in low gravity stars and can be used to study the giant contribution in an unresolved population. The indices KI1.17 and CaI1.98 have been found to be sensitive to the presence of cool dwarfs.

The MgI0.88 index on the other hand is sensitive to cool stars in general and does not distinguish among dwarfs and giants at solar metallicity (Diaz et al., 1989). The CaI feature has been recently defined by Smith et al. (2012) where they found a correlation between index strength and cool dwarfs.

## Results

The results for the dwarf stars appear in Figure 2.6 and for the giants in Figure 2.7. There are less empirical data points available for this comparison than there were for the optical test but general trends of index strength with temperature are still visible. The Munari library has a wavelength coverage only up to 10500 Å and is therefore not included in the redder indices presented here. The analysis is focused on the main IR indices that are used later on in this work: NaI, CaT and FeH0.99.

Among the dwarfs, the empirical trends are generally well reproduced by all theoretical libraries. The different NaI definitions yield a similar trend with temperature (despite the slight differences in strengths) and are well fitted by all the synthetic libraries. The CaT lines are best predicted by the BT-Settl GVS new library. The FeH0.99 is not well fitted by the Munari and BT-Settl new libraries. This index is stronger in cool dwarfs and this trend is well predicted by the other two BT-Settl libraries (CAF and old GVS). The FeH0.99 was used during the first IMF studies as a dwarf indicator, but FeH is a weak line that is generally hard to measure in low resolution spectra and for that reason is no longer the preferred index to study the IMF. Overall, the fits for the dwarfs in the infrared regime seem to be better for all the Phoenix-based libraries than in the optical. The new version of BT-Settl GVS (cyan) still exhibits better fits to the data than the older version (red) and than the BT-Settl CAF (purple).

The giants on the other hand are less well represented by the Phoenix-based libraries, especially at lower temperatures. In general, the Munari predictions produce by far the best fits to the data. The NaI and FeH0.99 lines are mainly sensitive to the presence of dwarfs and so the observed giants yield values very close to zero. An exception is seen in FeH0.99 where the line is sensitive to the coolest giants ( $T_{eff} < 4000$ ), however the strengths are even weaker than in the dwarfs at the same temperature. The CaT

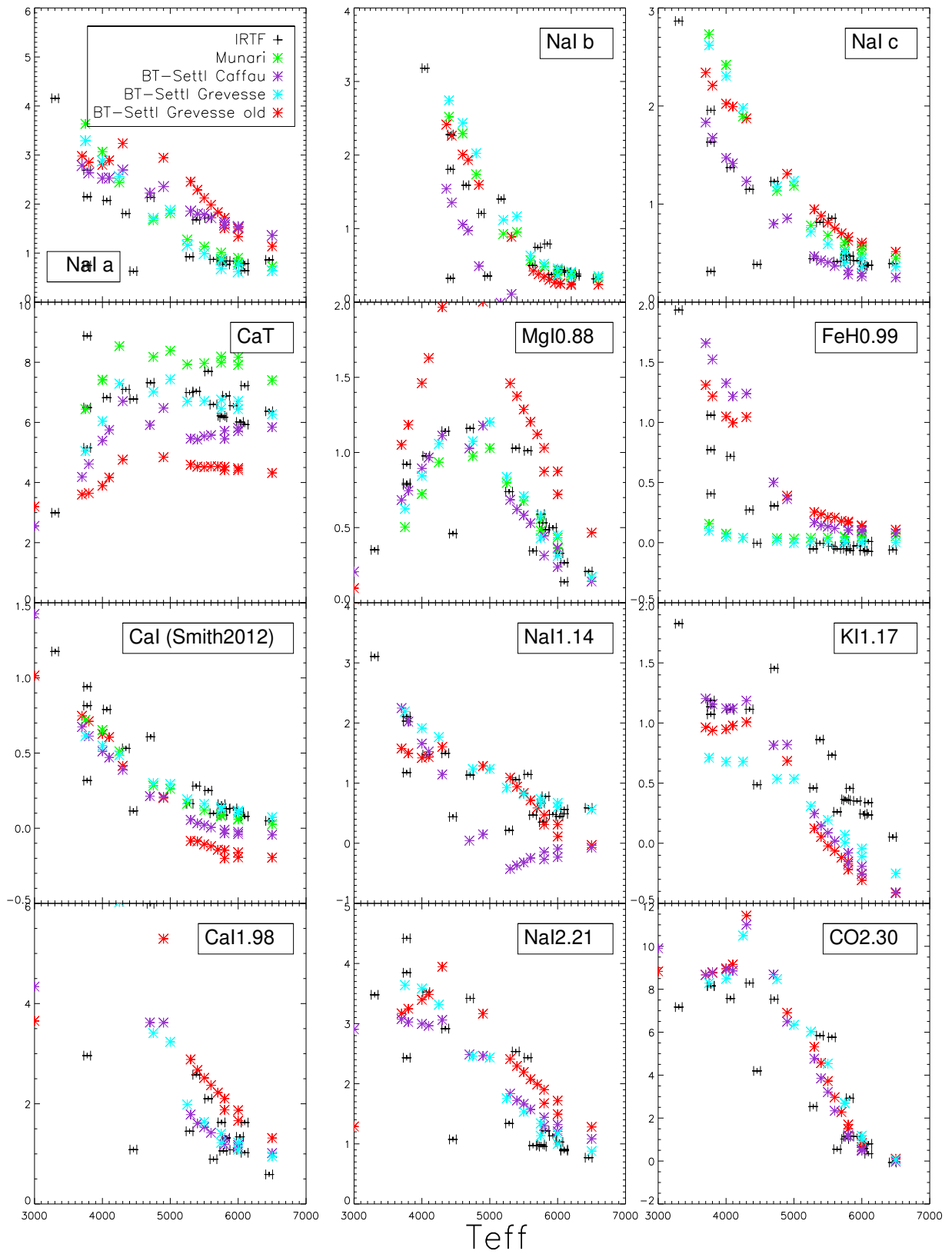


Figure 2.6: Infrared comparison in dwarf stars with  $\log L/L_{\odot} < 0.67$ . Error bars indicate  $\pm 50\text{K}$  uncertainty in the effective temperature.

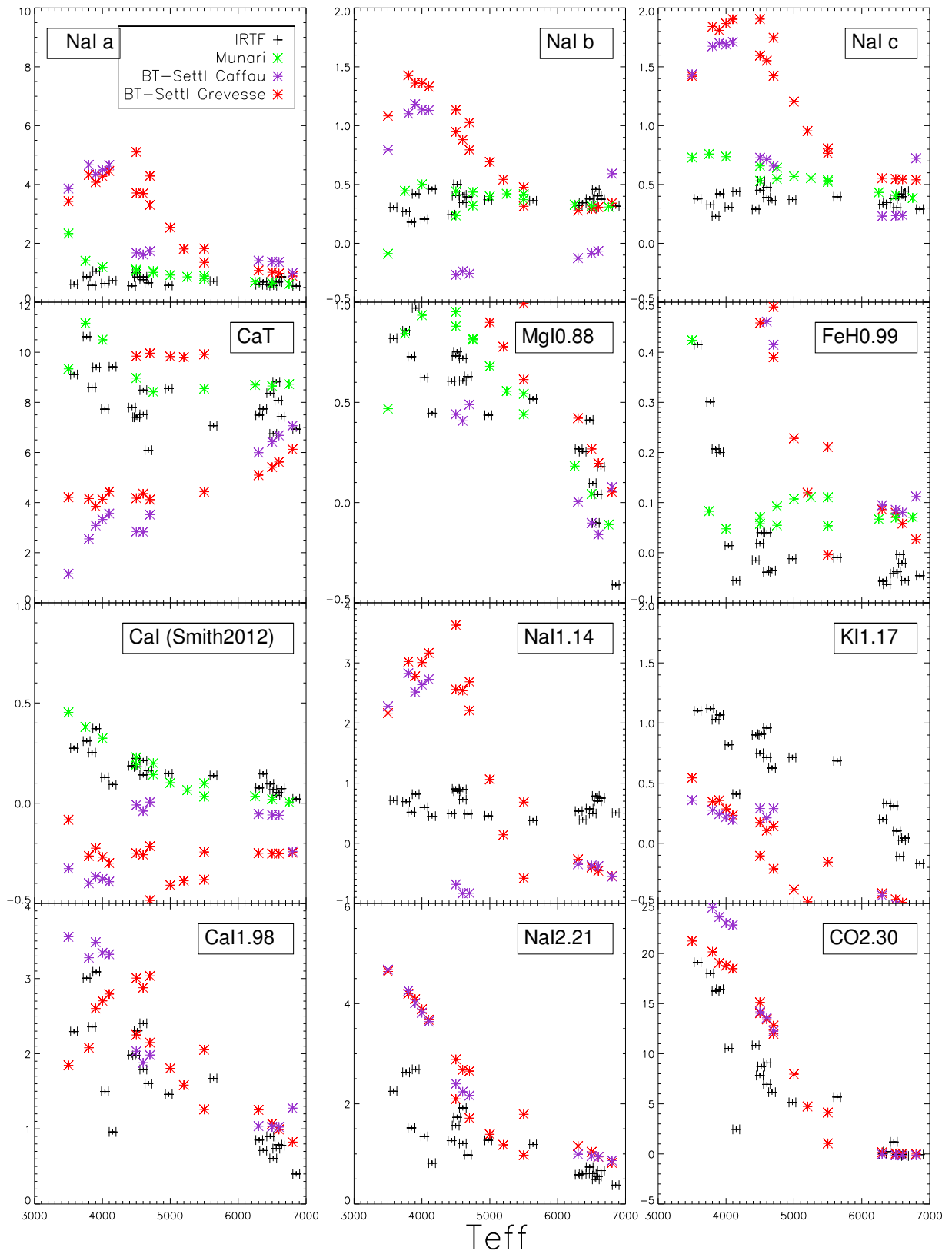


Figure 2.7: Infrared comparison in giant stars with  $\log L/L_{\odot} \geq 0.67$ . Error bars indicate  $\pm 50\text{K}$  uncertainty in the effective temperature.

is a giant indicator and the stronger lines are well fitted by Munari. All the BT-Settl libraries fail to predict the trends observed in the three indices of interest.

The infrared results show that the new BT-Settl GVS is the best library to sample cool dwarfs and the Munari for the giants, in agreement to what was observed in the optical analysis. The Phoenix-based libraries have shown a poor performance to represent the spectra of giant stars in the optical and IR regimes.

## 2.3 Final choices and the PSMs ingredients

All the discussions presented in this chapter show clearly that the new version of BT-Settl GVS is the best choice to assign spectra to the dwarf stars ( $\log g \geq 5.0$ ). The BT-Settl spectra have a better coverage of the parameter space for the dwarfs in comparison to Munari (they reach cooler temperatures and higher surface gravities) and the measured indices represent well the observed values in the optical and infrared. On the other hand, Munari is the best library to sample the rest of the main sequence stars and giants because of all the libraries it is the one that most successfully matches the observed indices. The fluxes from both spectral libraries are provided in the same units ( $\text{ergs/sec/cm}^2/\text{\AA}$ ) and in order to combine them the BT-Settl spectra have to be scaled by  $1/\pi$  to transform from physical into astrophysical flux. These libraries together with the BaSTI+ isochrones, are the main ingredients of the new population synthesis models presented in this thesis.

To illustrate further the suitability of the theoretical libraries, Figures 2.8 and 2.9 show comparisons between observed and theoretical spectra for a K dwarf (effective temperature  $\sim 4750$  and  $\log g \sim 4.5$ ) and a K giant (effective temperature  $\sim 4500$  and  $\log g \sim 2.5$ ). The empirical spectra was obtained from the Miles library (Sánchez-Blázquez et al., 2006). The resolution of all spectra has been lowered to  $10\text{\AA}$  FWHM to facilitate the comparison. Details of the stellar parameters of the synthetic and empirical spectra appear in the figures.

The coverage of the parameter space of the isochrones and the combination of both

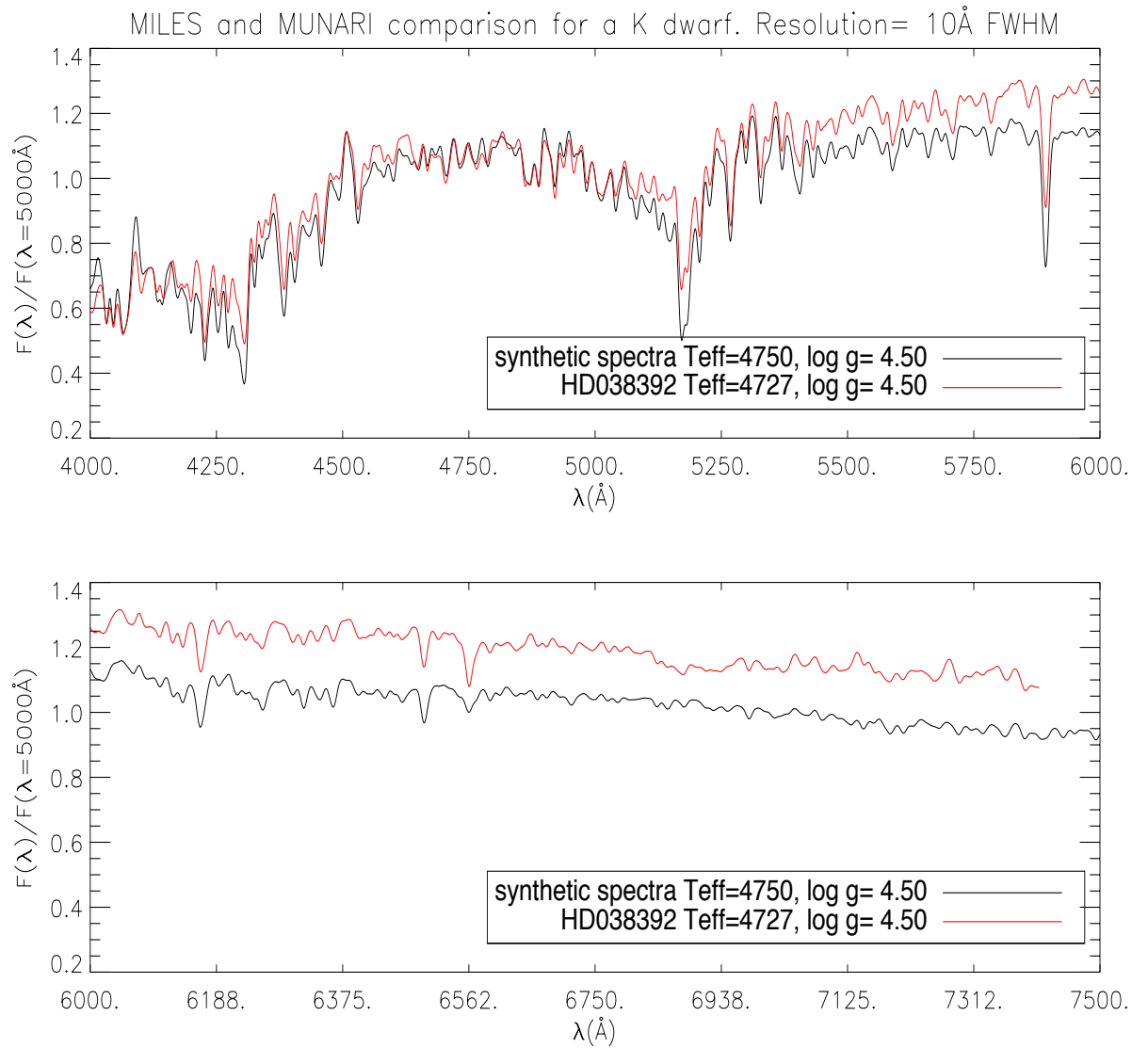


Figure 2.8: Comparison between a theoretical spectrum from the Munari library and an observed stellar spectrum from the MILES library for a K dwarf. The fluxes were normalized at 5000 Å. The stellar parameters are detailed in the figure.

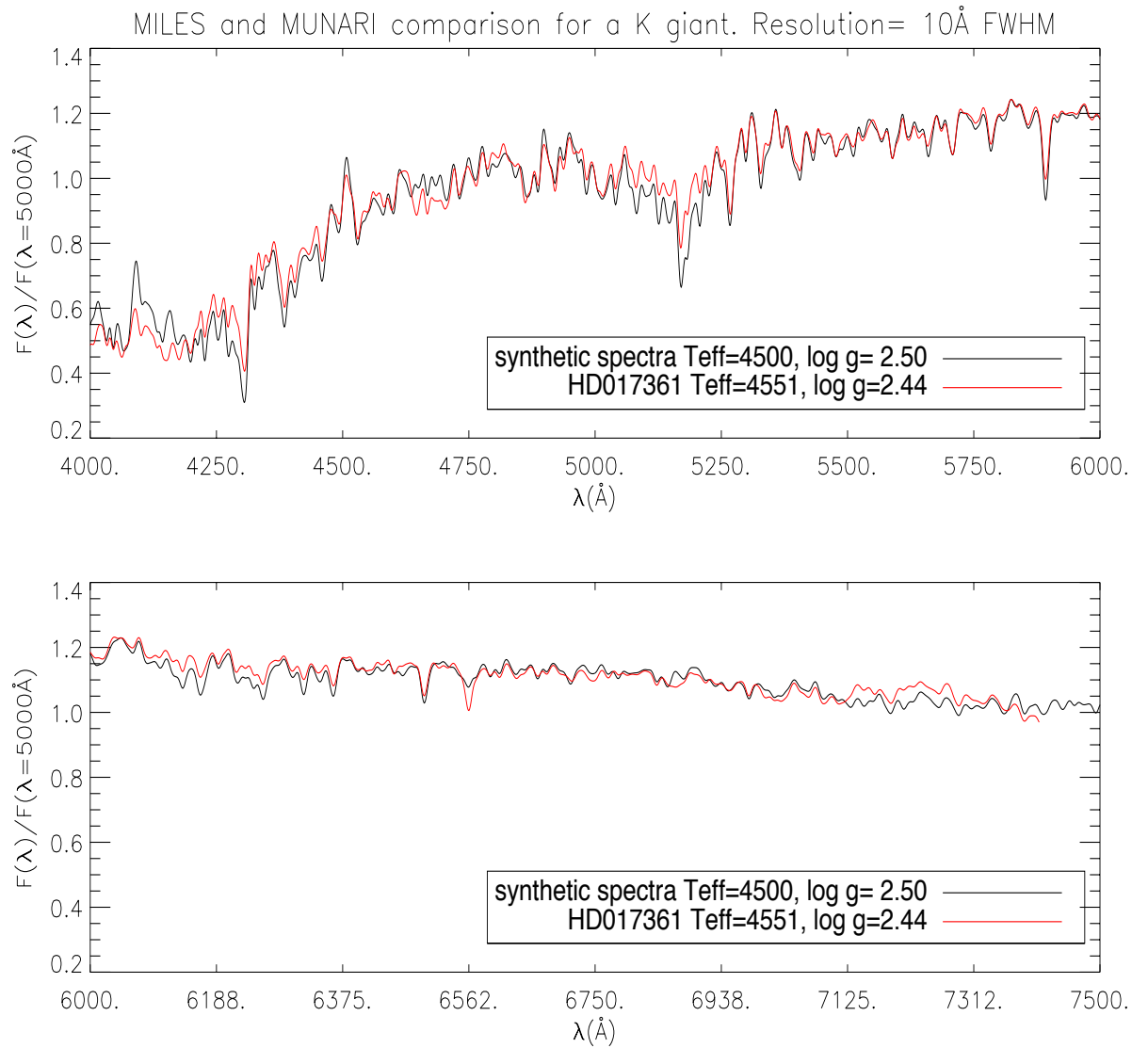


Figure 2.9: Comparison between a theoretical spectrum from the Munari library and observed stellar spectrum from the MILES library for K giant. The star HD017361 has  $[\text{Mg}/\text{Fe}] = -0.09$ . The fluxes were normalized at 5000 Å.

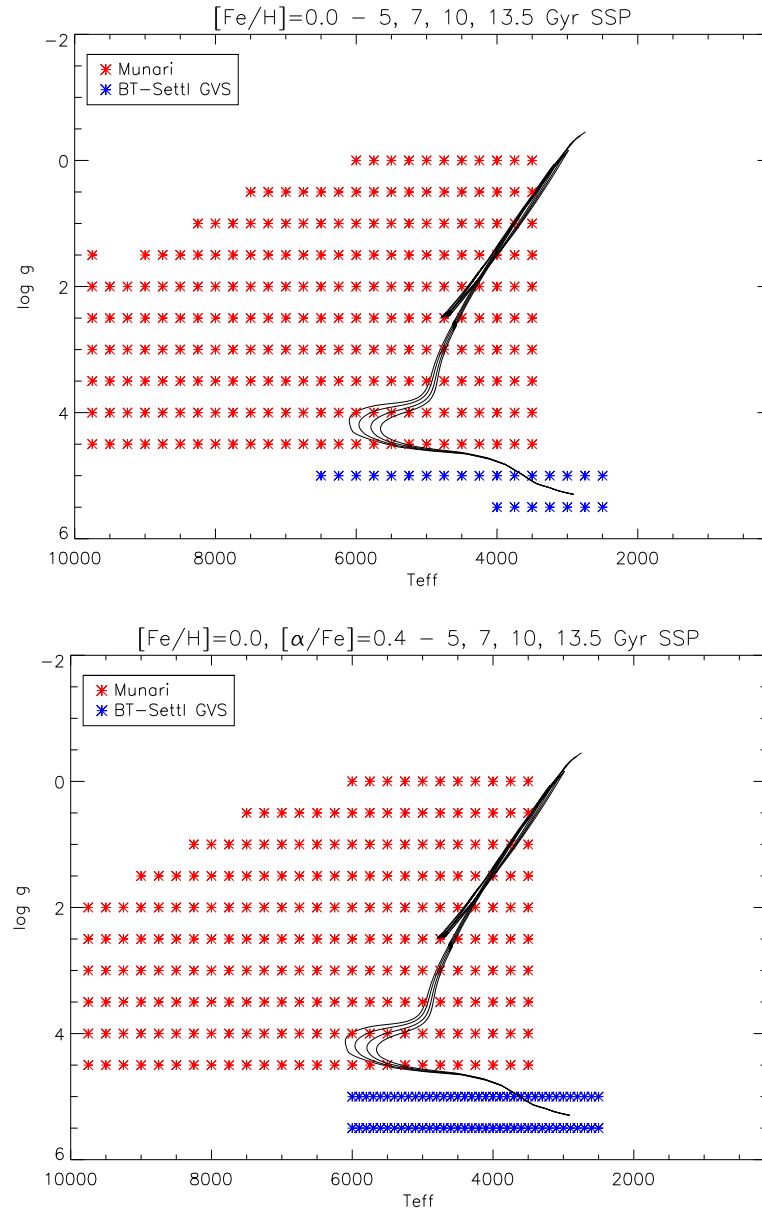


Figure 2.10: Grid of synthetic spectra and isochrones for  $[\text{Fe}/\text{H}] = 0$  with scaled-solar metal mixture (top panel) and  $\alpha$ -enhanced abundances (bottom panel). The two spectral libraries are colour coded as indicated in the plots. The four isochrone ages correspond to 5, 7, 10 and 13.5 Gyr (hottest to coolest TO temperature).

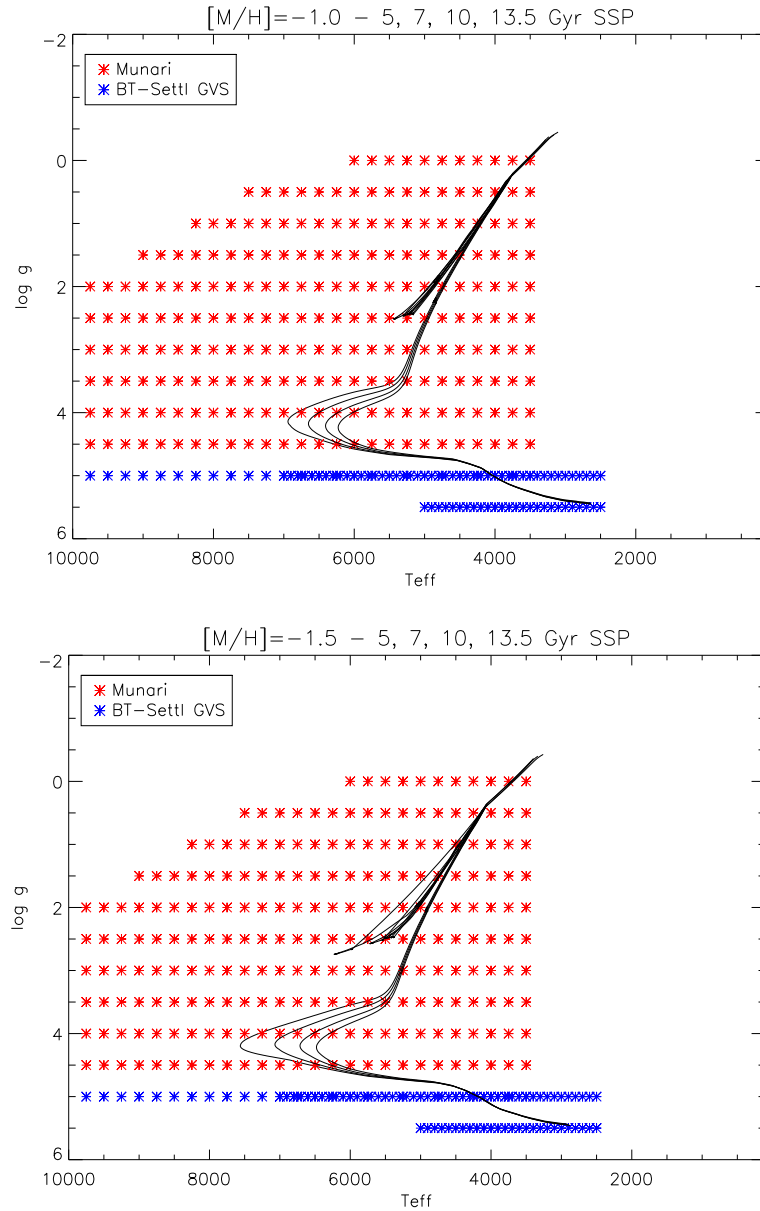


Figure 2.11: Grid of synthetic spectra and isochrones for  $[\text{Fe}/\text{H}] = -1.31$  (top) and  $-1.81$  (bottom), both with  $[\alpha/\text{Fe}] = +0.4$ . The total metal abundance  $[M/H]$  is indicated at the top of each panel. The two spectral libraries are colour coded as indicated in the plots. The four isochrone ages correspond to 5, 7, 10 and 13.5 Gyr (hottest to coolest TO temperature).

spectral libraries is illustrated in Figures 2.10 and 2.11. The panels show the grid of synthetic spectra for the metallicities and isochrone ages that are used in the next chapters. The PSMs are available at  $[\text{Fe}/\text{H}] = 0$  with scaled-solar abundances and an  $\alpha$ -enhanced metal mixture. The models with  $[\text{Fe}/\text{H}] = 0$  at scaled-solar and  $\alpha$ -enhanced metal mixtures are constructed with scaled-solar isochrones. The change in metallicity will affect the temperature predictions of the isochrone points. However, Conroy & van Dokkum (2012a) found that these differences are much smaller than the differences produced when changing the spectra assigned to each point along the isochrone at different metallicity and fixed temperature. The sub-solar metallicities  $[\text{M}/\text{H}] = -1.0$  and  $-1.5$  are all  $\alpha$ -enhanced and are quoted in terms of the total metal content  $[\text{M}/\text{H}]$  which corresponds to  $[\text{Fe}/\text{H}] = -1.31$  and  $-1.81$ , respectively. The  $\alpha$ -enhancement is  $+0.4$  for all models in this thesis. The PSMs are for old stellar populations with ages 5, 7, 10 and 13.5 Gyr.

From Figure 2.10 it is visible that the bright and cool giants are not sampled by either of the theoretical libraries. When the PSMs were initially constructed, neither of the two libraries had available spectra to cover this area of the parameter space. The original PSMs in this thesis do NOT include giant stars cooler than 3500K and surface gravities with  $\log g \leq 1.0$  when computing the integrated spectra of the populations.

At the final stages of the write-up of this thesis, the authors of the BT-Settl library were able to produce new low-gravity model atmospheres at solar metallicity making it possible to complete the grid in Figure 2.10. New model atmospheres were specially calculated for this work and new synthetic spectra for these cool and bright giants was obtained from the BT-Settl (Phoenix) library. The completed coverage of the parameter space is illustrated in Figure 2.12.

A comparison between the Munari and BT-Settl libraries for a common spectrum with effective temperature = 3500K and  $\log g = 1.0$  is shown in Figure 2.13. It is visible from this comparison that the two libraries produce very different spectra for the same parameters (effective temperature and surface gravity). The reasons for these observed differences are manifold and the study of them is beyond the scope of this work. The impact of the library extension on line indices predictions will be assessed in Section

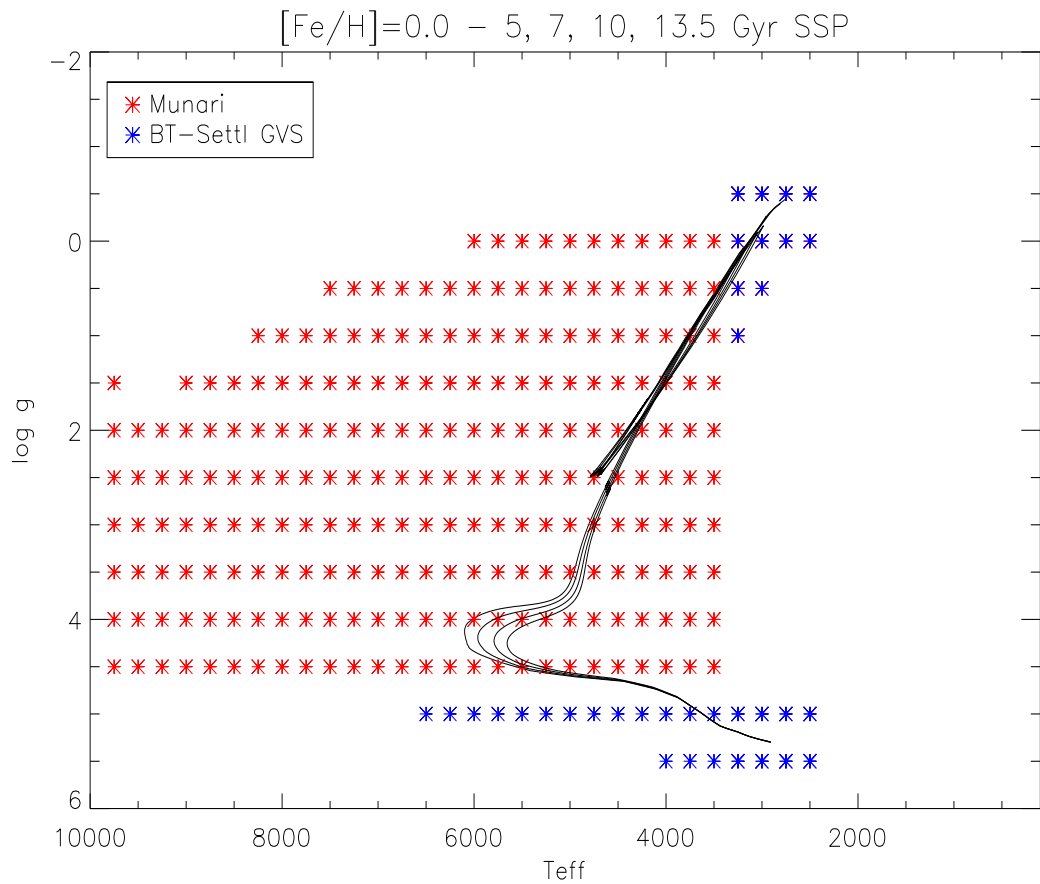


Figure 2.12: A completed version of the grid of synthetic spectra and isochrones shown in Figure 2.10 for  $[\text{Fe}/\text{H}] = 0$  and scaled-solar metal mixture. The additional spectra included in this version of the PSMs are represented by the blue stars at low surface gravity values. The model grid is composed of two libraries colour coded as indicated in the diagram.

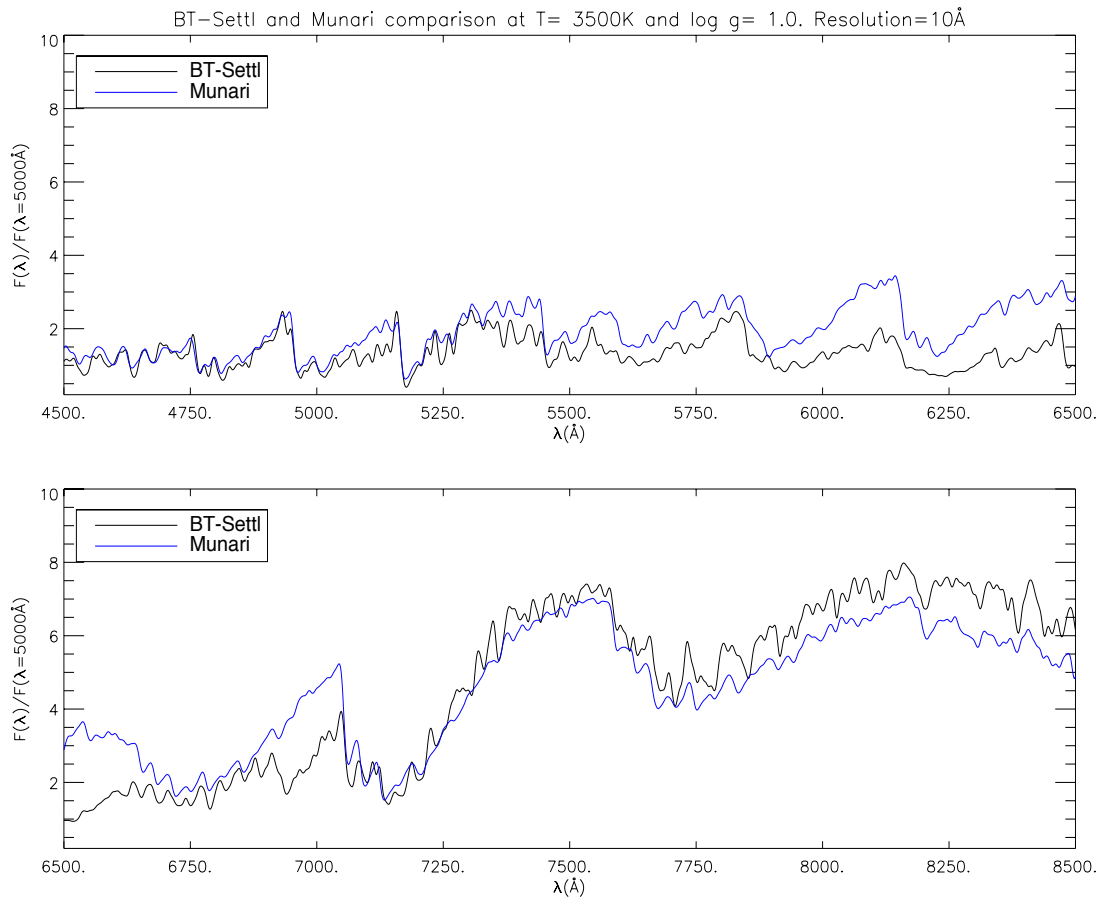


Figure 2.13: Comparison between BT-Settl and Munari synthetic spectra at 3500 K and  $\log g = 1.0$  at solar metallicity. Both spectra were normalized at  $\lambda = 5000\text{\AA}$ .

3.2.

### 2.3.1 Final remarks

The BT-Settl library was constructed especially to study cool, dwarf stars. The results presented in Sections 2.2.1 and 2.2.2 were discussed in private communication with the Lyon group who developed the BT-Settl model atmospheres. They suggested that a possible explanation for the poor performance of the BT-Settl libraries in the giant regime is the calibration of the mixing length parameter  $\alpha_{ML}$ . Convection becomes increasingly important in the atmospheres of giant stars due to their cool temperatures and its modelling can affect the line broadening parameters. The group is currently using 3D hydrodynamical models to recalibrate  $\alpha_{ML}$  in their 1D models for giant stars. This recalibration could improve the fits to the data but the results are not available yet. The new model atmospheres included in the completed version of the PSMs were produced using the latest version of their code but still present the same uncertainty. The modelling of atmospheres of low gravity stars is complex due to their extended envelopes, ongoing mass loss and dust formation. This is also true for the Munari library which has shown more scattered predictions around the observed values in the giants than in the dwarfs (Figures 2.4 and 2.7). The inclusion of the brightest giant stars do not have a great effect on the spectral lines in general, this will be discussed in Section 3.2. For these reasons, ALL of the work in this thesis was performed using the original PSMs with no bright giants (Figure 2.10).

## Chapter 3

# Behaviour of IMF-sensitive indices in synthetic SSP models

The main purpose of the new PSM is to study the IMF using absorption line indices with the approach introduced in Section 1.3.2. Several studies have now revived this technique to study the IMF of extragalactic systems. In this chapter I use the new PSM to construct integrated spectra of SSPs to explore the behaviour of absorption features recently defined and used in the literature as IMF indicators.

In order to use gravity-sensitive indices as IMF indicators it is important to understand how these spectral features respond to changes in other properties of the population and explore possible degeneracies with age and metallicity. To further understand the behaviour of the indices I look at the contribution from the different evolutionary phases to the final integrated values.

Another important aspect is to understand how uncertainties in the PSM can affect the predictions of these indices. In this chapter I explore the overall impact of uncertainties in the stellar isochrones.

### 3.1 PSM to generate integrated spectra of SSPs

The integrated spectrum for an SSP is calculated by adding the contribution of each point along the isochrone according to Equation 1.1. In order to assign a spectrum to each isochrone point it is necessary to interpolate linearly from the individual synthetic spectra that have a specific value of the effective temperature and the surface gravity (see Figures 2.10 and 2.11). For each point along the isochrone the code finds the nearest four-point grid of synthetic spectra in the parameter space (effective temperature and surface gravity). The code first interpolates among the high-gravity models and the low-gravity ones to produce two spectra for the given effective temperature of the isochrone point. Then it interpolates among these two spectra to produce a final spectrum for the  $\log g$  defined by the isochrone point.

The luminosity of an SSP is calculated from the total sum of the individual spectra in this way:

$$L_{SSP} = \sum_{i=1}^n f_{\lambda,i} \times \Phi_i \times S_i \quad (3.1)$$

where  $f_{\lambda,i}$  is the flux distribution of each isochrone point (the spectrum interpolated from the spectral libraries as described in the paragraph above) measured at the surface of the star in units of  $\text{ergs/s/cm}^2/\text{\AA}$ ;  $\Phi$  represents the IMF (defined in Equation 1.4) which determines the number of stars ( $dN$ ) for a given mass according to the chosen exponent  $x$  (for a Salpeter IMF  $x= 2.35$ ) and  $S_i$  is the surface area of the isochrone point which is calculated from its radius that is derived using the relationship between radius, luminosity and temperature:

$$L_i = S_i \times \sigma T_{\text{eff},i}^4 \quad (3.2)$$

where  $L_i$  and  $T_{\text{eff},i}^4$  are the luminosity and effective temperature of the isochrone point. Scaling the spectra by the surface area of the isochrone point ( $S_i$ ) accounts for the different dimensions of the stars in the population and therefore, their different luminosities at a given effective temperature. The IMF ( $\Phi_i$ ) weights the spectrum of an isochrone point because it determines the number of stars evolving at a given initial

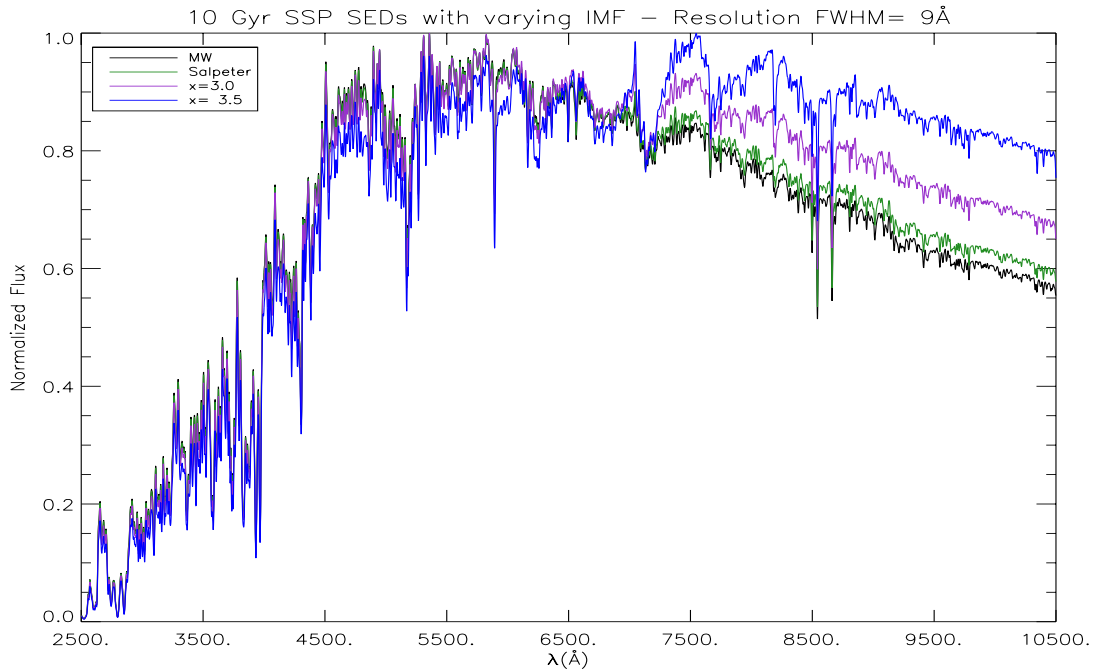


Figure 3.1: Examples of SEDs for the whole available spectral range for a 10 Gyr population with  $[\text{Fe}/\text{H}] = 0$ , scaled-solar abundances and different IMF exponents denoted by the colours as indicated in the caption. The original resolution was lowered to the approximate resolution of the Lick indices and the flux was normalized to a maximum value of 1.

stellar mass. The individual fluxes are also scaled by the inverse of the square of the distances to place them at a 10 pc distance to calculate absolute magnitudes from the spectra. The individual spectra for each isochrone point are then added together to generate the integrated spectrum of the population. The final integrated spectrum is normalized to  $1M_{\odot}$  for an SSP at 10 pc.

The PSM produces high-resolution spectral energy distributions (SEDs) that cover a spectral range from 2500 to 10500 Å. In Figure 3.1 there are some examples of solar metallicity SEDs for a 10 Gyr population with various IMF exponents. In this case the resolution of the spectra was convolved with a Gaussian of  $\text{FWHM} = 9\text{Å}$  which is the approximate resolution of the Lick/IDS system. This is the resolution that will be used for the analysis in the next section.

## **3.2 Impact of the coverage of the parameter space on the integrated spectra of SSPs**

The PSMs ingredients were presented in Section 2.3 where it was also discussed the coverage of the parameter space of the original PSMs. The original PSMs do not cover the parameter space occupied by the brightest and coolest giant stars of the population. This issue affects mainly populations at metallicities around solar because at lower metallicities the stars on the tip of the RGB and later evolutionary stages are hotter than at higher metallicities.

In order to understand the overall implication of the original restriction in the models, I generated integrated spectra for three SSPs, each with a different coverage of the parameter space. I selected a list of spectral features which are used throughout this thesis (see Tables 2.3, 2.4 and 3.5) to measure the equivalent widths in 1. the original version of the PSMs without bright giants (Figure 2.10); and 2. the completed version including cool and bright giants (Figure 2.12). As a control test, I also constructed a PSM replacing two additional low-gravity models from the original Munari library with new BT-Settl spectra. The spectra replaced have effective temperature= 3500K and  $\log g = 0.5$  and  $1.0$ . The idea of this additional SSP model is to test for possible systematics effects introduced by using a different spectral library in this parameter space.

Table 3.1 shows the absolute values of the individual indices measured in the integrated spectra of a 13.5 Gyr SSP at solar metallicity and Salpeter IMF produced by different versions of the PSMs. Column 2 shows the values produced by the original PSMs with no bright giants. Column 3 shows the values produced by the PSMs which include bright giants from the BT-Settl library. Column 4 shows the values produced by the PSMs with bright giants from BT-Settl and the additional replacement of two low gravity models from the Munari library with the BT-Settl. All indices were measured in the high-resolution spectra produced in the population synthesis.

The main differences are observed in the red part of the spectrum as expected since cool

### 3.2. Impact of the coverage of the parameter space on the integrated spectra of SSP54

Index	Original model (without bright giants)	Model with bright giants	BT-Settl	Model with BT-Settl bright giants + 2 Munari spectra replaced
H $\beta$	1.109	1.133		1.115
Mgb	4.595	4.675		4.677
Fe5270	3.933	3.953		3.927
Fe5335	4.350	4.351		4.335
Fe5406	2.563	2.588		2.626
NaD	3.902	3.939		3.861
NaIb	1.766	1.821		1.927
CaT	8.575	8.527		8.054
FeH0.99	0.090	0.456		0.526
bTiO	0.022	0.026		0.023
aTiO	0.017	0.018		0.017
TiO1	0.024	0.031		0.027
TiO2	0.073	0.084		0.075
CaH1	-0.0002	0.0001		0.0011
CaH2	0.041	0.054		0.041

Table 3.1: The effect produced on individual indices when adding cool giants to a 13.5 Gyr old population with solar metallicity and Salpeter IMF. The indices were measured in high resolution spectra. The values are in Å except for the the TiO and CaH bands that are in magnitudes.

giant stars mainly contribute to the integrated light in this spectral range. The strong increase in the FeH0.99 line is in agreement with previous studies which showed that this line is highly sensitive to the temperature of the tip of the RGB (Schiavon et al., 1998). All the TiO lines are sensitive to the presence of the cool giant stars and the indices become stronger as these are included in the population. The same is true for the CaH lines. The change observed in CaH2 when the giants are included is in disagreement with what Spiniello et al. (2014) had found (they observed that this line was only strong in cool dwarfs).

The effect observed when the Munari spectra are replaced by the BT-Settl indicates that there is some kind of compensation in some spectral regions by the inclusion of these spectra. All the TiO bands and CaH2 for instance produce integrated values that are closer to the original model with no bright giants when more BT-Settl spectra is used in the PSMs. Bluer indices on the other hand, deviate more from the original value when the original Munari spectra are replaced by BT-Settl.

Another crucial test for the PSMs is to calculate the fractional contribution of stars at each evolutionary stage to the final integrated light of the population at different

### 3.2. Impact of the coverage of the parameter space on the integrated spectra of SSP55

wavelengths. Tables 3.2 and 3.2 show the percentage contribution for a 13.5 and 5 Gyr population with Salpeter IMF at solar metallicity. Table 3.4 shows the percentage contribution for a 13.5 Gyr metal-poor SSP with  $[\text{Fe}/\text{H}] = -1.81$  and Salpeter IMF.

For the solar calculation at 13.5 Gyr the limits for each evolutionary phase are defined as follows:

- Low Main Sequence: all stars with surface gravity  $\log g \geq 4.5$ .
- Turn Off: all stars with surface gravity  $4.0 \leq \log g < 4.5$
- Sub Giant Branch: all stars with surface gravity  $3.5 \leq \log g < 4.0$
- Red Giant Branch: isochrone sequence that starts at  $\log L/L_{\odot} = 0.62$ ,  $T_{\text{eff}} = 4849$  and  $\log g = 3.49$  and reaches  $\log L/L_{\odot} = 3.45$ ,  $T_{\text{eff}} = 2984$  and  $\log g = -0.16$
- He-burning phase: isochrone sequence that starts at  $\log L/L_{\odot} = 3.26$ ,  $T_{\text{eff}} = 3123$  and  $\log g = 0.09$  and reaches  $\log L/L_{\odot} = 1.66$ ,  $T_{\text{eff}} = 4724$  and  $\log g = 2.41$
- Asymptotic Giant Branch: isochrone sequence that starts at  $\log L/L_{\odot} = 1.67$ ,  $T_{\text{eff}} = 4723$  and  $\log g = 2.4$  and reaches  $\log L/L_{\odot} = 3.53$ ,  $T_{\text{eff}} = 2957$  and  $\log g = -0.27$

For the metal-poor population at the same age, the definitions of the later evolutionary phases (after the Sub Giant Branch) differ as follows:

- Red Giant Branch: isochrone sequence that starts at  $\log L/L_{\odot} = 0.74$ ,  $T_{\text{eff}} = 5455$  and  $\log g = 3.49$  and reaches  $\log L/L_{\odot} = 3.36$ ,  $T_{\text{eff}} = 4055$  and  $\log g = 0.04$
- He-burning phase: isochrone sequence that starts at  $\log L/L_{\odot} = 3.19$ ,  $T_{\text{eff}} = 4216$  and  $\log g = 0.59$  and reaches  $\log L/L_{\odot} = 1.77$ ,  $T_{\text{eff}} = 5808$  and  $\log g = 2.57$
- Asymptotic Giant Branch: isochrone sequence that starts at  $\log L/L_{\odot} = 1.78$ ,  $T_{\text{eff}} = 5805$  and  $\log g = 2.57$  and reaches  $\log L/L_{\odot} = 3.56$ ,  $T_{\text{eff}} = 3694$  and  $\log g = 0.0$

$\lambda$ (Å)	Low Main Se- quence	TO stars	SGB	RGB	He- burning phase	AGB
5000.50	18.25	32.03	4.92	26.54	12.33	5.93
6000.50	20.99	25.52	4.40	30.17	11.81	7.11
7000.50	23.69	21.90	3.91	32.30	10.53	7.68
8000.50	25.27	18.33	3.44	34.75	9.71	8.50
8500.50	23.90	18.04	3.51	35.88	9.91	8.76
9000.50	25.72	15.75	3.10	36.91	9.18	9.34
9500.50	25.58	14.71	2.91	38.40	8.55	9.85

Table 3.2: The percentage contribution at different wavelengths from each evolutionary phase to the total integrated flux of a 13.5 Gyr population with Salpeter IMF and solar metallicity.

For the 5 Gyr population at solar metallicity and Salpeter IMF the limits for each evolutionary phase are defined as follows:

- Low Main Sequence: all stars with surface gravity  $\log g \geq 4.3$ .
- Turn Off: all stars with surface gravity  $3.88 \leq \log g < 4.3$
- Sub Giant Branch: all stars with surface gravity  $3.75 \leq \log g < 3.88$
- Red Giant Branch: isochrone sequence that starts at  $\log L/L_{\odot} = 0.56$ ,  $T_{\text{eff}} = 5100$  and  $\log g = 3.74$  and reaches  $\log L/L_{\odot} = 2.92$ ,  $T_{\text{eff}} = 3576$  and  $\log g = 0.78$
- He-burning phase: isochrone sequence that starts at  $\log L/L_{\odot} = 2.75$ ,  $T_{\text{eff}} = 3715$  and  $\log g = 1.02$  and reaches  $\log L/L_{\odot} = 1.70$ ,  $T_{\text{eff}} = 4717$  and  $\log g = 2.48$
- Asymptotic Giant Branch: isochrone sequence that starts at  $\log L/L_{\odot} = 1.70$ ,  $T_{\text{eff}} = 4717$  and  $\log g = 2.49$  and reaches  $\log L/L_{\odot} = 3.71$ ,  $T_{\text{eff}} = 2743$  and  $\log g = -0.45$

### 3.3 Definition of IMF-sensitive indices

Stellar spectral features that are strong in cool dwarfs or giants are known as IMF-sensitive indices because they can be used to quantify giant-to-dwarf ratios from the

$\lambda$ ( $\text{\AA}$ )	Low Main Se- quence	TO stars	SGB	RGB	He- burning phase	AGB
5000.50	27.80	25.53	2.28	26.98	7.73	9.68
6000.50	26.35	20.02	2.01	32.18	8.03	11.40
7000.50	26.22	17.37	1.81	35.16	7.47	11.97
8000.50	25.34	14.54	1.60	38.36	7.16	13.01
8500.50	24.20	14.05	1.58	39.42	7.35	13.41
9000.50	24.40	12.49	1.43	40.52	6.93	14.23
9500.50	23.90	11.71	1.35	41.65	6.51	14.87

Table 3.3: The percentage contribution at different wavelengths from each evolutionary phase to the total integrated flux of a 5 Gyr population with Salpeter IMF and solar metallicity.

$\lambda$ ( $\text{\AA}$ )	Low Main Se- quence	TO stars	SGB	RGB	He- burning phase	AGB
5000.50	20.69	17.98	4.51	36.83	11.70	8.29
6000.50	23.07	14.00	3.75	40.06	9.77	9.35
7000.50	23.82	12.28	3.42	41.61	8.93	9.95
8000.50	24.26	10.97	3.15	42.86	8.29	10.47
8500.50	21.98	11.07	3.20	44.54	8.31	10.91
9000.50	24.46	10.15	2.98	43.61	7.97	10.82
9500.50	24.78	9.64	2.86	43.99	7.71	11.02

Table 3.4: The percentage contribution at different wavelengths from each evolutionary phase to the total integrated flux of a 13.5 Gyr metal poor  $[\text{Fe}/\text{H}] = -1.8$  population with Salpeter IMF.

integrated spectra of stellar populations. In this section I use integrated spectra of SSPs with different IMF exponents to explore the sensitivity of a set of indices to the assumed shape of the IMF. The aim is to test the predicted behaviour of known IMF-sensitive indices in the new models. The IMF variations applied for this purpose range from a MW-type IMF (Kroupa) that predicts a slight turn-over at lower masses, to a Salpeter single power-law and towards more dwarf-enriched populations with exponents  $x = 3.0$  and  $x = 3.50$  (see Equation 1.4). These are the variations considered in recent studies that suggest that massive ETGs have IMFs that deviate from that observed in the MW towards mass functions with an increasing fraction of low-mass stars.

The indices included in this test are the known IR IMF-sensitive indices (defined in Table 2.4) and additional indices in the optical range (see Table 3.5). The optical indices are TiO and CaH bands recently defined and studied by Spiniello et al. (2014) as a new set of IMF-sensitive indices (Figure 3.2). The motivation for their work was to find *bluer* IMF indicators in order to avoid the intrinsic difficulties of measuring absorption lines in the IR (contamination from telluric lines and the interstellar medium). For this purpose they used empirical stellar spectra from the MILES library to measure the ratio between the spectra of cool giant and dwarf stars at roughly the same metallicity in order to locate spectral regions with large flux differences. As a result, they identified and studied the optical indices listed in Table 3.5 which were found to be sensitive to the presence of cool stars in general with the exception of CaH1 which is strong only in high-gravity stars (the same behaviour is seen in the synthetic spectra used here). The Lick indices  $H\beta$ ,  $Mgb$ , Fe5335 and Fe5270 (Table 2.3) are also included in this analysis. These indices are used as stellar population diagnostics and are not expected to exhibit great sensitivity to the IMF.

Figure 3.3 shows the strength of the indices as a function of the shape of the IMF in populations with different ages (colours) at solar (plus signs) and sub-solar (triangles) metallicities. The sub-solar metallicity considered in this section has a total metal content  $[M/H] = -1.0$  and  $[\alpha/Fe] = +0.4$ , which corresponds to  $[Fe/H] \sim -1.31$  (Equation 1.3). The equivalent widths were calculated using Equation 2.2 and strengths are

Index	Blue continuum	Central passband	Red continuum	Sensitive to
bTiO	4742.750 4756.500	4758.500 4800.000	4827.875 4847.875	dwarfs & giants
aTiO	5420.000 5442.000	5445.000 5600.000	5630.000 5655.000	dwarfs & giants
TiO1	5816.625 5875.625	5936.625 5994.125	6038.625 6103.625	dwarfs & giants
NaD	5860.625 5875.625	5876.875 5909.375	5922.125 5948.125	dwarfs
TiO2	6066.625 6141.625	6189.625 6272.125	6372.625 6415.125	dwarfs & giants
CaH1	6342.125 6356.500	6357.500 6401.750	6408.500 6429.750	dwarfs
CaH2	6510.000 6539.250	6775.000 6900.000	7017.000 7064.000	dwarfs & giants

Table 3.5: New optical indices defined by Spiniello et al. (2014).

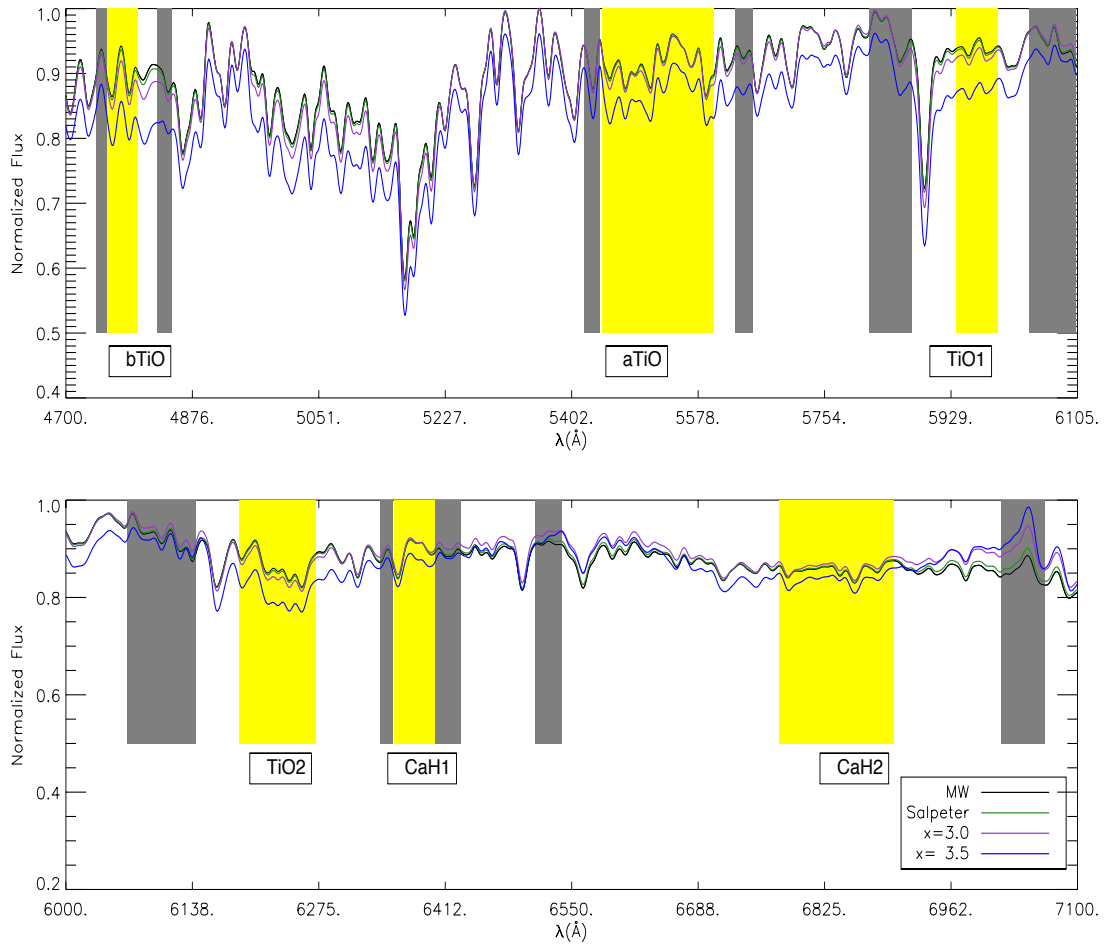


Figure 3.2: The same spectra shown in Figure 3.1 for a 10 Gyr population with varying IMF zooming in the spectral regions of the optical IMF-sensitive indices. The central passbands are shaded in yellow and the corresponding blue and red continua appear in grey to the left and right sides of the yellow regions respectively.

quoted in units of  $\text{\AA}$  except for the TiO and CaH bands that are quoted in magnitudes.

The TiO bands are abundant in the atmospheres of M-type stars and they tend to dominate the optical opacity in the spectra of low-mass stars (Bochanski et al., 2007). The strength of all the TiO bands in this test increases as the IMF steepens and the fraction of dwarf stars increases. The aTiO index has the weakest measured strengths and is the least sensitive to the steepening of the IMF. The TiO index with the highest fractional change when varying from a MW IMF to an  $x = 3.5$  IMF at solar and sub solar metallicities is the  $\text{TiO}_1$  (its percentage change is above 200%). The sensitivities to changes in the IMF of all the TiO indices increase at sub solar metallicity. Spiniello et al. (2014) found that  $\text{TiO}_2$  and bTiO are strong in cool stars in general (dwarfs and giants) and concluded that these indices used alone cannot distinguish between a bottom- or top-heavy IMF. This issue is discussed in the next Section.

The presence of CaH bands in cool stars was first investigated by Ohman (1934) who found that the intensities of the bands in the spectra of dwarfs were stronger than in giants. In Spiniello et al. (2014) the behaviour of CaH2 was found to be similar in the spectra of dwarf and giant stars whereas CaH1 was found to be a good dwarf indicator. In these new models CaH1 and CaH2 are more sensitive to IMF variations than any of the TiO bands and CaH2 is overall the most sensitive index plotted in Figure 3.3. The percentage change of CaH2 when the IMF changes from a MW to  $x = 3.5$  IMF is over 300%.

The sodium feature NaD is a strong absorption line that is mildly sensitive to the IMF in these models at solar metallicity if compared to the lines discussed so far. On the other hand, the two definitions of the NaI feature (a and b in Figure 3.3) are sensitive to the IMF with differences in their strengths but they follow similar trends with respect to IMF variations. The definition NaIb presents weaker strengths but it increases more than NaIa as the IMF steepens. This line is a good IMF indicator as it is only sensitive to the presence of cool dwarfs, expanded further in Section 3.4. Another classical IMF indicator is the FeH0.99 line (also called the Wing-Ford Band) which is known to be a relatively weak feature which is difficult to measure in systems with high velocity dispersion (Carter et al., 1986, were unable to measure the line in their galaxies despite

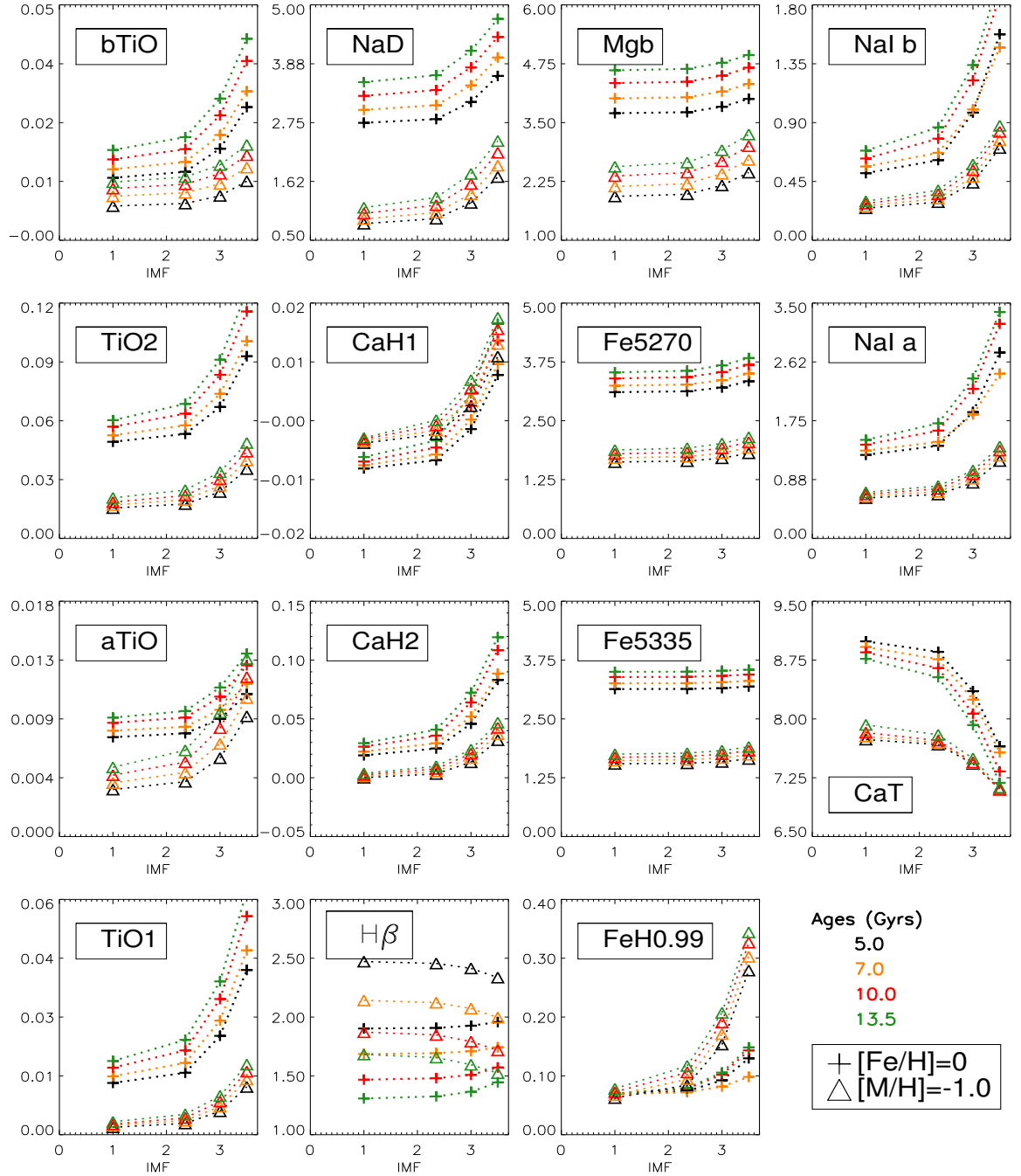


Figure 3.3: The behaviour of optical and infrared indices as a function of IMF exponent for different ages and metallicities. The x-axis indicates the IMF exponent  $x$  (Equation 1.4) except for  $x = 1$  that is used to represent the MW Kroupa multi-power law. The ages are colour-coded as labeled and the plus symbols and triangles represent solar and sub solar metallicity populations respectively. The sub-solar metallicity is quoted in terms of total metal abundance  $[M/H]$  because it is  $\alpha$ -enhanced by +0.4 and this corresponds to a total value of  $[Fe/H] \sim -1.31$ . The TiO and CaH bands are measured in magnitudes while all the other indices are in  $\text{\AA}$ .

having good S/N in that region). The new models show that the feature is sensitive to the IMF but is extremely weak (more than expected) suggesting that this line is probably not well modelled in the new PSM. This issue has been already noticed in Figure 2.6 where the synthetic spectra significantly under-predict the observed values. The line is practically invisible in the theoretical spectra, probably due to problems in the modelling of this spectral region. During private communication with the authors of the BT-Settl library it was suggested that the total band strength is not reproduced well with the available line list. The other classical IMF indicator is CaT which, as expected, responds in the opposite way to the other indices when the fraction of dwarf stars increases. Because CaT is strong in low-gravity stars, as the IMF predicts an increasing number of dwarfs their contribution to the spectra result in a weakening of the absorption feature.

The selected Lick indices were not expected to show a great response to IMF variations. Only a very mild variation can be observed in every Lick index in Figure 3.3 as the IMF becomes more bottom-heavy.

### 3.4 Contribution from different evolutionary phases

In the previous section the IMF-sensitive indices have been discussed in terms of their response to IMF variations. In this section I study which stars from the population are the main contributors to the observed integrated values of these indices. I study the fractional contribution from the different evolutionary phases (determined by the initial stellar mass) at a given isochrone age. In this way it is possible to sample which are the mass ranges that mainly contribute to the observed strengths of the features. Ideally, this means that if we trust the models and if the indices are sensitive to different mass ranges, one could determine the shape of the IMF at these specific mass ranges.

To quantify the fractional contribution I compute several integrated spectra considering different upper cut-off masses along the isochrone, using a 13.5 Gyr isochrone at solar metallicity that has a minimum initial mass  $\sim 0.1M_{\odot}$ . Figure 3.4 shows the behaviour

of the IMF-sensitive indices for a Salpeter IMF as a function of mass range.

All of the TiO bands reach their final value (green, solid line) very close to the turn-off point (blue, dashed line) which means that the giant stars do not contribute significantly to the final values of these indices. This means that for bTiO and TiO<sub>2</sub>, which are sensitive to cool giants and dwarfs (Spiniello et al., 2014), when computing the integrated spectrum of a population, the contribution from the RGB to the final integrated value is insignificant in comparison to the dwarf stars. Therefore, these indices could potentially distinguish a bottom-heavy from a top-heavy IMF. All the other IMF-sensitive indices depend on the presence of the giant stars which mainly contribute to weaken the absorption feature (except for FeH0.99 and CaT). CaT is sensitive to the presence of low-gravity stars therefore its strength builds up along the mass-range considered and is sensitive to the presence of stars in the later stages of their evolution.

All TiO, Na and CaH bands (except for aTiO and NaD that are discussed later) present similar behaviours: they are all strong in cool dwarfs with masses below 0.13M<sub>⊙</sub> (the molecular bands are over ten times stronger than their final population value and the atomic line NaI is seven times stronger) and as hotter main sequence stars are added to the population, the strengths decrease gradually. When all stars up to 0.50M<sub>⊙</sub> (effective temperature  $\sim 3900\text{K}$  and  $\log g = 4.8$ ) are taken into account in the population, the initial integrated values have dropped by  $\sim 50\%$ . This means that for these indices the observed strengths are produced by the very cool dwarfs and therefore these are effective IMF-indicators to explore the faint low main sequence stars. This behaviour is also observed independently of the chosen IMF (I repeated the same test with a bottom-heavy IMF  $x = 3.5$  and the same trend was reproduced by all the spectral features).

The aTiO and NaD lines behave differently to the features discussed above. They are also very strong in cool dwarfs but rather than following a gradual decrease in their line-strengths as main sequence stars are added to the population, these indices present a plateau in the mass range between 0.20 and 0.70 M<sub>⊙</sub>. Up to a cut-off mass  $\sim 0.73\text{M}_{\odot}$  (effective temperature  $\sim 4700\text{K}$  and  $\log g \sim 4.6$ ) both indices are more than two times stronger than their final population value. As it is the case of the other spectral lines,

stars around the TO and in later stages contribute to weaken the absorption line.

### 3.5 Age and metallicity effects

To fully understand the behaviour of the IMF-sensitive indices it is important to look at possible degeneracies with age and metallicity. The variations of each index due to metallicity effects are plotted in Figure 3.3 using plus signs to indicate scaled-solar metallicity models and triangles for total metal content given by  $[M/H] = -1.0$  and an  $\alpha$ -enhancement = 0.4. The variations of age are colour coded as indicated in the figure. It is clear from the plots that all the IMF-sensitive indices are also sensitive to the age and metallicity of the population.

Populations with older ages produce stronger absorption lines for all the IMF-sensitive indices except for CaT at solar metallicity. The CaT line is sensitive to the presence of low-gravity stars and as a population ages its strength decreases because the population is increasingly dominated (in number) by the dwarf stars along the main sequence. At a given IMF, as the age of the population increases so does the number ratio of dwarf-to-giant stars.

There is a clear degeneracy between IMF variation and age because an increase in the age of the population has the same effect on the indices as a steepening of the IMF at constant age. In order to quantify and compare age and IMF effects I looked at the behaviour of the indices in two situations:

- i. changing the age of the population from 10 to 13.5 Gyr, at solar metallicity and MW-IMF.
- ii. changing the IMF of the population from a MW to a Salpeter IMF, at 13.5 Gyr and solar metallicity.

To simplify I discuss the behaviour of only two indices: NaIb and TiO<sub>1</sub>. In situation i, NaIb changes by +9.6% and TiO<sub>1</sub> by +10%. In situation 2, NaIb changes by +26% and TiO<sub>1</sub> by +29%. In this example the effect on the indices of changing the IMF is almost

[Fe/H]=0.0, 13.5 Gyr SSP, Salpeter IMF

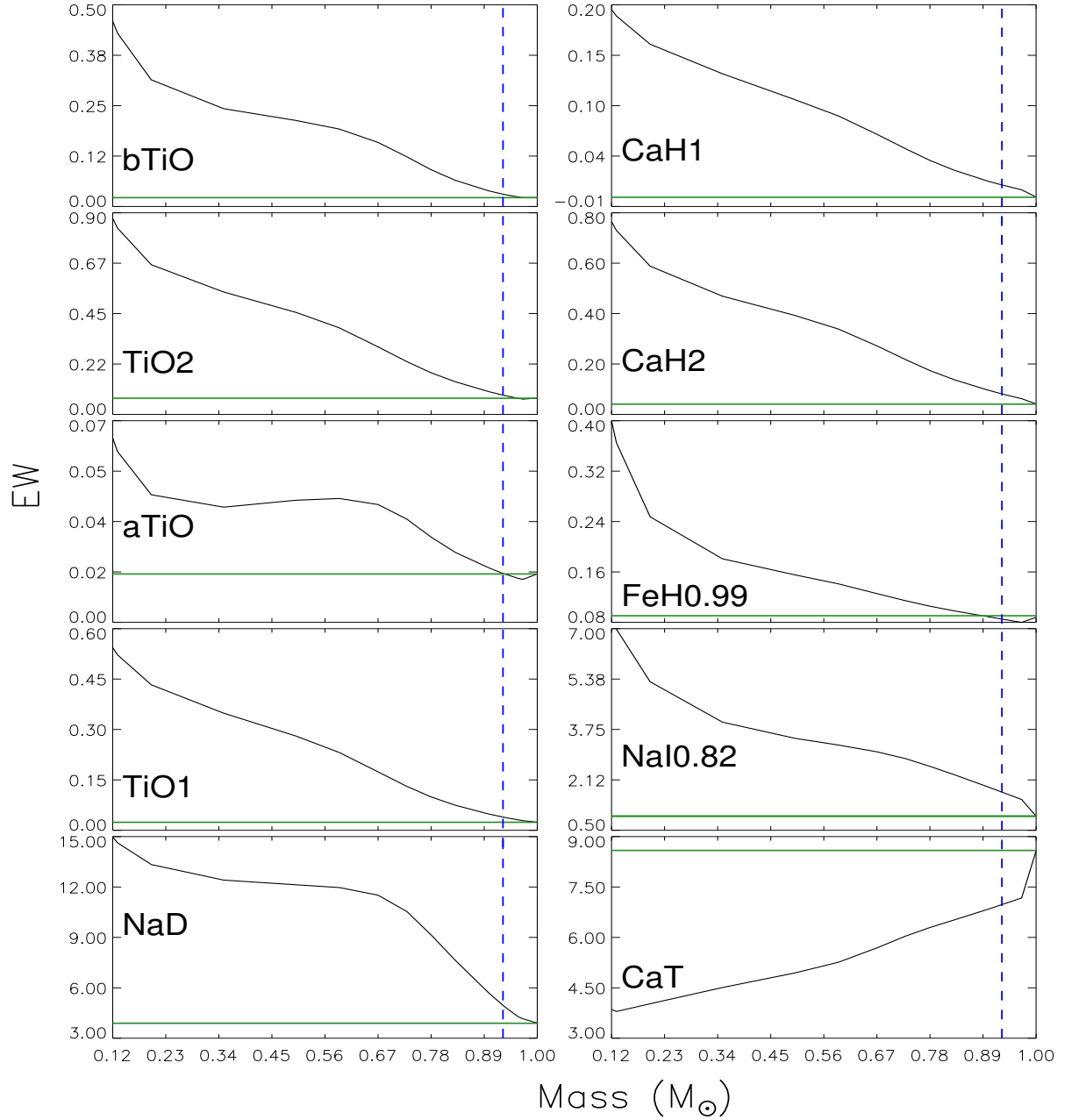


Figure 3.4: Fractional contribution of the evolutionary phases to the integrated value of the IMF-sensitive indices. Along the x-axis we plot the upper cut-off mass used to compute the integrated spectra. The maximum mass  $0.98M_{\odot}$  accounts for the whole isochrone. The blue dashed line indicates the turnoff mass ( $\sim 0.93 M_{\odot}$ ) and the solid green line indicates the final integrated value obtained when considering the entire isochrone. Only the NaIb definition is plotted here.

three times stronger than the effect produced when changing the age of the population. A similar behaviour is observed in all the IMF-sensitive indices at solar and sub-solar metallicities. At sub-solar metallicity the same relative effect between age and IMF is observed. Schiavon et al. (2000) explored the behaviour of NaI, FeH (WFB), CaT and a different region of the TiO bands with respect to age and metallicity and found that FeH and CaT were almost insensitive to age. In these new models CaT is also the least sensitive index to the age of the population (less than 6% when changing from a 5 to 13.5 Gyr population). The percentage change by which an IMF-sensitive index gets stronger due to age variations in the range considered is in every case significantly smaller than the percentage change produced by a steepening of the IMF slope.

All of the IMF indicators are stronger at solar metallicity with the exception of CaH1 and FeH0.99. This overall behaviour is expected since the spectral features considered here are all metallic lines and at  $[M/H] = -1.0$  the metal content is reduced with respect to solar. CaH2 and TiO<sub>1</sub> are the most sensitive indices to the metallicity of the population, while CaT is the least sensitive to the metal content. Spiniello et al. (2014) found a TiO<sub>2</sub> dependence on metallicity that is also seen in our models, especially as the IMF becomes steeper. The CaH1 line presents a different behaviour and the strength of the line increases as the total metallicity of the population goes down. This is in agreement with Spiniello et al. (2014) who observed that the line is weaker in  $\alpha$ -enhanced populations at solar  $[Fe/H]$  (i.e. larger total metallicity  $Z$ ). On the other hand, the reasons for a stronger FeH0.99 line at sub-solar metallicity are not clear as one would expect to detect a weaker line as the total  $[Fe/H]$  content decreases and this is what had been observed in previous studies (Schiavon et al., 2000) (Conroy & van Dokkum, 2012a). This can be another associated problem to the poor modelling of this spectral feature in the synthetic spectra used in the PSM.

All IMF-sensitive indices are sensitive to the total metallicity of the population, i.e. there is a degeneracy with metallicity. When changing the metallicity of a 13.5 Gyr population with MW-IMF, from solar to  $[M/H] = -1.0$ , all the IMF indices except CaT change by at least  $\sim 50\%$ . The metallicity change explored in this work is quite large ( $\Delta[Fe/H] = -1.35$ ) and it would be interesting to see the effect of changing the iron

content [Fe/H] by  $\sim \pm 0.5$  but the models are not available.

## 3.6 The impact of isochrone uncertainties

The previous sections have defined the IMF-sensitive indices and investigated which are the mass ranges they are probing. This section explores which assumptions and/or uncertainties from stellar evolution predictions may bias IMF determinations using the spectral features defined above. For this purpose I consider the effect of uncertainties in the effective temperatures predicted by the stellar isochrones and the overall effect of changing the stellar evolution predictions by using another set of isochrones.

### 3.6.1 Temperature uncertainties

The question addressed here is: what is the effect of changing the temperature of the stars along the isochrone on the IMF sensitive indices defined in the previous section? Changing the predicted temperatures will shift the location of the isochrone in the HRD (see Figure 2.10) and therefore the spectra associated with each isochrone point will vary.

The temperature differences are introduced by adding/subtracting 100, 150 and 200K to the temperature value predicted by the isochrone. Temperature changes are considered for two cases:

1. For the whole isochrone. Effective temperature predictions for stellar isochrones vary depending on the stellar evolution models (libraries of isochrones) used, see Section 3.6.2.
2. For the RGB (all isochrone points with surface gravity  $\log g \leq 3.0$ ). The temperature of the RGB is very sensitive (more so than for the main sequence) to the calibration of the mixing length which is a free parameter and a great source of uncertainty in stellar evolution models.

Unlike the rest of the work in this thesis, these two tests are performed on the version of the PSMs discussed in Section 2.3 which include bright and cool giants (see Figure 2.12). The reason for using this version of the models in this test is because the cool and bright giants are potentially the stars in the population more likely to be affected by temperature uncertainties.

The calculations were made on 13.5 Gyr SSP at solar metallicity and MW-type IMF. The effects on the individual spectral features are shown in Figures 3.5 and 3.6 for the whole isochrone and RGB respectively. The plus signs in the figures indicate the integrated value of the index at the given temperature uncertainty plotted along the x-axis. The horizontal dotted lines indicate the integrated values for different shapes of the IMF with the original temperature predictions.

As expected, the variation of the indices due to temperature differences is larger when applied to the whole isochrone than to the RGB alone. In the case of the whole isochrone, if cooler isochrone temperatures are assumed the predicted values of all the TiO bands and NaD when matched with the original isochrone would retrieve a steeper-than-Salpeter IMF. The rest of the indices have a similar behaviour to what is seen in the RGB scenario. In the RGB case, the FeH0.99 line is the most sensitive to temperature variations. The behaviour of this line as a function of IMF exponent when predicted with the PSMs that include bright giants is the reverse as expected from previous studies and the original PSM used in this work. The line gets weaker as the fraction of dwarf stars in the population increases. The reverse behaviour would be expected if we consider this line to be sensitive to the dwarf population. This discrepancy is another reason to believe that there are problems with the modelling of this line. On the other hand, CaH1 is nearly insensitive to temperature uncertainties along the RGB. When cooler temperatures are assumed, NaI has the opposite behaviour to the rest of the indices. This line would retrieve a bottom-light IMF when matched to the original isochrone. For the rest of the indices, when cooler temperatures are assumed the predicted values can affect IMF determinations when matched with the original isochrone between a MW and a Salpeter IMF but not beyond. This implies that the RGB stars contribute to those indices (i.e. to their continuum).

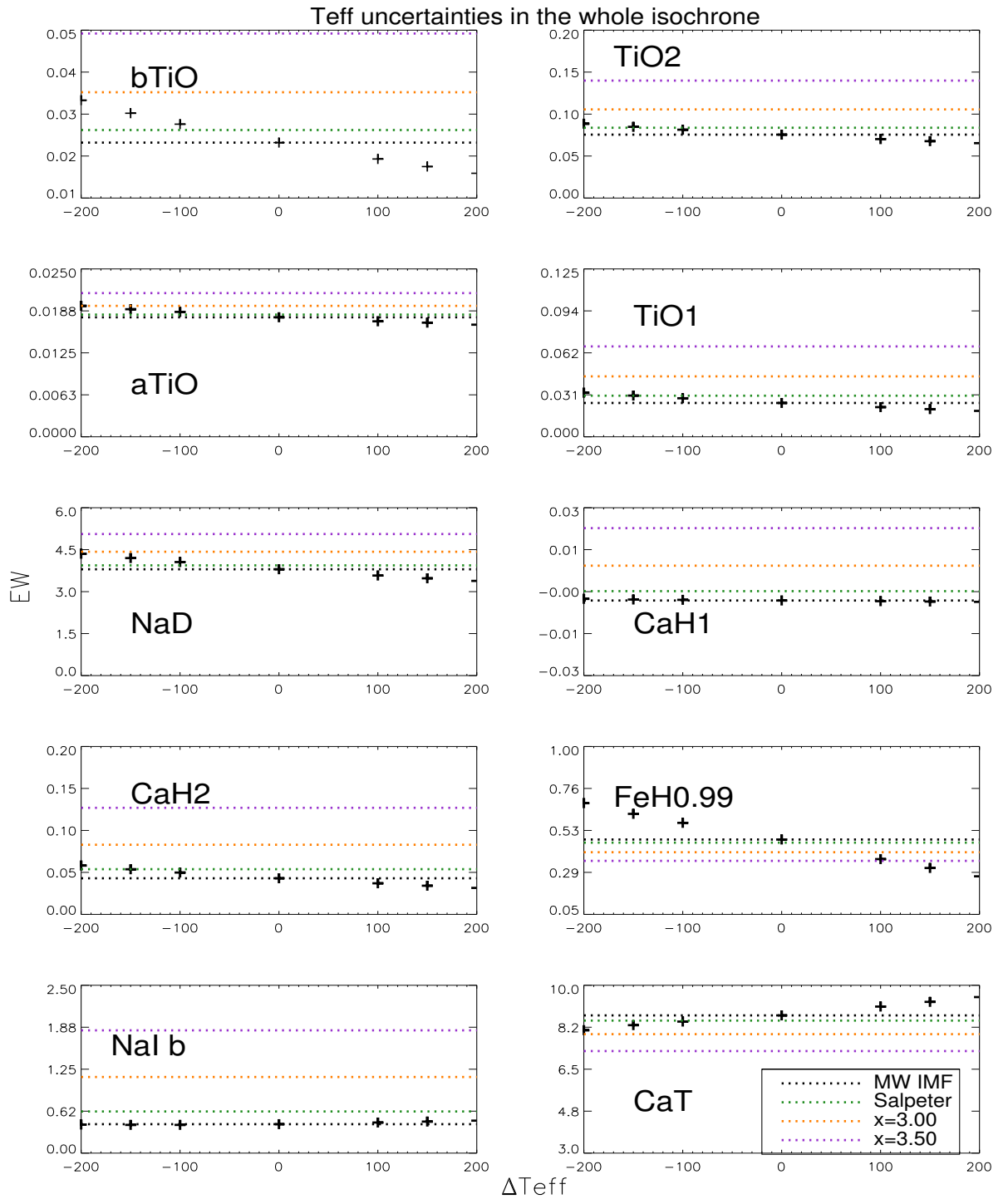


Figure 3.5: The integrated value of the indices when a change in the temperature of the whole isochrone is applied shown by the plus signs. The temperature uncertainties are reproduced by adding and subtracting 100, 150 and 200K from the original effective temperature ( $T_{eff}$ ) predicted by the isochrone (when  $\Delta T_{eff} = 0$ ). Isochrone points with original temperatures below 3700K are not changed. The dotted lines are the integrated values for different shapes of the IMF using the original temperature predictions of the isochrone.

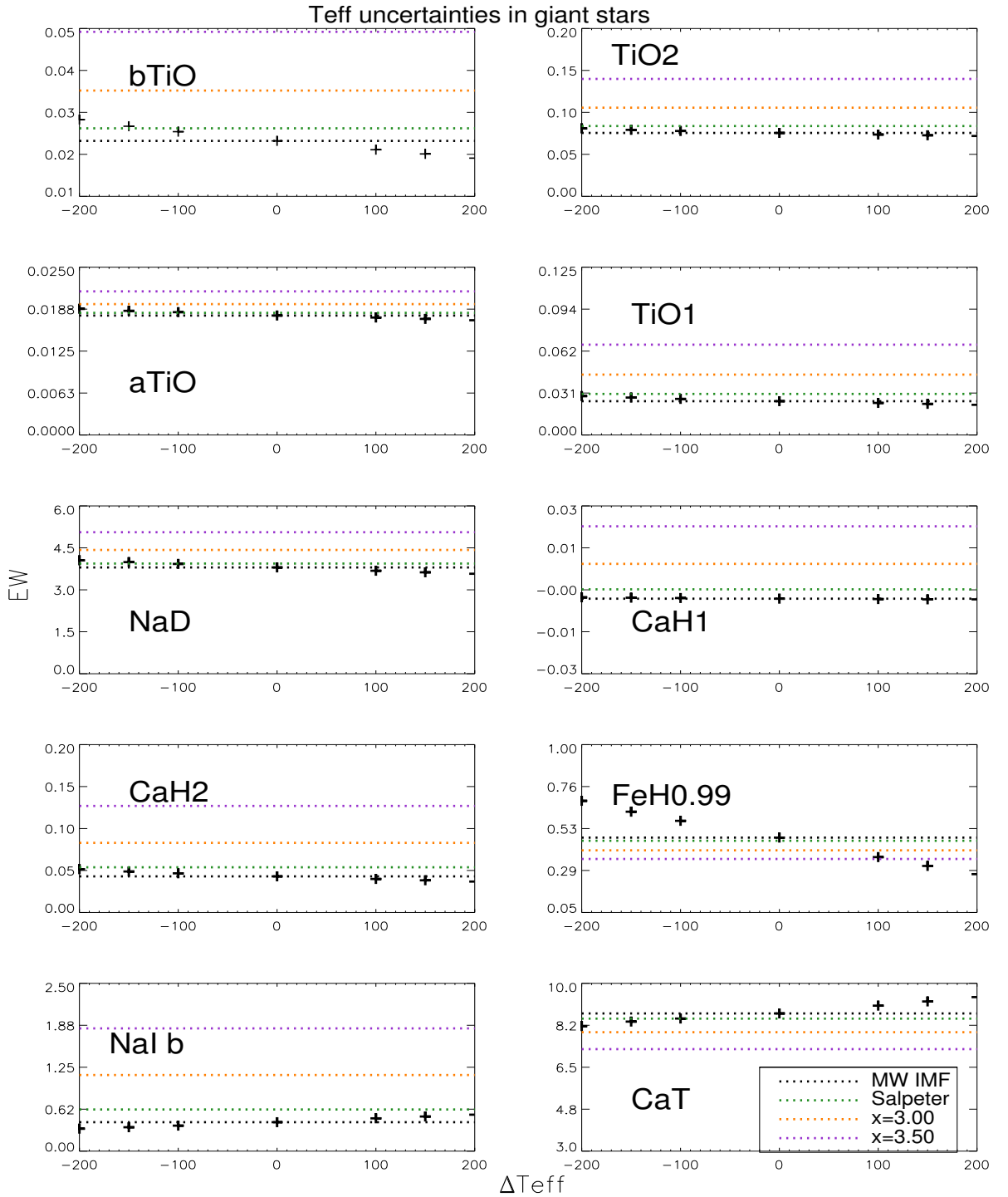


Figure 3.6: The integrated value of the indices when changing the temperature of the red giant branch only are shown by the plus signs. Temperature uncertainties were applied to all stars with  $\log g \leq 3.0$  by adding and subtracting 100, 150 and 200K from the original effective temperature ( $T_{eff}$ ) predicted by the isochrone ( $\Delta T_{eff} = 0$ ). The dotted lines are the integrated values for different shapes of the IMF using the original temperature predictions of the isochrone.

### 3.6.2 Stellar evolution predictions

Another way to understand how model dependent are the conclusions drawn from these indices is to study the effect of changing the library of stellar isochrones. For this purpose I use the version of the Padova models described in Marigo et al. (2008). This Padova set was calculated based on the Grevesse et al. (1993) solar abundances. The main difference between the BaSTI+ and Padova isochrones is some of the input physics and assumptions regarding convection. The isochrones are plotted in Figure 3.7 where it is possible to see how their predictions differ (examples of these differences for a 10 Gyr population are quoted in Table 3.6). Another key difference for our study between the two libraries is the value of the minimum mass of the main sequence illustrated in Figure 3.7. The BaSTI+ models have been extended to  $M_{min}=0.10M_{\odot}$  (see Section 2.1) whereas the Marigo et al. (2008) prescriptions start at  $M_{min}=0.15M_{\odot}$ . For the following analysis we use the same mass range in order to understand the effect of solely changing the stellar evolution predictions. For the following test the TP-AGB phase (which evolves very fast) from the Padova models is not taken into account.

Parameter	Padova	BaSTI+
Low-MS $T_{eff}$ at $\log g \sim 5.0$ (K)	3560	3570
TO $T_{eff}$ (K)	5730	5790
RGB $T_{eff}$ at $\log g \sim 3.0$ (K)	4690	4750
RGB $T_{eff}$ at $\log g \sim 1.0$ (K)	3780	3780
TO mass ( $M_{\odot}$ )	1.00	0.98
Tip RGB mass ( $M_{\odot}$ )	1.05	1.06
He-burning luminosity ( $L/L_{\odot}$ )	1.62	1.67

Table 3.6: The main visible isochrone differences between the BaSTI+ and Padova stellar evolution predictions for a 10 Gyr population.

I constructed PSMs using the Padova isochrones at solar metallicity for different ages and IMF exponents and produced the same test as in Section 3.3. In Figure 3.8 is plotted the behaviour of the indices as a function of IMF exponent for the two sets of PSMs. The panels show the predictions using BaSTI+ models (plus signs and solid lines) and Padova models (triangles and dashed lines) at the same isochrone ages (colours). At first sight the general behaviour of the indices with varying IMF is similarly reproduced by both models. For a given age, both PSMs show an increase in the IMF-sensitive indices as the IMF steepens (except for CaT) and very mild or no variation in the Lick

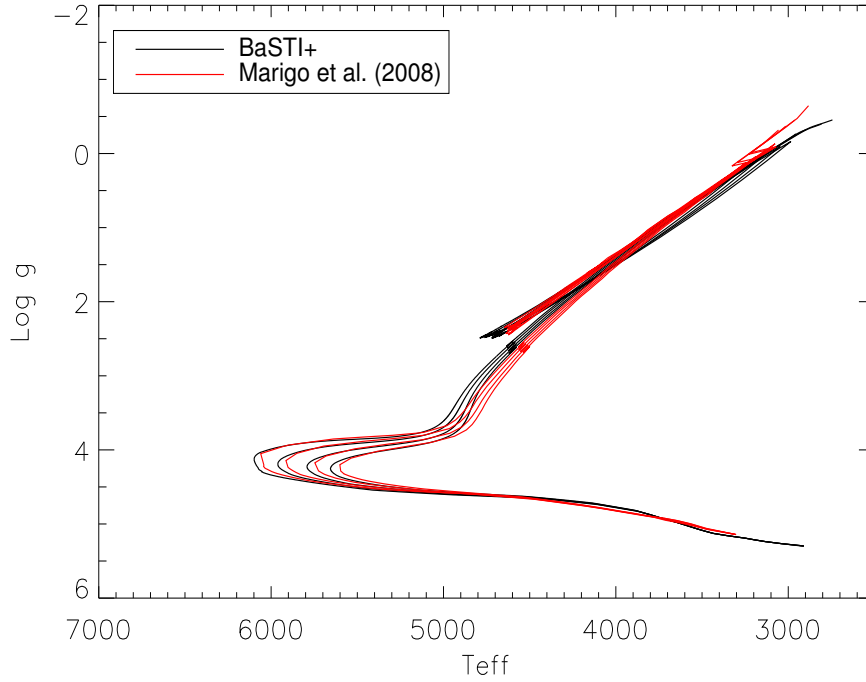


Figure 3.7: The BaSTI+ and Padova Marigo et al. (2008) isochrones at solar metallicity with ages 5, 10, 7 and 13.5 Gyr. The Padova isochrones predict cooler turnoffs and RGB temperatures for all ages. For simplicity the post-AGB phase from the Padova models is not shown here as it is not taken into account in this work. The different minimum mass between libraries is visible at the low mass end of the main sequence.

Index	MW	Salpeter	x=3.0	x=3.5
bTiO	13.51	15.38	-21.05	-20.21
aTiO	-4.00	-3.70	-8.33	-10.00
TiO <sub>1</sub>	-5.08	-6.25	-11.11	-14.83
TiO <sub>2</sub>	-0.21	-1.52	-5.58	-10.03
CaH2	-6.94	-10.00	-15.29	-19.23
CaH1	-3.62	-4.72	-14.12	-147.06
NaD	4.48	4.13	2.93	1.11
NaIa	-0.29	-3.55	-10.28	-18.09
NaIb	-0.80	-6.19	-14.38	-21.61
FeH0.99	-1.13	-3.39	-9.32	-16.78
Fe5335	2.10	2.07	2.03	1.89
Fe5270	2.04	1.91	1.51	0.72
Mgb	4.67	4.55	4.12	3.34
H $\beta$	-4.17	-4.22	-4.40	-4.88
CaT	0.04	0.36	1.37	3.19

Table 3.7: The percentage change produced when changing a 5 Gyr isochrone from BaSTI+ to the Padova predictions. The values are calculated by computing the difference between the indices produced by each PSM at a given value of the IMF and are normalized by the value from the BaSTI+ PSM.

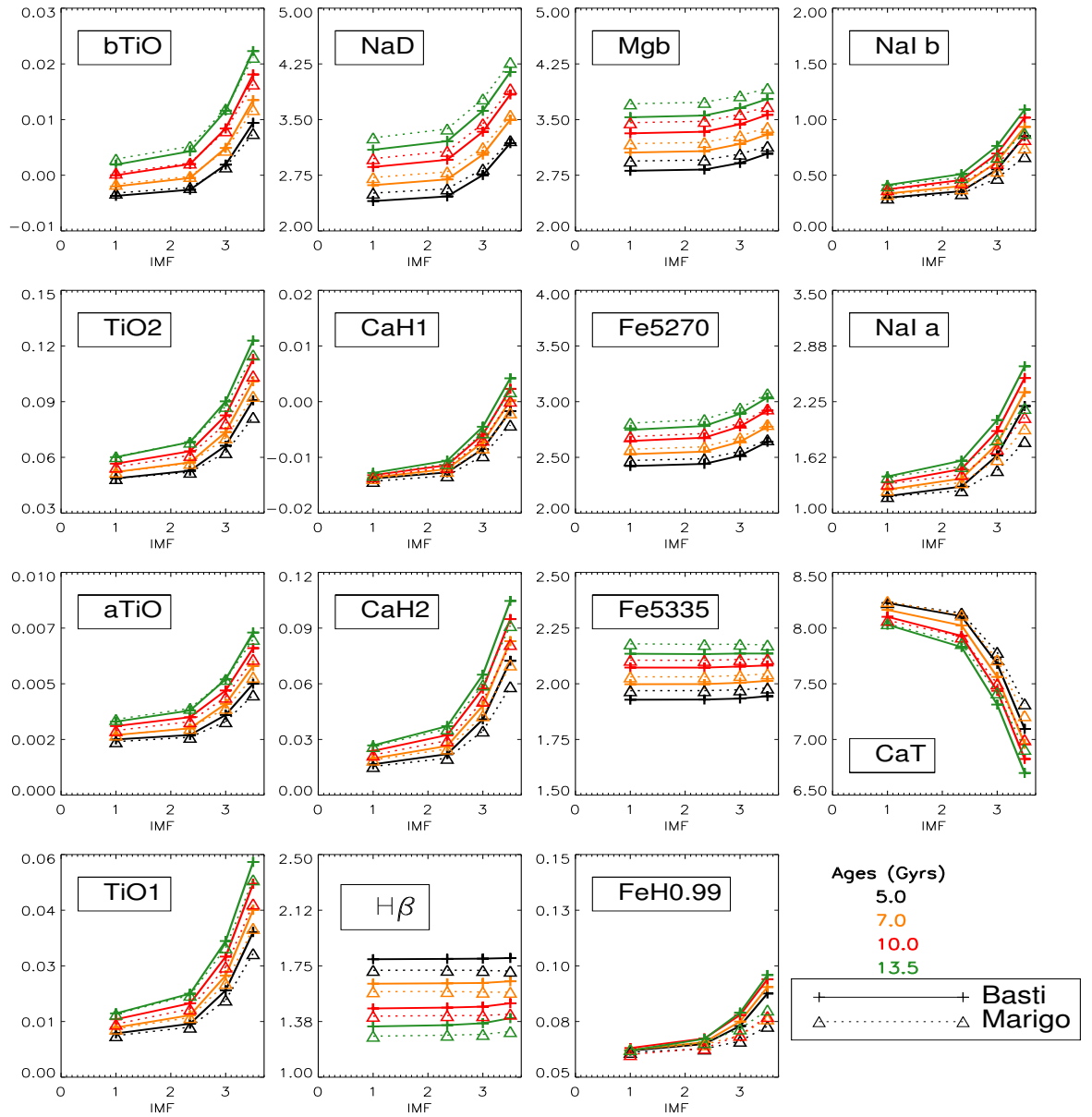


Figure 3.8: The behaviour of the indices as a function of IMF shape in the two PSMs. The BaSTI models are plotted using plus signs and solid lines and the Padova models are indicated with triangles and dashed lines. All PSMs are at solar metallicity and ages colour-coded as indicated.

indices. On the other hand, the strength of the indices at a given IMF vary slightly between the models. As an example, if we consider the index CaH2 (which was shown to be very sensitive to the IMF in Section 3.3) the strength produced with a MW-IMF in a 13.5 Gyr population when using the BaSTI+ models is reproduced by the Padova version for a younger population ( $\sim 10$  Gyr) and a Salpeter IMF.

To quantify the variations amongst the two sets of PSMs and taking the BaSTI models as the fiducial models in this study, Table 3.7 shows the percentage change of the indices for each value of the IMF in a 5 Gyr SSP. Changing the isochrones at any IMF-exponent produces differences in the observed EW that are at most  $\sim \pm 25\%$ , except for CaH1 that appears to be the most sensitive index to the choice of isochrones. All IMF-sensitive indices except bTiO and NaD, decrease with respect to the strengths observed using BaSTI+. For comparison, in the BaSTI+ PSM when the IMF changes from MW to Salpeter in a 5 Gyr population, the IMF-sensitive indices all increase by values below 20% (except for CaH2 that changes by 30%). NaD and bTiO are the only two indices that change in the same direction in both situations and by a similar amount.

### 3.7 Summary and conclusions

In this chapter I have explored the sensitivity of various spectral features to changes in the IMF using the new PSM. I have investigated possible degeneracies with age and metallicity and model uncertainties.

- In the new PSM the IMF-sensitive features respond in ways that are consistent with what has been observed by other authors using other PSMs (Spiniello et al., 2014). When considering IMF changes from a MW to a bottom-heavy IMF ( $x = 3.5$ ), in this new PSM the most IMF-sensitive indices are TiO<sub>1</sub> and CaH2.
- All the IMF-indices used in this chapter are strong in low-mass stars with  $\log g \gtrsim 5.0$  and their strengths can be used to probe this fraction of the population in

the integrated spectrum of an SSP. aTiO and NaD seem to be unaffected by stars in the mass range between 0.20 and 0.70  $M_{\odot}$ .

- All the IMF indices are also sensitive to the age and metallicity of the population. In the examples explored here, the responses of the indices to age and metallicity were weaker than those resulting from changes in the IMF from MW to Salpeter.
- Variations in the effective temperature of the isochrone affect the behaviour of the IMF-sensitive indices. When assuming cooler temperatures and a MW-IMF, the TiO bands and NaD predictions yield values that when matched with the original model, correspond to a bottom-heavy IMF.
- Reasonable uncertainties in the effective temperatures of giant stars can lead to a misinterpretation of the shape of the IMF between MW and Salpeter using the TiO bands NaD and CaH2 as IMF indicators. The variations however do not reproduce the strengths observed in more bottom-heavy IMFs.
- Changing the stellar evolution models used to compute the PSM affects the zero-point of the indices while the behaviour with IMF variations appears to be similar.

# Chapter 4

## Application to globular clusters and early-type galaxies

This chapter presents the final application and original motivation for this new set of PSMs. In this chapter I use the models to derive estimates of the integrated properties (ages, metallicities and IMF) of extragalactic globular clusters and early-type galaxies.

The chapter is divided into two parts: 1. analysis of globular cluster spectra and 2. analysis of early-type galaxies from line indices. In all cases the data have been obtained from the literature. All estimates are derived under the assumption that these populations can be modelled as SSPs. When possible, the new model predictions are compared to previous published results.

In the globular cluster analysis I address two well known problems in the modelling of these populations: dynamical evolution and the morphology of the HB. I study these problems in the context of IMF determinations.

For all data sets the first step is to find estimates of the metallicity and age of the population in order to use the appropriate PSM to study the IMF. The ages and metallicities were studied using the well known diagram  $H\beta$ -[MgFe] which clearly disentangles the effects of age and metallicity. In order to study the level of  $\alpha$ -enhancement I use the Fe5406-[MgFe] combination when possible. In cases where the available data does

not include the Fe5406 line I use another Fe line as an indicator of  $[\text{Fe}/\text{H}]$ . These plots are discussed later on in the text.

## 4.1 Tests on globular clusters

Globular clusters (GCs) have long been idealized as the empirical counterpart of theoretical SSPs. In that view, GCs are the classical testbeds to calibrate stellar evolutionary models as well as PSMs. However, increasingly accurate spectroscopic and photometric observations in the last decades have challenged this view and today the general consensus is that GCs host multiple generations of stars, e.g. Gratton et al. (2012a). From the spectroscopic point of view, advances in instrumentation (larger telescopes, multi-fiber optics) have enabled studies on individual cluster stars at different evolutionary stages that revealed that variations in the light-element (C, N, O, Na, Mg, Al) abundances with respect to halo field stars of the same  $[\text{Fe}/\text{H}]$ , affect the majority of the stars inside each cluster, see Gratton et al. (2004) for a detailed review. Resolved spectroscopic observations have shown that GCs exhibit chemical anti-correlations within cluster members with respect to the average cluster abundances typically between C-N, O-Na and Mg-Al (Gratton et al., 2012b). These variations cannot be explained by evolutionary effects and they imply that the majority of cluster stars were formed from matter that was already processed by a first generation of stars. The second generation of stars exhibits a decrease of C, O and Mg and an increase of N, Na, and Al with respect to the first generation stars. It is not clear which are the mechanisms responsible for these chemical anomalies. A possible explanation is mass-loss from first generation, fast-rotating massive stars and intermediate-age AGB stars. In this scenario, the second generation of stars forms from matter that is a mixture of the ejected material (which contains the chemical anomalies observed) and gas with the initial chemical composition of the cluster (which formed the first generation of stars). In the last decade, the multiple population scenario has been supported by high-precision photometry available from the Hubble Space Telescope. Resolved photometry has revealed CMDs with visible splits in the evolutionary sequences (MS, SGB and RGB),

e.g. Bedin et al. (2004), Piotto (2009).

Although globular clusters are no longer regarded as populations of coeval stars with the same initial chemical composition, they still remain the best systems to calibrate SSP models. Even if there are more than one generation of stars, the spread in ages tends to be fairly small ( $\leq 0.1$  Gyr) and it is not expected to produce significant effects in the integrated spectra of the population. Metallic lines used to derive the total metallicity  $Z$  of the population, are not affected by the small age spread of the second generation stars (Trager & Somerville, 2009). On the other hand, Coelho, Percival & Salaris (2011) showed that it is possible to predict which Lick indices are affected by abundance anti-correlations and found that the only indices affected by this phenomenon are: G4300, Ca4227, CN1, CN2 and NaD (G4300 and Ca4227 decrease while CN bands and NaD increase). Cassisi et al. (2013) also found that even in the chemical anti-correlation scenario if the sum of CNO elements within the population is kept constant in comparison to standard models (with no anti-correlation and  $\alpha$ -enhanced abundances), the isochrone predictions are the same as the standard models.

In the following sections I use integrated spectra of M31 GCs from Caldwell et al. (2011), courtesy of R. Schiavon, to study the global properties of the populations (age, metallicity and IMF) predicted by the new PSMs. Caldwell et al. obtained integrated spectra for more than 300 globular clusters in the Andromeda galaxy and determined mean cluster metallicities and ages using line indices. The observations were taken with the Hectospec multifibre spectrograph on the 6.5 m Multi Mirror Telescope (MMT) in Arizona, between 2004 and 2007. The spectra cover a wavelength range between 3700 and 9200 Å and have a resolution of 5Å. Table 4.1 contains a summary of the parameters of the sample of GCs used in this work selected to match the metallicities of the model grid. The flux distributions of these clusters are plotted in Figure 4.1.

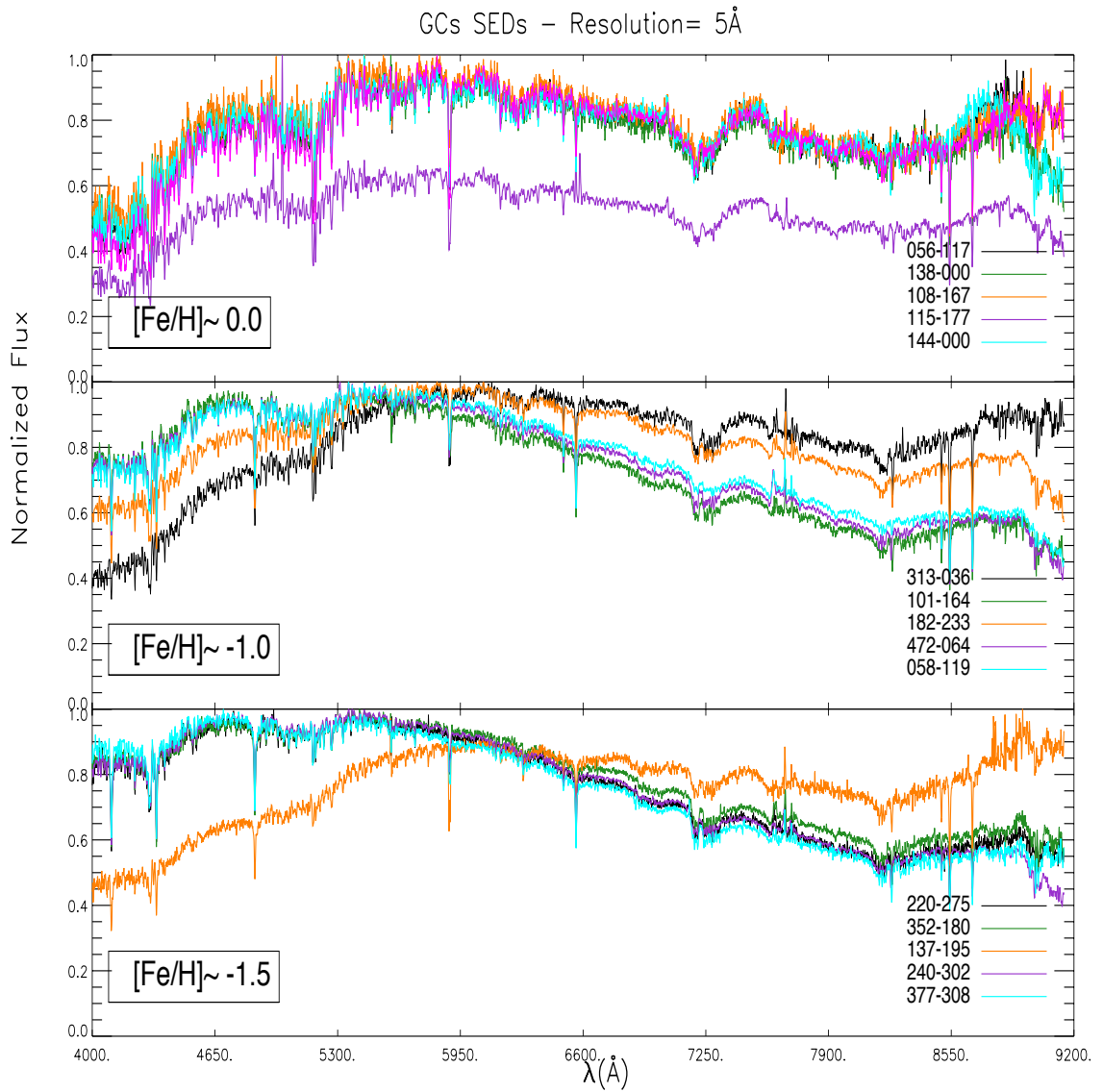


Figure 4.1: Spectral Energy Distributions (SEDs) of the GC sample. The spectra are plotted in three panels corresponding to the different  $[\text{Fe}/\text{H}]$  as derived by C+2011. The GC SED are colour-coded as indicated in the key, where the names are those from C+2011.

Cluster	[Fe/H]	Age (Gyr)	Log M ( $M_{\odot}$ )
184-236	0.14	**	5.35
056-117	0.00	**	5.39
108-167	+0.02	10.4	5.36
115-177	+0.06	**	5.84
138-000	-0.04	7.4	5.50
144-000	+0.08	11.7	5.58
101-164	-1.02	**	5.40
182-233	-1.03	**	6.24
313-036	-0.99	**	5.91
472-064	-0.98	**	6.07
058-119	-1.05	**	6.19
137-195	-1.47	**	5.58
220-275	-1.48	**	5.56
240-302	-1.48	**	6.07
377-308	-1.48	**	5.26
352-180	-1.52	**	5.60

Table 4.1: Parameters of the M31 globular clusters used in this work as derived by C+2011. Measured ages have an uncertainty  $\pm 2$  Gyr.

\*\* Ages could not be determined because the clusters fall outside their PSM grid, see Section 4.1.1.

### 4.1.1 Age and metallicity estimates

In Chapter 3 I showed that the IMF indices are degenerate to the age and metallicity of the population. In order to derive IMF estimates it is important to first obtain accurate estimates of these two parameters. In this section I compare the age and metallicity estimates derived by Caldwell et al. (2011) (hereafter C+2011) with those predicted by the new PSMs.

I employ Lick-type indices that can break the degeneracy between age and metallicity to generate a model grid in an index-index plot. Rabin (1982) demonstrated that it is possible to separate age and metallicity effects from the integrated spectra by plotting a hydrogen Balmer feature against a metallic line (examples of these plots used to derive SFHs were introduced in Section 1.2.2). Here I plot the commonly used combination of  $H\beta$  to trace the age and [MgFe] as the metallicity indicator. The [MgFe] index is a

good indicator of the total metallicity  $Z$  of the population and is calculated as follows:

$$[MgFe] = \sqrt{\frac{Fe5270 + Fe5335}{2}} \times Mgb \quad (4.1)$$

where all the indices are defined under the Lick IDS system (see Table 2.3). I measured these indices in the theoretical integrated spectra generated by the PSMs for various ages (between 5 and 13.5 Gyr) and metallicities with scaled-solar abundances ( $[Fe/H]=0.0$ ) and  $\alpha$ -enhancement ( $[Fe/H]=0.0, -1.31, -1.81$ ) with an assumed MW-type IMF. All the integrated spectra from the models were convolved to match the resolution of the clusters. The resultant grid is shown in Figure 4.2.

### Age comparison

C+2011 used index-index grids constructed with the SSP models from Schiavon (2007) (hereafter S07) to derive age estimates. The S07 SSP models are based on the empirical spectral library by Jones (1999) and the Padova isochrones for scaled-solar metallicities (Girardi et al., 2000) and with  $\alpha$ -enhancement (Salasnich et al., 2000). C+2011 used models for a range of ages between 0.9 and 14 Gyr and a metallicity range:  $-1.3 \leq [Fe/H] \leq +0.2$ . Ages were derived by matching the line strengths measured in the GCs to those predicted by the SSP models. To do this they employed an algorithm that successively matches pairs of indices between the observed values and the ‘best-fits’ from the models (for details on this procedure see Section 4 of their paper).

The resultant age estimates are quoted in Table 4.1 and have an estimated uncertainty  $\pm 2$  Gyr. Ages for the GCs that fall outside the grid could not be determined. This affects most of the clusters in my sample. C+2011 found that three of the six clusters with  $[Fe/H]=0.0$  in the sample have  $H\beta$  values that fall outside the grid. Their youngest cluster in this sample is 7.4 Gyr old (cluster 138-000). The remaining two clusters (108-167 and 144-000) have ages  $>10$  Gyr according to their models.

I derived ages for the solar- $[Fe/H]$  clusters in the sample using the new PSMs from this work and assuming that these clusters have scaled-solar metal mixtures. Most

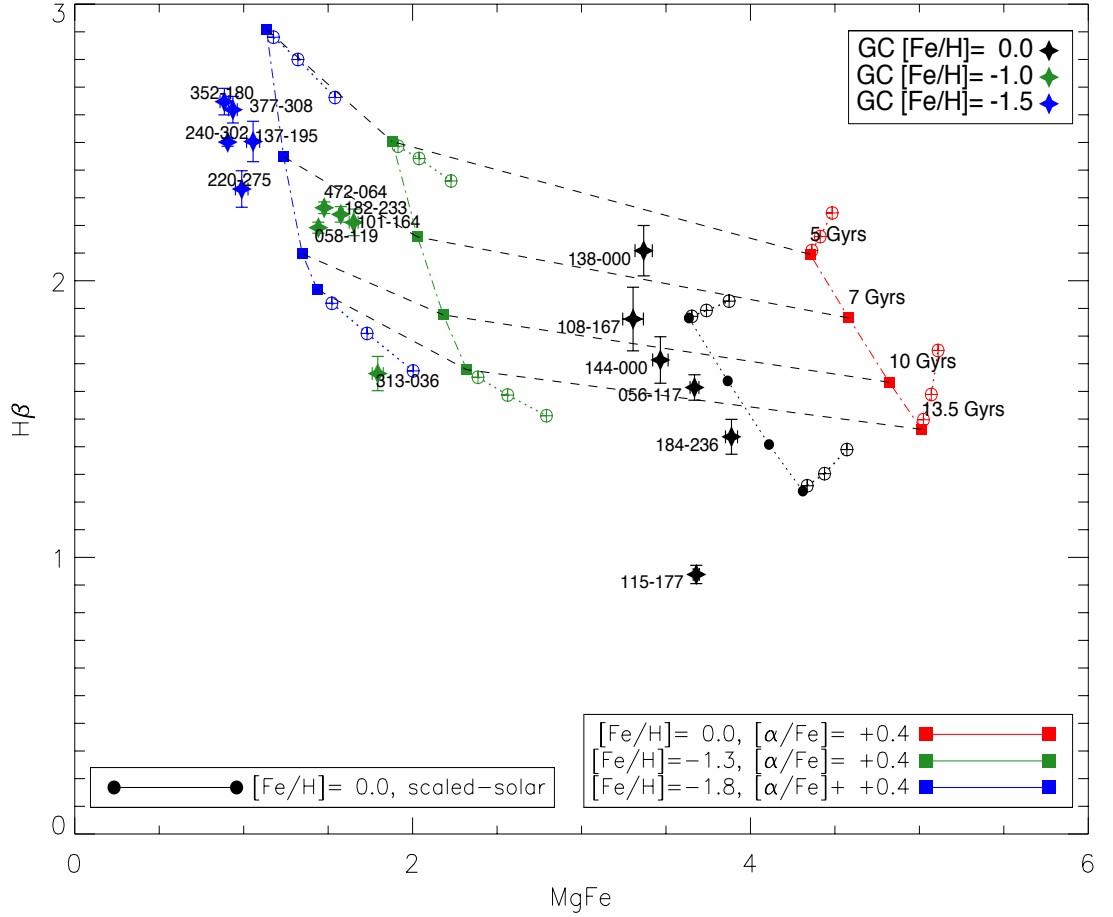


Figure 4.2: Age and metallicity grid predicted by the PSMs compared to the M31 GCs (stars). Each point or square in the grid represents an SSP with a specific age and metallicity and a Kroupa MW-type IMF. The synthetic high-resolution integrated spectra were convolved with a Gaussian with  $\text{FWHM} = 5 \text{ \AA}$  to match the resolution of the GC spectra. The filled circles represent the set of models for scaled-solar abundances available at  $[\text{Fe}/\text{H}] = 0.0$  and the filled squares are  $\alpha$ -enhanced models for  $[\text{Fe}/\text{H}] = 0.0, -1.31, -1.81$ , where  $[\alpha/\text{Fe}] = +0.4$ . The black-dashed lines denote constant age and the colour dotted-dashed lines denote constant metallicity. In the grid, age increases from the top down and metallicity decreases from right to left. The coloured stars represent the measured indices in the M31 clusters and are colour-coded according to their metallicity as estimated by C+2011. The errors were calculated using the program LECTOR (Vazdekis, 2011). For the younger and older ages of each metallicity, I plotted the model predictions for different exponents of the IMF. The circles with the cross in the middle added to the standard grid represent the effect of changing the IMF-exponent to Salpeter,  $x = 3.0$  and  $x = 3.5$ . For all the SSPs as the IMF changes from Kroupa to  $x = 3.5$  the metallicity indicator  $[\text{Mg}/\text{Fe}]$  gets stronger. The effect on  $\text{H}\beta$  depends on the metallicity.

of the clusters lie between the model predictions for 5 and 10 Gyr (see Figure 4.2). The youngest in the sample appears to be 138-000 (in agreement with C+2011) but it lies outside the PSM grid suggesting it must be younger than 5 Gyr. The oldest cluster appears to be 115-177 which presents the lowest value of  $H\beta$  and hence has an unphysical age as estimated by the models. The integrated spectrum of this cluster has a distinctive shape when compared to the other solar- $[Fe/H]$  clusters (see Figure 4.1). C+2011 already pointed out that the spectrum of this cluster shows strong  $[OIII] \lambda 5007$  emission lines and it did not follow the Fe5015-Fe5270 correlation observed in all the other M31 clusters (Figure 7 in their paper). This weak  $H\beta$  measurement can be due to an excess of absorption lines in the bandpasses neighbouring the central passband that are not observed in the other clusters at the same  $[Fe/H]$ . Or most likely has  $H\beta$  emission falling in the absorption line.

At lower  $[Fe/H]$ , the PSMs in this work predict ages between 7 and 10 Gyr for all clusters with estimated  $[Fe/H] = -1.0$ , except 313-036 which lies outside the grid towards older ages. The lowest metallicity clusters of this sample (blue stars in Figure 4.2) appear even younger ( $\leq 7$  Gyr) as estimated by the models, except 220-275 that appears to have an age between 7 and 10 Gyr. The younger ages in these low-metallicity clusters can be due to the presence of blue Horizontal-Branch (HB) stars. Blue HB stars are hot and they contribute to the Balmer lines affecting age derivations using  $H\beta$  (Lee et al., 2000). The presence of a blue HB component can explain the younger ages observed at  $[Fe/H] \leq -1.0$  as was also noted by C+2011. This issue is further discussed in Section 4.1.3.

Overall, with the PSMs from this work I have been able to estimate ages for most of the clusters in the sample. The new PSMs extend towards lower metallicities than the S07 models used in C+2011, and more clusters fall inside the model grid than in the original work. For the clusters with  $[Fe/H] = 0$  the new PSMs predict younger ages than the S07 models by at least  $\sim 5$  Gyr. A possible explanation for this inconsistency can be that these clusters have  $\alpha$ -enhanced abundances according to my models. At fixed age,  $H\beta$  is stronger for an  $\alpha$ -enhanced population (see Figure 4.2). I study this possibility in the next Section where I study the metallicities of the clusters.

In the new PSMs, at fixed [Fe/H] the  $H\beta$  line is stronger in  $\alpha$ -enhanced populations than in scaled-solar ones. This means that for a population at fixed [Fe/H] the  $\alpha$ -enhanced models predict older ages than the scaled-solar ones. Schiavon (2007) on the other hand, had found that  $\alpha$ -enhanced models predict weaker lines (and younger ages) than scaled-solar ones. The reason for this discrepancy is still unknown and is an interesting question for future research.

### **Metallicity comparison**

C+2011 estimated the metallicity of the clusters using two methods: the index-index technique described above and using a correlation between absorption lines (Lick indices) and [Fe/H] abundances from clusters in the MW. The values that are discussed here are those obtained using the MW correlation. C+2011 used a spectral library of MW clusters from Schiavon et al. (2005) and the metallicity scale from Carretta & Gratton (1997) to derive a relation between the Lick iron lines, Fe5270 and Fe5335, and [Fe/H] (Figure 8 in their paper). This relation was then used to calibrate the Lick-measurements from the M31 clusters and derive their [Fe/H] abundances. This technique assumes that M31 and MW clusters have the same age. The derived values appear in Table 4.1 and have uncertainties  $\pm 0.1$ - $0.2$ . C+2011 compared their estimates with other spectroscopic studies that derived metallicities for some of the clusters in their sample and from HST CMDs. The offset with respect to the integrated spectra determinations from the literature was very small ( $\sim 0.08$  dex) and the rms of the differences with respect to the CMD derivations was 0.2 dex. The [Fe/H] values derived using the MW-scale and the S07 PSMs index-index grid, have a mean offset between 0.05 and 0.08 dex.

The metallicity scale from Carretta & Gratton (1997) was re-calibrated in Carretta et al. (2009) using higher-resolution spectra obtained with the UVES optical spectrograph on the VLT. They observed 13 MW clusters from their previous work and found that the new [Fe/H] estimates were systematically lower than the previous estimates by an average of  $\sim 0.19$  dex and  $\sigma = 0.11$  dex. The differences observed were larger at lower

metallicities.

I refer back to Figure 4.1 to compare the estimates from my PSMs to those derived in C+2011. At first glance it is clear that the new PSM grid predicts lower metallicities than the original estimates from C+2011. Taking into account the re-calibration by Carretta et al. (2009) my predictions for the solar  $[\text{Fe}/\text{H}]$  clusters (black stars) are in good agreement with the values derived by C+2011. For the metal-poor clusters, I still find on average lower  $[\text{Fe}/\text{H}]$  values than those published.

In the previous Section I suggested that the  $[\text{Fe}/\text{H}]=0$  clusters might be  $\alpha$ -enhanced. In order to study the metal mixture of these clusters, in Figure 4.3 I plot  $\text{Fe}5406-[\text{MgFe}]$  for both clusters and models. The feature Fe5406 is the preferred indicator to measure  $[\text{Fe}/\text{H}]$  because it is very sensitive to the iron content of the population and is practically insensitive to the  $\alpha$ -element abundances (Trager et al., 1998). Percival et al. (2009) compared Fe5406 and  $[\text{MgFe}]$  measurements from high-resolution spectra of Galactic GCs with PSM predictions and found that it is possible to study the degree of  $\alpha$ -enhancement of a population with this index combination. In a  $\text{Fe}5406-[\text{MgFe}]$  plot, a population with a given  $[\text{Fe}/\text{H}]$  and  $\alpha$ -enhancement will have the same Fe5406 strength as a scaled-solar population of the same  $[\text{Fe}/\text{H}]$  but because it has a larger total metallicity  $Z$  (larger  $[\text{MgFe}]$ ) it appears to the right of the scaled-solar population. In this way  $\text{Fe}5406-[\text{MgFe}]$  is an excellent combination to distinguish an  $\alpha$ -enhanced population from a scaled-solar one. All  $[\text{Fe}/\text{H}]=0$  clusters except 184-236, have Fe5406 strengths below the scaled-solar models suggesting that they have slightly sub-solar  $[\text{Fe}/\text{H}]$  and  $\alpha$ -abundances that are enhanced with respect to solar ( $0 < [\alpha/\text{Fe}] < +0.4$ ). The more metal-poor clusters (green and blue stars) appear to be in good agreement with the model predictions and I therefore conclude that they are  $\alpha$ -enhanced with  $[\alpha/\text{Fe}] \sim +0.4$ .

To conclude this section I summarize briefly the results found. Using the PSMs in this thesis, I found that the  $[\text{Fe}/\text{H}]=0$  clusters have estimated ages younger than those found by C+2011. I also found that these clusters have slightly sub-solar  $[\text{Fe}/\text{H}]$  and super-solar  $[\alpha/\text{Fe}]$ . Models with these abundances would predict older ages for the same clusters. At lower metallicities, the clusters appear increasingly younger as  $[\text{Fe}/\text{H}]$

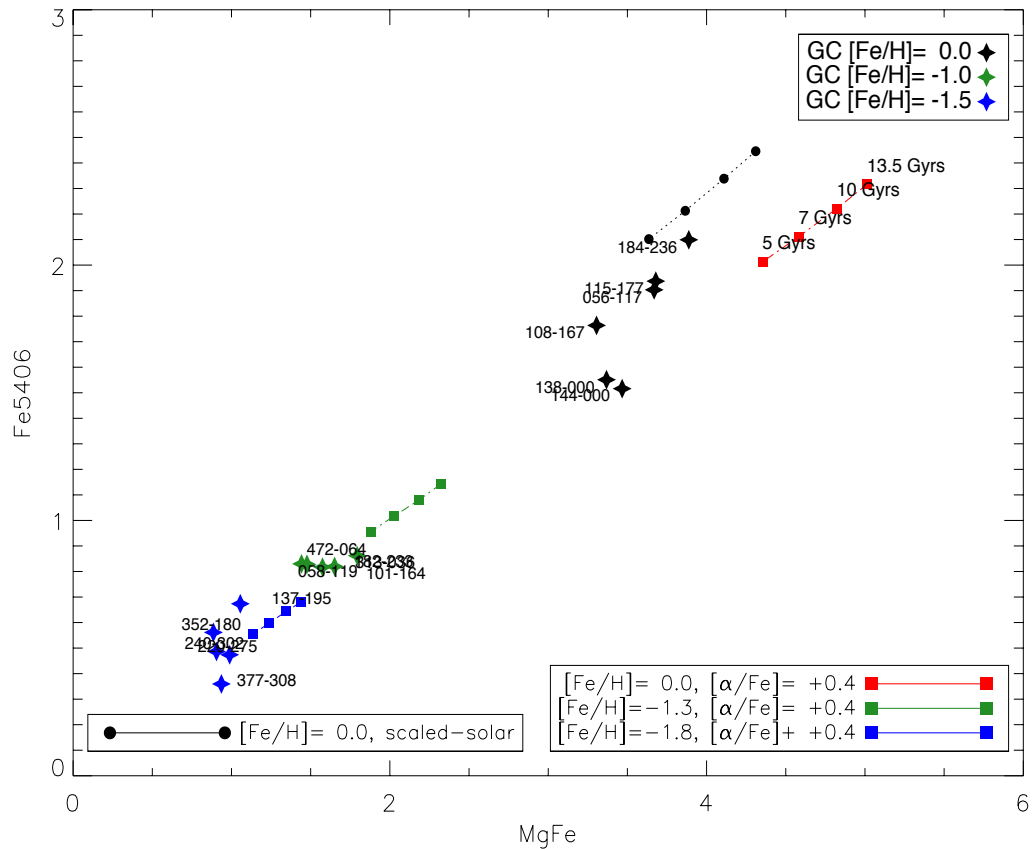


Figure 4.3: Fe5406 and  $[\text{MgFe}]$  plot to study the  $\alpha$ -abundances of the GCs. At fixed  $[\text{Fe}/\text{H}]$ , an  $\alpha$ -enhanced population has larger  $[\text{MgFe}]$  strength than the scaled-solar mixture. The models and clusters are colour-coded as indicated in the Figure. Models with the same metallicity are joined with a line and each point specifies an SSP with a characteristic age and MW-IMF. Older ages always produced larger Fe5406 strengths.

decreases. A possible explanation for this can be the presence of a blue HB component. Clusters with  $[\text{Fe}/\text{H}] \leq -1.0$  are consistent with  $\alpha$ -enhancement.

In figures 4.4 and 4.5 I show comparisons between a globular cluster spectrum and the modelled spectrum derived from the PSMs for the closest metallicity in terms of  $[\text{Fe}/\text{H}]$ . Figure 4.4 shows the solar metallicity comparison and Figure 4.5 shows the  $[\text{Fe}/\text{H}] = -1.0$  comparison. The globular cluster spectra has uncertain flux calibration which can explain some of the discrepancy observed between the modelled and observed spectra. The strength of the spectral indices are not well matched by the modelled spectra and this will affect the predictions derived from the models. The discrepancies observed between the theoretical and the empirical spectra can be due to uncertainties in the theoretical libraries which are a consequence of uncertainties in the model atmospheres calculations and in the atomic and molecular line lists.

### 4.1.2 Dynamical evolution of GC: the model perspective

When studying stellar clusters it is important to take into account their dynamical evolution which ultimately affects the integrated spectra and colours of the population. After their formation, clusters evolve internally towards a state of equipartition of energy. As stellar encounters take place and stars undergo two-body relaxation, the kinetic energy between the stars balances out eventually leading to a state of mass-segregation within the cluster. Mass segregation is produced when high-mass stars (with lower average speeds than low-mass stars) develop orbits at smaller radii from the centre of the cluster and low-mass stars concentrate towards the periphery.

Throughout their lifetimes, clusters interact with their environment and are subject to disruption events which affect their mass budget. Disruption events are produced when the cluster encounters an external tidal field, e.g. tidal shocks during crossings through the galactic disc or bulge, that produce the removal of stellar mass or gas. These events can destroy fully or partly the system in a single episode or it can be a gradual process (cluster dissolution in a smooth tidal field). According to Lamers et al. (2006) depending on the time-scale of these events, the consequences for the cluster are

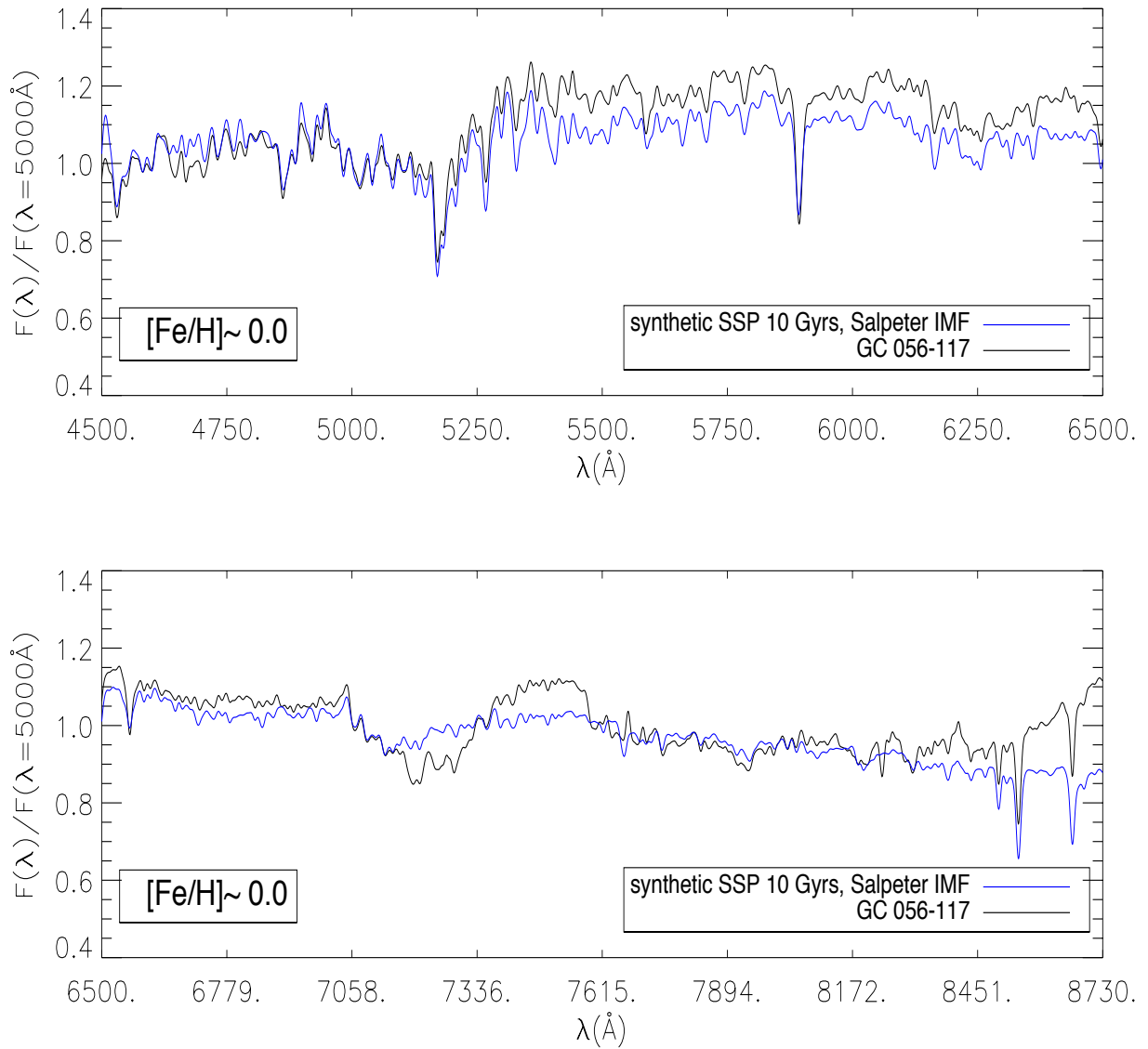


Figure 4.4: Comparison between the observed spectrum of a solar globular cluster and the modelled spectrum for a 10 Gyr SSP with Salpeter IMF,  $[\text{Fe}/\text{H}]=0$  and scaled-solar metallicity. To facilitate the comparison both spectra have been convolved to  $10\text{\AA}$  FWHM. The fluxes were normalized at  $5000\text{\AA}$ .

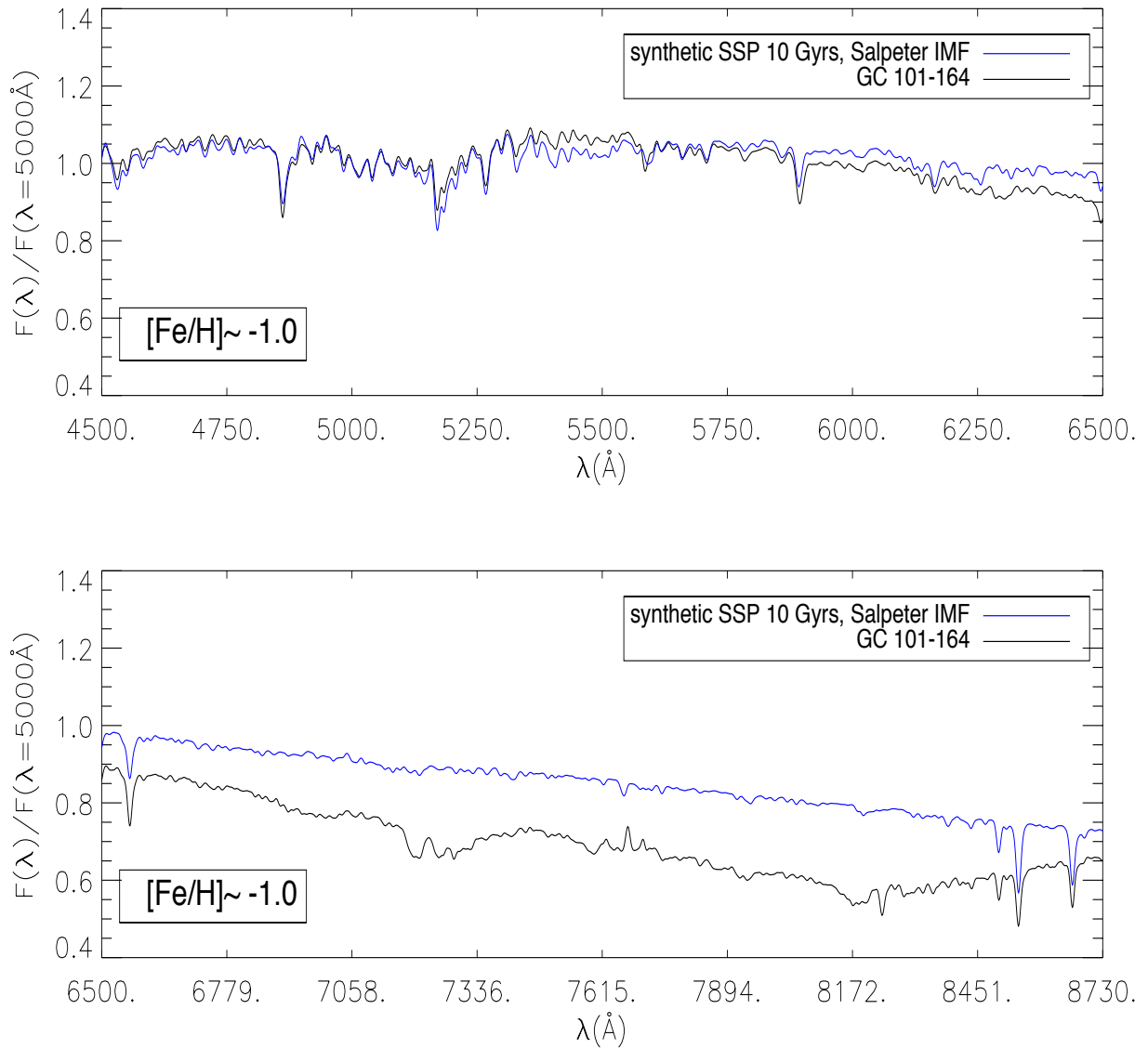


Figure 4.5: Comparison between the observed spectrum of a metal poor globular cluster and the modelled spectrum for a 10 Gyr SSP with Salpeter IMF and  $[\text{Fe}/\text{H}] = -1.0$ . To facilitate the comparison both spectra have been convolved to  $10\text{\AA}$  FWHM. The fluxes were normalized at  $5000\text{\AA}$ .

two-fold: 1. before mass segregation, stars of different masses are removed from the cluster; 2. after mass segregation, low-mass stars are preferentially removed because of their location away from the centre of the cluster. Dynamical evolution affects the number ratio of dwarf-to-giant stars and this means that the mass function (MF) of the population is no longer fixed by its initial value (IMF) but it is a time-dependent variable. The evolution of the MF has an impact on all the observable properties of the population and the derived SFH and should be taken into account when modelling the integrated properties of star clusters.

In order to take into account the effects of disruption in the theoretical modelling of cluster populations, Anders et al. (2009) used  $N$ -body simulations of clusters in tidal fields together with PSMs to derive a time-dependent representation of the MF. In their formalism, the IMF exponent is a time-dependent variable that is a function of the age and the total disruption time ( $t_{95\%}$ ) of the cluster. The total disruption time  $t_{95\%}$  is the time taken to remove 95% of the total initial mass of the cluster. Anders et al. derived two expressions to represent an evolving MF according to the mass range under consideration :

$$M \leq 0.3M_{\odot}$$

$$\alpha(t) = \alpha_{IMF}(0) - 0.1345\gamma + 1.7986\gamma^2 - 1.8121\gamma^3 + 1.2181\gamma^4 + 0.000003215\gamma t \quad (4.2)$$

$$M > 0.3M_{\odot}$$

$$\alpha(t) = \alpha_{IMF}(0) - 0.08389\gamma + 1.9324\gamma^2 - 0.4435\gamma^3 + 0.734\gamma^4 + 0.000014143\gamma t \quad (4.3)$$

where  $\alpha$  represents the slope of the mass function and is equal to  $x - 1$  ( $x$  in Equation 1.4),  $t$  is the cluster age in Myrs and  $\gamma = t/t_{95\%}$ . Previous studies based in  $N$ -body simulations had derived formulas for a time-dependent MF only for stars with  $M \leq 0.5M_{\odot}$ , e.g. Baumgardt & Makino (2003), Kruijssen (2008). Anders et al. on the other hand, found that dynamical evolution affects stars with higher masses as well. The total disruption time depends on the mass of the cluster and on the orbit. Depending on the orbit, the cluster will be at a given distance from the Galactic centre which determines

the strength of the external tidal field (the strength of its gravitational pull). The larger the mass of the cluster, the longer the disruption timescale. At the same time, the stronger the external tidal field, the shorter the disruption timescale will be. In order to use this formalism to predict the SFH of a star cluster, an estimate of the disruption time should be obtained by considering the mass, location and dynamics of the cluster as well as the strength of the tidal field around it. These details are not always available (especially for extragalactic objects) which makes it very difficult to produce realistic models of GCs. Kruijssen & Mieske (2009) derived the dissolution timescales due to two-body relaxation and disc shocking (the main mechanisms that produce cluster dissolution) for a sample of 24 Galactic globular clusters using their orbital parameters to study M/L ratios. They found that for a cluster with mass  $10^6 M_{\odot}$  the dissolution timescale ranges from 8-300 Gyr.

From the PSM perspective it is possible to study the effect of dynamical evolution on the global properties of the population. Anders et al. (2009) studied the effect on the integrated colours of the population. In this case I am interested in the effect on the spectral features sensitive to the IMF (discussed in Chapter 3) which has never been studied before. I applied equations 4.2 and 4.3 to an arbitrary SSP assuming different values of the total disruption time. Figure 4.6 shows the predictions for the IMF-sensitive indices in a 7 Gyr population with a Salpeter IMF as it undergoes dynamical evolution for different disruption times (represented by the black line). The coloured lines are the values for the time-independent IMFs as labeled in the diagram. The range of disruption timescales applied is the one derived by Kruijssen & Mieske (2009) for Galactic globular clusters .

When the disruption times are long enough (i.e. larger than the age of the Universe) and the effect of dynamical evolution on the MF is negligible, all indices meet the predictions for a Salpeter, time-independent, IMF (the black line merges with the green-dashed line in Figure 4.6). For disruption times  $8 \leq t_{95\%} \leq 30$  Gyr, the cluster is depleted of low-mass stars and the strengths of all the IMF-sensitive indices decrease. In this  $t_{95\%}$  range the present-MF of the cluster appears as a MW-type IMF and even more “bottom-light” as indicated by the IMF-sensitive indices.

[Fe/H]=0.0, 7 Gyr SSP, Salpeter IMF, FWHM= 5A

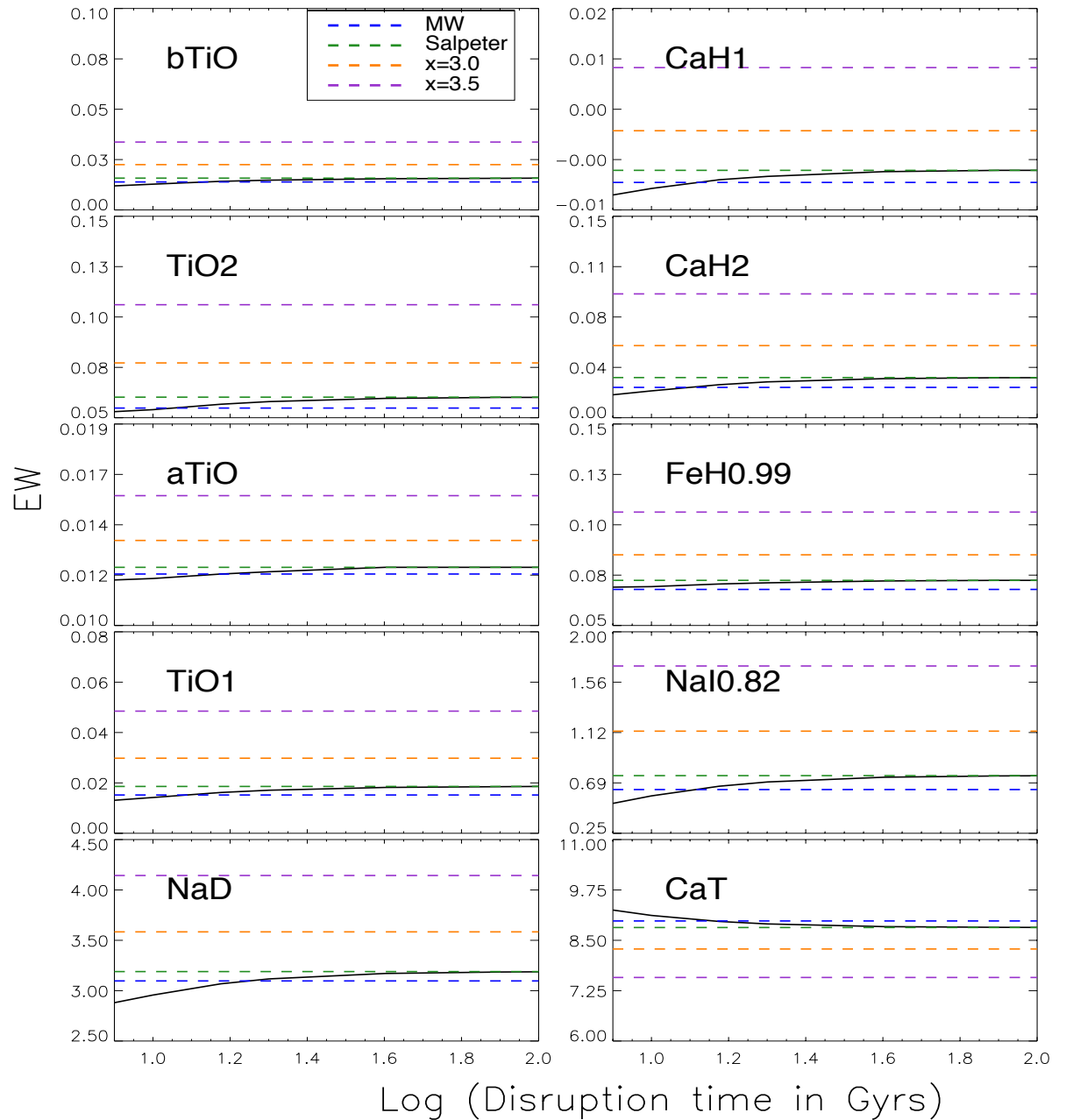


Figure 4.6: The effect of dynamical evolution on the IMF-sensitive indices assuming the range of disruption timescales calculated by Kruijssen & Mieske (2009). The black solid line indicates the predicted behaviour at a given disruption time. The colour-lines indicate the value of the indices for the different IMFs without dynamical evolution.

Shorter disruption times at fixed age increase the variation of the IMF with time ( $\gamma$  in Equations 4.2 and 4.3) and hence the number of stars removed from the cluster. As more stars are removed from the cluster the dwarf-sensitive indices become weaker because all the low-mass stars are essentially removed from the population. This explains the behaviour of the indices in Figure 4.6.

This study showed how the individual indices are affected by dynamical evolution. This effect will be revisited in the next Section where I introduce the effect in a model grid used to determine the IMF of stellar populations. The next study will enable a broader understanding of how dynamical evolution may affect IMF predictions.

### 4.1.3 Index-index plots to explore the IMF of the M31 GCs

In this section I use the index-index combinations in the optical and infrared studied in Spiniello et al. (2014) and Spiniello et al. (2012) respectively, to explore the behaviour of the PSMs and estimate the present-day MF of the M31 GCs. The index-index combinations used in this Section include the IMF-sensitive indices discussed in Chapter 3. These combinations were chosen by Spiniello et al. (2012, 2014) for their ability to break the degeneracy of the IMF with age and metallicity and were originally used to study the IMF of early-type galaxies.

The analysis is divided into two parts: the first section is restricted to present the behaviour of the models in the index-index plots and the second part includes the clusters and discusses the derivation of their present-day MF. Because we do not have enough information to estimate the disruption timescales of the clusters, the aim is to find an indication of the present-day MF without trying to recover the IMF (no account of dynamical evolution).

#### Model grid for the optical and infrared index-index diagrams

The previous sections discussed two problems encountered in the modelling of GCs: dynamical evolution and the morphology of the HB. From the point of view of the

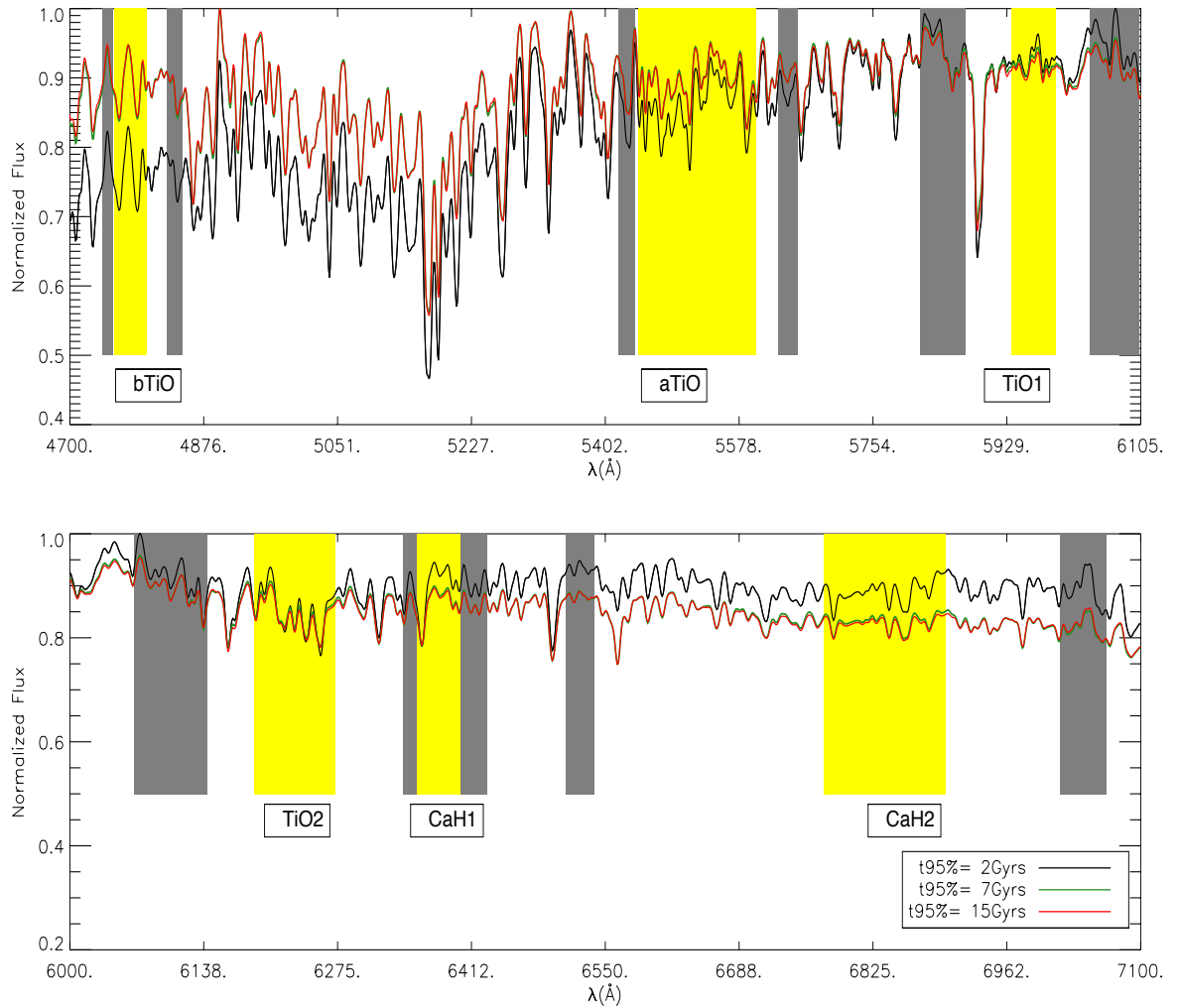


Figure 4.7: SEDs for three of the dynamically-evolved 7 Gyr SSPs, colour-coded as indicated in the lower panel. Highlighted in yellow are the central passbands for the indices as indicated in the figure. The adjoining sidebands are highlighted in grey. The original spectra were convolved to a resolution  $\text{FWHM} = 5 \text{ \AA}$ . All indices except CaH1, shown here all become stronger as  $t_{95\%}$  becomes shorter.

models, it is possible to study these two problems parametrically and in this section I explore their effect in the index-index diagrams used for IMF determinations.

The motivation to include dynamical evolution in the IMF analysis is straightforward: by changing the ‘original’ IMF it affects the behaviour of the IMF-indices and the estimates derived from their strengths. As in the previous section, dynamical evolution is applied on a 7 Gyr SSP initiated with a Salpeter IMF using the same disruption timescales from Section 4.1.2 (1.55, 2, 5, 7, 10, 15, 20, 40, 80 and 100 Gyr).

On the other hand, it is well known that the HB morphology affects age determinations derived from the Balmer lines and this issue has been extensively studied in the literature e.g. Percival & Salaris (2011), Cenarro et al. (2010). But we do not know the effect it has on the IMF-indices and how it can affect IMF determinations from index-index plots.

HB morphology was first mentioned in Section 4.1.1 as a possible explanation for the younger ages observed in the metal-poor clusters because we cannot predict the morphology of the HB for a given age and metallicity and the different morphologies affect  $H\beta$ . Accurate observations of Galactic GCs have shown that HB morphology is primarily determined by the metallicity of the cluster: metal-poor populations typically host hot (blue) HB stars and more metal-rich populations tend to have a red HB component, e.g. Arp et al. (1952), Sandage & Wallerstein (1960). Subsequent investigations have shown varied morphologies at fixed metallicity suggesting that there is at least one other parameter which affects the evolution of HB stars inside clusters (Lee et al., 1994). The nature of the secondary parameter(s) is still a matter of debate and possible candidates include cluster ages, initial helium abundance and mass loss efficiency, or a combination of them.

Stars evolving in the HB phase are burning He in their cores and H in a shell around the core. The bolometric luminosity of the HB is fairly constant and is fixed by the mass of the He-burning core at the He-flash. The HB is populated by low-mass stars and the stellar temperatures in this phase are mainly determined by the initial chemical composition and total mass of the star (Salaris & Cassisi, 2005). From the modelling

point of view, increasing the mass-loss efficiency at fixed metallicity has essentially no effect on the position of the RGB in the HRD but affects the position of the HB shifting it towards the blue. This is how the blue-HB effect is introduced in the stellar evolution models. In this Section I used isochrones that have a larger mass-loss parameter  $\eta$  which alters the Reimers mass-loss relation (Reimers, 1975). The standard BaSTI+ isochrones used throughout this work assume  $\eta=0.2$  whereas the blue-HB isochrones have  $\eta=0.4$ . I use a blue HB isochrone for a 13.5 Gyr,  $[\text{Fe}/\text{H}]=-1.8$ ,  $\alpha$ -enhanced population.

Figures 4.8 and 4.9 show the theoretical index-index diagrams in the optical and infrared respectively. The PSMs were constructed for four ages: 5, 7, 10 and 13.5 Gyr, represented with different symbols; and for each metallicity colour-coded as indicated in the top panel of each figure. The coloured lines join SSPs with the same age and metallicity and varying IMF. The IMF variations hold the same throughout this work: Kroupa MW-IMF, Salpeter,  $x = 3.0$  and  $x = 3.5$ . Each point on the plots represents an SSP with a given age, metallicity and IMF. All the indices in these figures are to some extent IMF-sensitive and in all plots the strength of the indices increase as the slope of the IMF steepens (becomes more bottom-heavy). I first discuss the behaviour of the standard PSMs in the diagrams and then I focus in the special cases (populations with dynamical evolution and blue HB).

The optical diagrams (Figure 4.8) are different combinations of the TiO bands with the index CaH1 which was found to be only sensitive to the dwarf stars in the population (Spiniello et al., 2014). For metal-rich populations (red and black lines) the best combinations that appear to separate more cleanly the effects of age and IMF slope are  $\text{TiO}_2$ -CaH1 and bTiO-CaH1. The aTiO index in the  $[\text{Fe}/\text{H}]=0$  models is mildly sensitive to the IMF and is very degenerate to age and metallicity, on the other hand in metal-poor populations (green and blue lines) it appears to be more sensitive to the IMF. In all the optical indices, as the metallicity decreases the effect of age decreases and the indices respond mainly to IMF variations alone. All the TiO lines are very sensitive to the metallicity of the population and the larger  $Z$ , the stronger the TiO lines. The CaH1 line on the other hand is less sensitive to the metallicity of the population

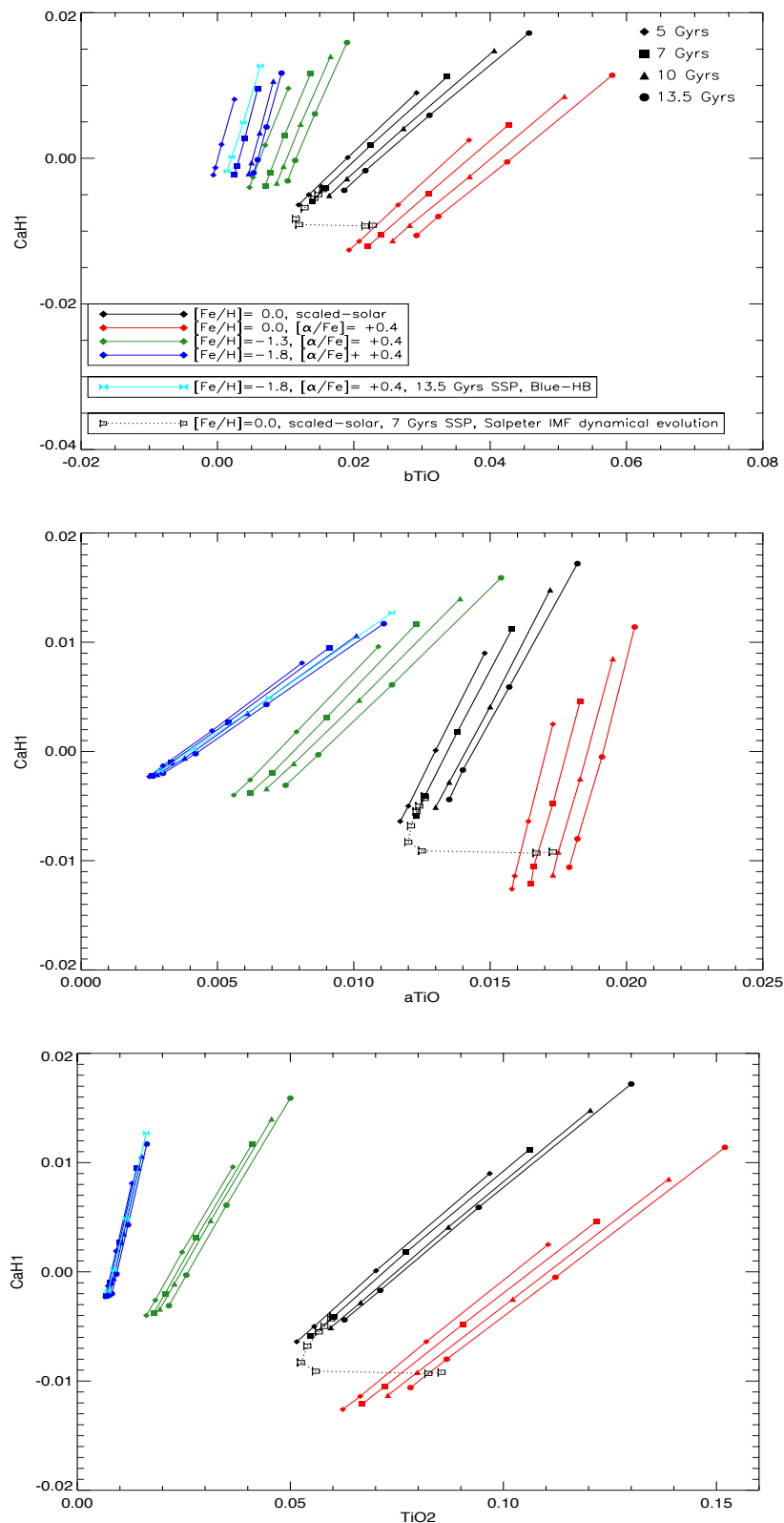


Figure 4.8: Optical index-index diagrams used to study the IMF. Each symbol represents an SSP with a given age, metallicity and IMF as indicated in the top panel. The dotted line indicates the effect of dynamical evolution on a 7 Gyr, solar metallicity SSP with Salpeter IMF. The cyan line indicates the effect of a blue HB in a 13.5 Gyr population with  $[\text{Fe}/\text{H}] = -1.8$ .

(this effect is also visible in Figure 3.3).

The infrared combinations (Figure 4.9) are based on the sodium lines NaD and NaI0.82, TiO<sub>2</sub> and the metallicity indicator [MgFe]. As with the TiO bands, all the infrared indicators are significantly sensitive to the total metallicity  $Z$  of the population. The TiO<sub>2</sub> feature is sensitive to the iron content of the population and increases with  $\alpha$ -enhancement as expected (Ti and O are both  $\alpha$ -elements). At fixed [Fe/H], NaI appears to be fairly insensitive to variations in the  $\alpha$ -elements (middle panel of Figure 4.9) and for [Fe/H]  $\leq -1$  it becomes less sensitive to the metallicity of the population. NaD decreases as [ $\alpha$ /Fe] increases. As in the optical diagrams, the infrared indices are sensitive to the age of the population at solar [Fe/H] but at lower metallicities it becomes very hard to distinguish between ages.

The effect of dynamical evolution is shown in Figures 4.8 and 4.9 with the dotted line indicating the value of the indices for specific disruption timescales. In this diagrams the predictions are for a range of disruption timescales from 5 to 100 Gyr to explore the effect of extreme situations. As expected the longer disruption timescale meets the prediction for the standard 7 Gyr, Salpeter IMF SSP in all plots. Following what was observed in Section 4.1.2, as the disruption timescales get shorter and approach the age of the cluster the indices become weaker and the predictions are shifted towards a ‘bottom-light’ IMF in all plots. However, as the disruption times continue to decrease, the effect on the predictions is less obvious. Shorter disruption times in the optical plots have the same effect in all three cases: the dynamically evolved population is shifted across the diagram mimicking the effect of a change in metallicity towards larger  $Z$  and an IMF heavier than Salpeter. The effect of shorter disruption times in the infrared diagrams is less systematic and it moves within the same metallicity grid towards the predictions for older populations. These are hypothetical situations since such short disruption timescales would happen in very violent environments and have not been observed. They are included in this analysis to show how the indices would be affected in such cases. Overall, if the age and metallicity of the population are well constrained, these diagrams can be used to predict the disruption timescale assuming the cluster has a standard (MW-Salpeter) IMF.

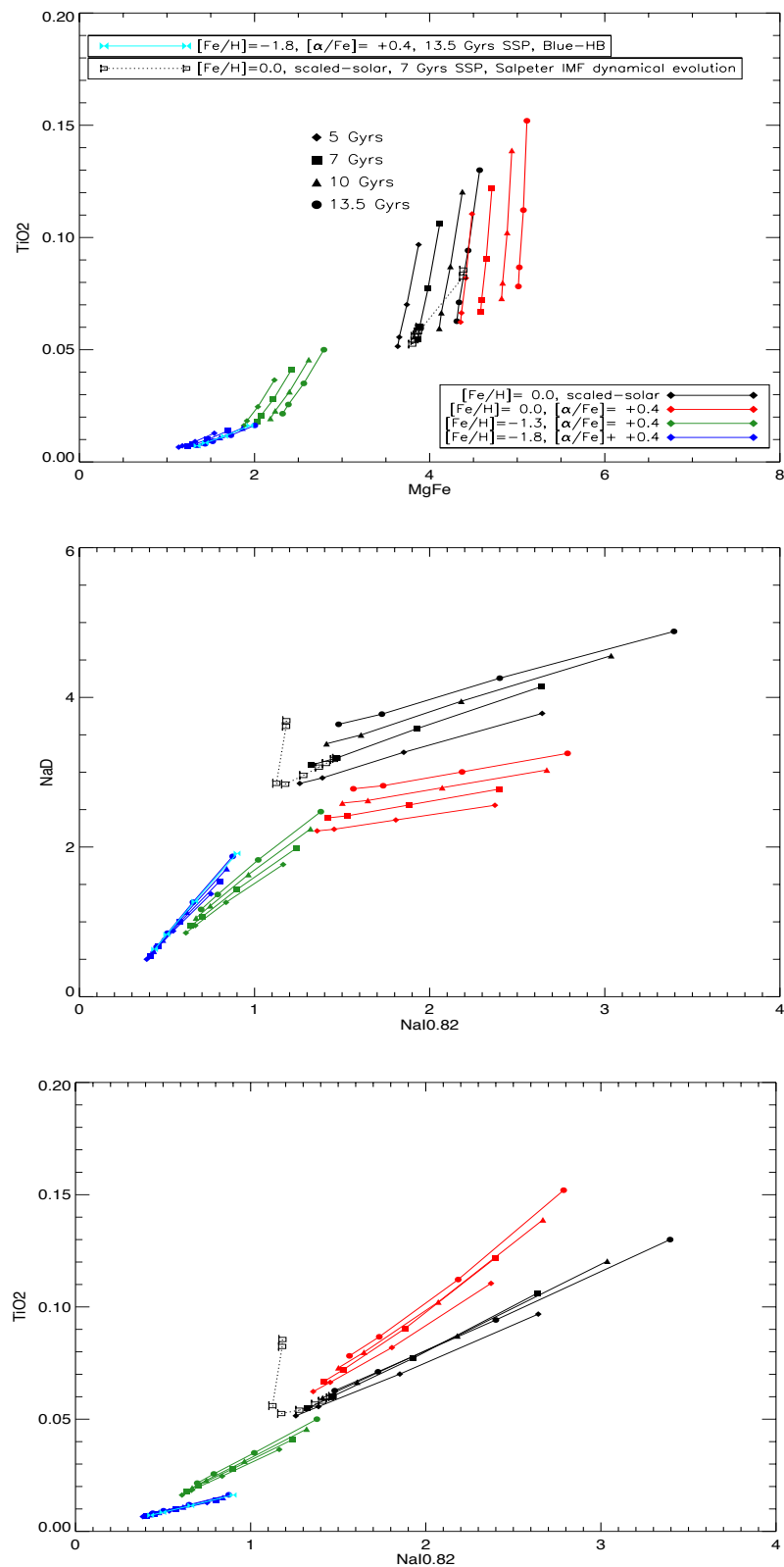


Figure 4.9: Infrared index-index diagrams used to study the IMF. Each symbol represents an SSP with a given age, metallicity and IMF as indicated in the top panel. The dotted line indicates the effect of dynamical evolution on a 7 Gyr, solar metallicity SSP with Salpeter IMF. The cyan line indicates the effect of a blue HB in a 13.5 Gyr population,  $[Fe/H] = -1.8$  for all IMFs.

The effect of the blue HB is shown in Figures 4.8 and 4.9 with the cyan line. The main effect of a blue HB on the SSPs is as expected, to appear younger than their true age (in the diagrams the cyan line is moved towards the predictions for standard HB models with younger ages  $\sim 10$  and 7 Gyr, see top panel of Figure 4.8). At fixed IMF an SSP with a blue-HB presents slightly stronger absorption lines compared to the standard SSP, but the effect is small. As was noted in the previous discussions, both optical and infrared diagrams show that as  $[\text{Fe}/\text{H}]$  decreases the effect of age is minimised and the indices respond mainly to IMF variations (the sensitivity to the IMF is also smaller than what is observed at higher metallicities). This means the effect of a blue HB is not important for IMF studies in populations with  $[\text{Fe}/\text{H}] \leq -1.0$ .

### **Present-day MF from the index-index plots**

In this section I use the optical and infrared combinations to study the present-day MF of the M31 clusters. Because of lack of knowledge of the total disruption times of the clusters and the unknown morphology of the HB, this analysis is based on the standard PSMs. The optical and infrared index-index combinations including the clusters are plotted in Figures 4.10 and 4.11, respectively. The clusters are colour-coded according to the original metallicity derived in C+2011. The cluster 115-177 with emission lines in its spectrum was removed from the solar  $[\text{Fe}/\text{H}]$  sample. The errors in the EWs were calculated using the program LECTOR.

In the  $b\text{TiO}-\text{CaH1}$  plane (top panel of Figure 4.10), the  $[\text{Fe}/\text{H}] = 0$  clusters (grey stars) lie between the two  $[\text{Fe}/\text{H}] = 0$  models (black and red lines) in agreement to what was observed in the  $\text{Fe}5406-[\text{MgFe}]$  plot (Section 4.1.1). Extrapolating from the available models, it seems that the clusters would lie close to SSPs with an IMF heavier than Salpeter. On the other hand, in the low metallicity regime the clusters (green and cyan stars) seem to be in better agreement with a standard IMF between Salpeter and MW-type. In the  $a\text{TiO}-\text{CaH1}$  (middle panel, same Figure) the solar- $[\text{Fe}/\text{H}]$  clusters present a huge scatter that cannot be explained by abundance effects. The  $a\text{TiO}$  abundances for these clusters are in disagreement with the metallicity predictions derived in Section

4.1.1. Most of the metal-poor clusters show aTiO abundances that are below the model predictions and the only two clusters that lie within the model grid are consistent with a standard IMF. Using TiO<sub>2</sub> and CaH1 (bottom panel) the [Fe/H]= 0 clusters are better fitted with the scaled-solar models which predict a bottom-heavy MF for most of them. The low-metallicity clusters are, again, better matched by a standard MF.

In the [MgFe]-TiO<sub>2</sub> plot (top panel of Figure 4.11) the solar-[Fe/H] clusters are better matched by the scaled-solar models and appear slightly bottom-heavy with  $x = 3.0$ . At the intermediate metallicity (green stars), the clusters appear slightly more metal-poor than the predictions and is difficult to derive an estimate of their MF. For the most metal-poor clusters it is not possible to derive any conclusion given that the models show very little sensitivity to the IMF. In the middle and bottom panels, the clusters present a large scatter in NaI and NaD at all metallicities and they appear completely off the grid in the NaI-NaD and NaI-TiO<sub>2</sub> plots. A possible explanation for this scatter is that these clusters have abundance anti-correlations. Coelho, Percival & Salaris (2011) used PSMs to study the impact of abundance anti-correlations on Lick-type indices in old SSPs and found that when the second generation of stars had an increased Na abundance with respect to a first generation with an  $\alpha$ -enhanced mixture, the NaD index was strongly affected and larger NaD strengths were observed. To explore this possibility, Figure 4.12 shows the behaviour of the clusters in NaD with respect to the total metallicity. Effectively, the clusters appear to have stronger NaD than are predicted by the models. The models have a standard metal distribution that represents the observed values in halo field stars. In a cluster with abundance anti-correlations, the sodium abundance from the models corresponds to the lowest sodium levels present in the clusters (where some of the stars have higher [Na/Fe]). On the other hand, NaI presents weaker strengths when compared to the models. The behaviour of this index in the presence of Na anti-correlations is not known but from what is seen in Figure 4.11, it appears that NaI is weaker in clusters with strong NaD (at least at solar [Fe/H]). I conclude that it is not possible to derive any IMF estimate for the clusters using NaI-NaD and NaI-TiO<sub>2</sub> unless the PSMs are able to model Na-enhancement.

Overall, in the optical and infrared the clusters present some scatter and inconsistencies

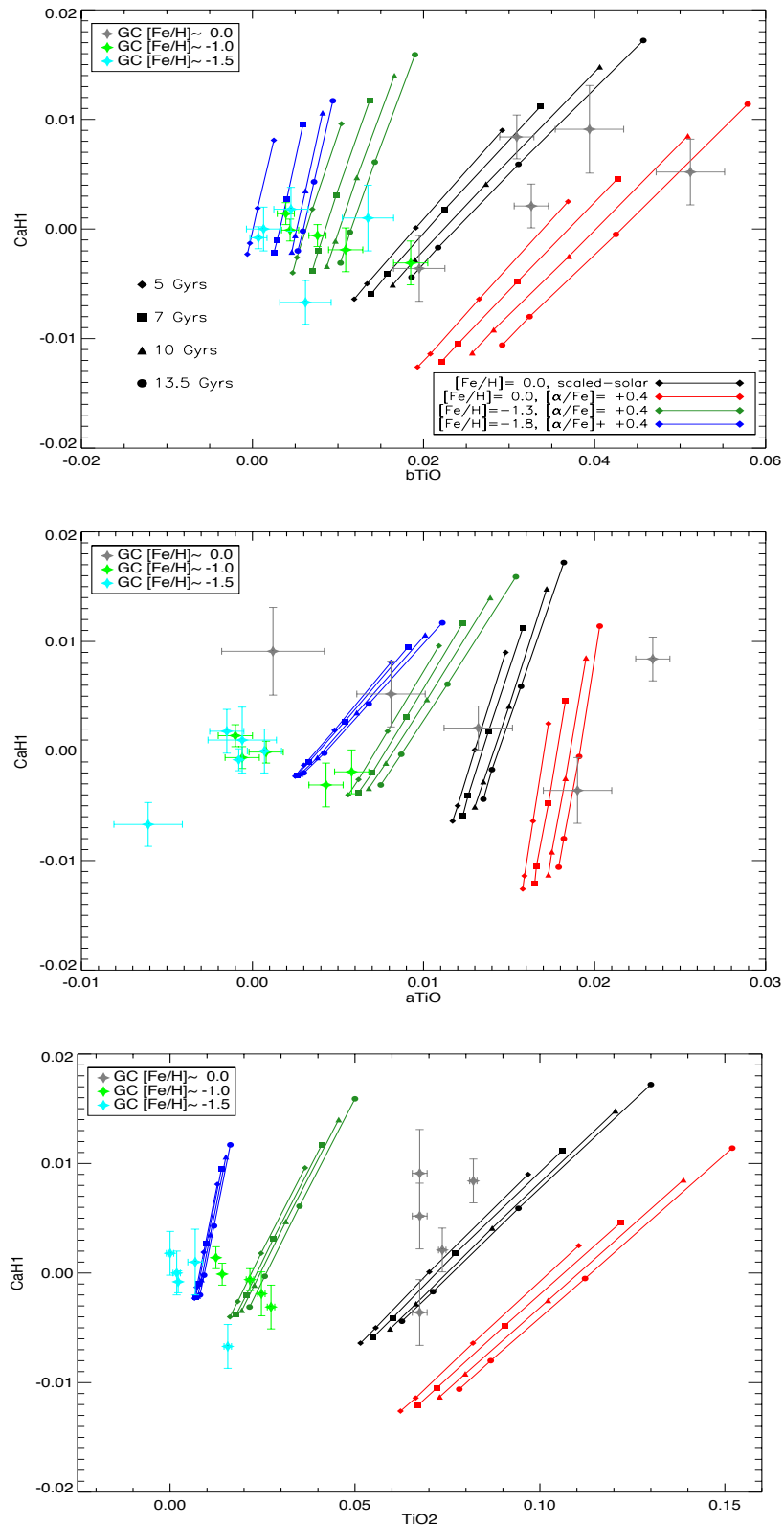


Figure 4.10: Optical index-index diagrams used to study the IMF of the M31 GCs. The models are labeled in the top panel and the clusters are colour-coded as indicated in each plot. The lines join SSPs with the same age and varying IMF. Each symbol from the model grid represents an SSP with a given age, metallicity and IMF as indicated in the top panel.

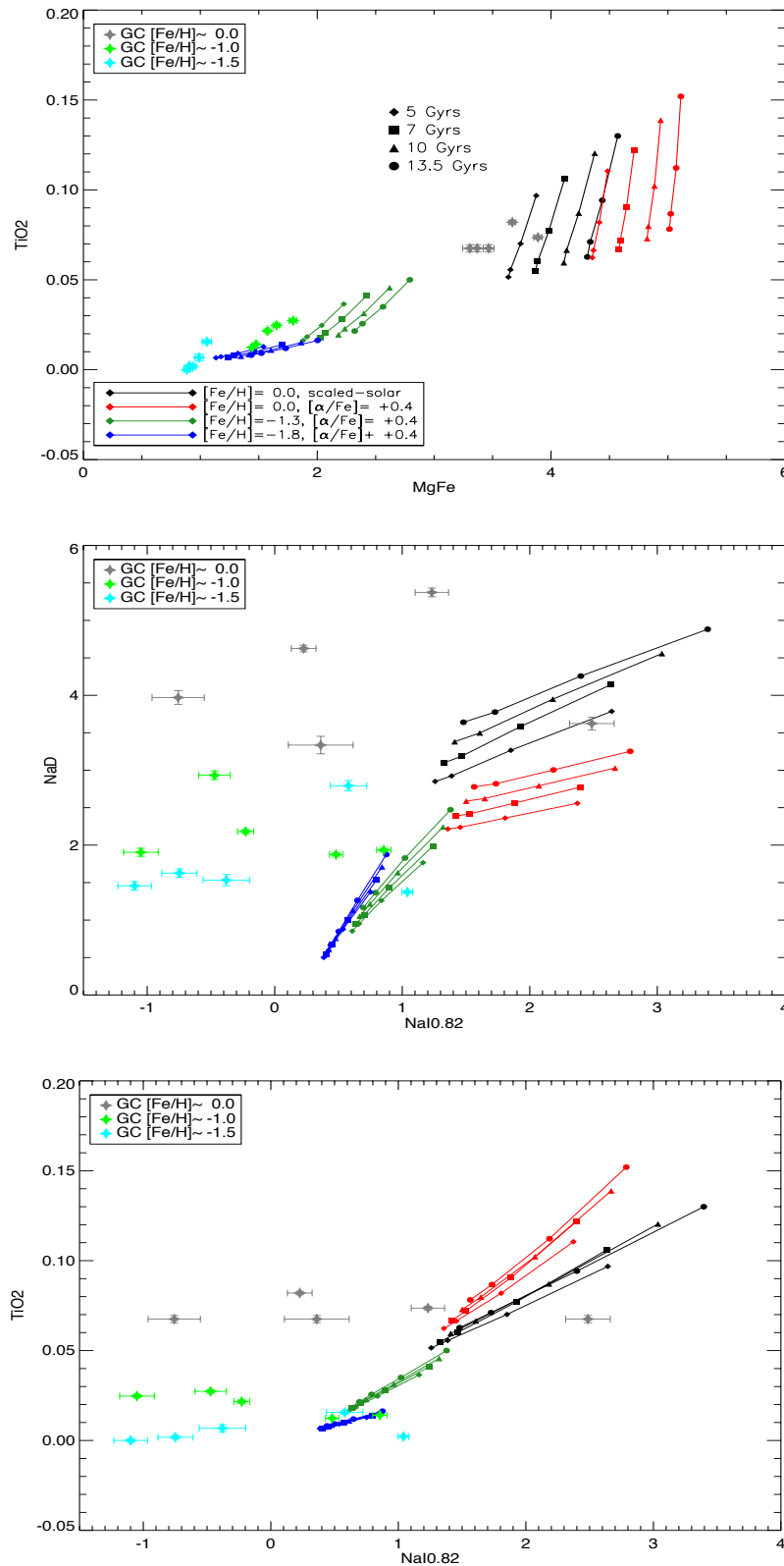


Figure 4.11: Infrared index-index diagrams used to study the IMF of the M31 GCs. The models are labeled in the top panel and the clusters are colour-coded as indicated in each plot. The lines join SSPs with the same age and varying IMF. Each symbol from the model grid represents an SSP with a given age, metallicity and IMF as indicated in the top panel.

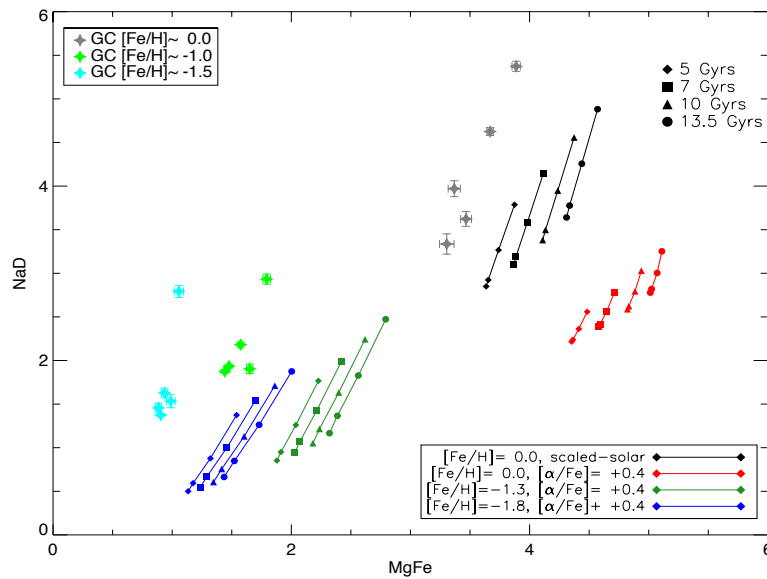


Figure 4.12: NaD and [MgFe] for the models and clusters colour-coded as indicated in the figure. Models with the same age are joined with a line and each point specifies an SSP with a characteristic age and IMF. Steeper IMF slopes always produce larger NaD values.

with the derived metallicities. This could be due to chemical anomalies in the clusters or simply due to inadequacies in the models to reproduce the observed abundances. In any case, the dynamical states and chemical abundances of the clusters are fundamental unknowns that could explain some of the scatter observed in Figures 4.10 and 4.11. Some indices suggest that the solar-[Fe/H] clusters may have MFs that mimic a bottom-heavy IMF. This result is rather surprising given that these clusters most certainly have undergone some kind of dynamical evolution and have lost a substantial fraction of the low-mass stars. On the other hand, the sub-solar clusters are in better agreement with MF close to Kroupa and Salpeter.

The conclusion that the metal-rich clusters may have a bottom-heavy IMF is unrealistic because these old clusters are expected to have evolved dynamically and therefore have lost a substantial fraction of the original dwarf population. This result suggests that there is some systematic effect that makes the spectra appear bottom-heavy. Under-prediction of the line strengths by the modelled spectra may explain why I observe this result.

The index-index combinations used in this section were originally chosen to determine

the IMF in ETGs from their integrated spectra and they have never been used before to study GCs. This analysis has shown that deriving an estimate of the MF for GCs using the same technique is very difficult. GCs are regarded as ideal laboratories to calibrate PSMs but their dynamical and chemical evolution are still rather complex and require a complex modelling of their integrated spectra.

## 4.2 Comparison with early-type galaxies

The previous analysis of GCs proved to be complicated given the number of uncertainties regarding their dynamical evolution and chemical abundances. In this section I analyse a sample of early-type galaxies (ETGs) that has been studied in Spiniello et al. (2014) using other PSMs. Their paper focused on IMF determinations using index-index plots of the optical IMF-sensitive features already studied in this thesis. The PSMs used in the original study are those from Conroy & van Dokkum (2012a) (hereafter CvD12). In this section I reanalyse the data using the PSMs from this thesis and compare the new predictions with those from the other models.

### 4.2.1 The data

The data used in this section are all published and were kindly provided by C. Spiniello (private communication). The data was selected from a sample of red early-type galaxies (ETGs) from the Sloan Digital Sky Survey (Aihara et al., 2011). The galaxies have a redshift  $z \leq 0.05$  and little ongoing star formation (Star Formation Rate,  $\text{SFR} < 0.3 M_{\odot} \text{ yr}^{-1}$ ). All galaxies with emission lines around  $\text{H}\beta$  were removed. The data were stacked together into five velocity dispersion bins between 150 and 310  $\text{kms}^{-1}$ . The spectra were stacked to improve the final signal-to-noise (S/N) to  $\sim 300$  per  $\text{\AA}$  in the wavelength range between 4000 and 7000  $\text{\AA}$ . In both cases, I only have the index measurements from the spectra and not the individual flux distributions.

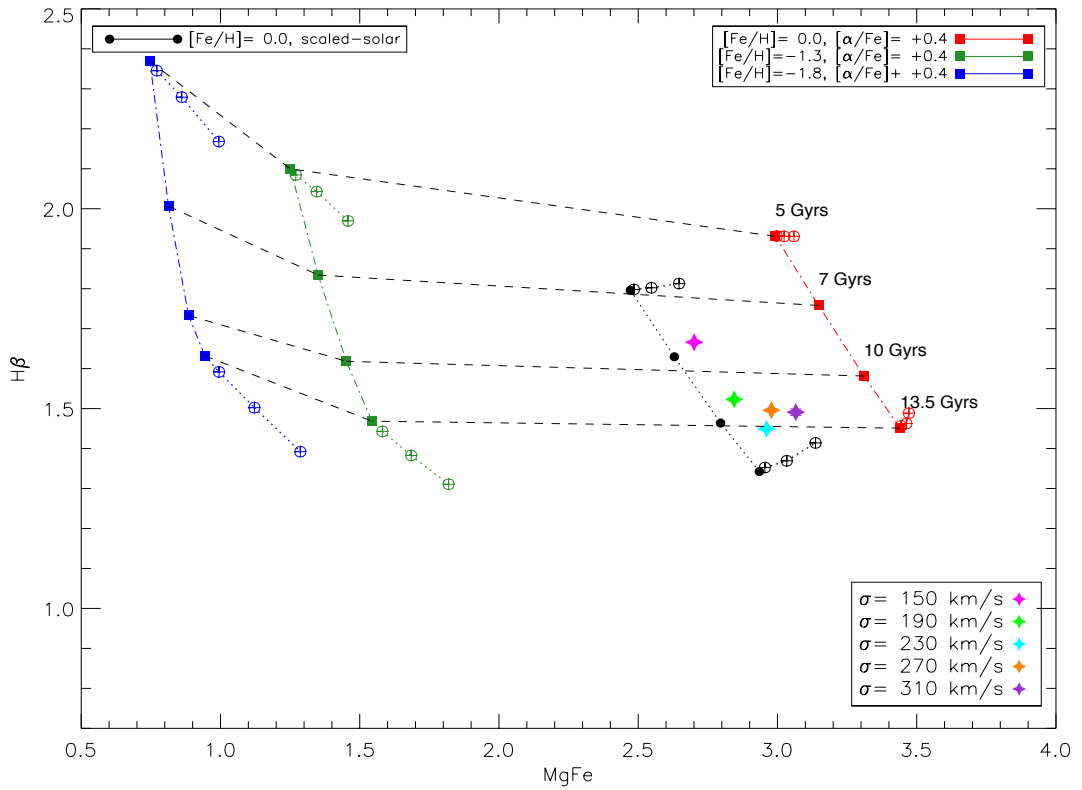


Figure 4.13: Age and metallicity grid for the sample of ETGs. The data is colour-coded according to the velocity dispersion  $\sigma$  and the colour-scheme of the models is indicated in the plot. The circles with the crosses inside indicate the effect of changing the IMF from MW-type to bottom-heavy ( $x=3.5$ ).

## 4.2.2 Age and metallicity estimates

As in the GC analysis, in order to derive IMF estimates for the populations I initially determine their ages and metallicities. I use the classical combination  $H\beta$  and  $[MgFe]$  already discussed in the GC analysis. Figure 4.13 shows the distribution of the stacks in this plane. The grid of models is constructed in the same way as in the GCs. All the spectra (both data and models) have been convolved to  $\sigma \sim 350 \text{ km s}^{-1}$  to match the resolution of the systems with the highest velocity dispersion. Each grid point represents an SSP with a given age and metallicity and a Kroupa IMF. IMF variations are explored for some of the SSPs and are indicated by the circles with the crosses inside. The data are stacked into five velocity dispersion bins= 150, 190, 230, 270 and 310  $\text{ km s}^{-1}$  colour-coded as indicated in the Figure.

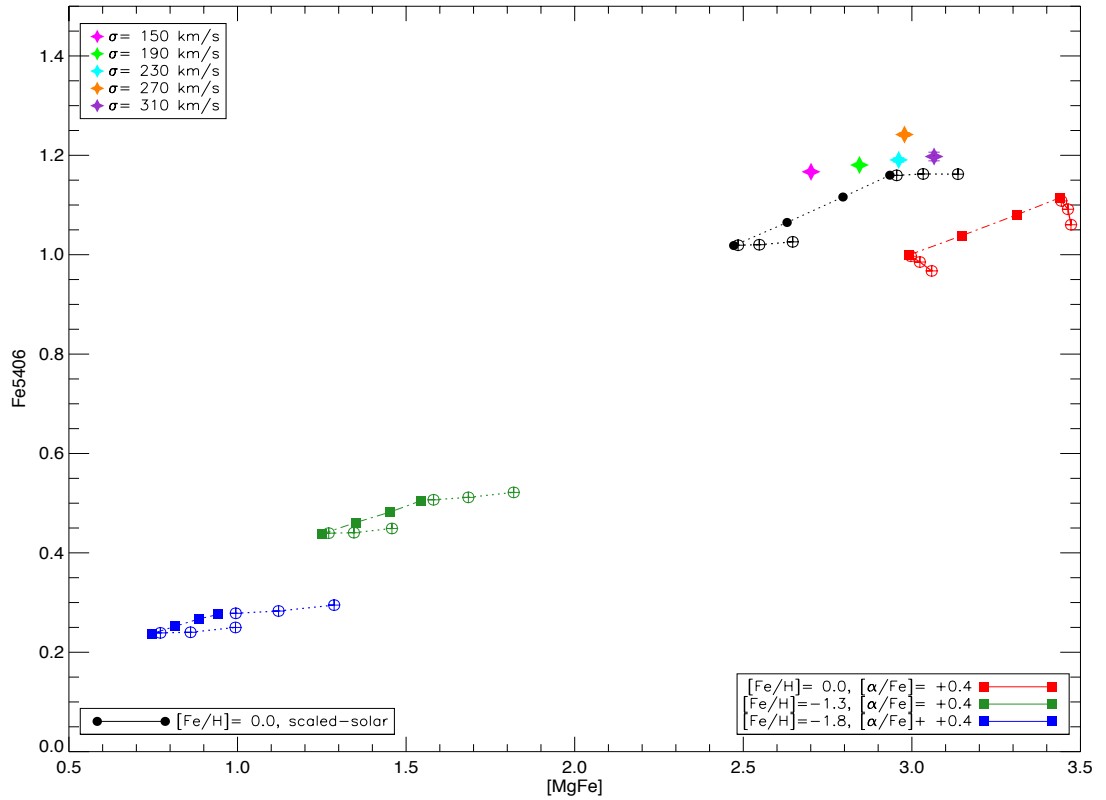


Figure 4.14: To study the  $\alpha$ -enhancement of the stacks. The colour-scheme of the models is described in the bottom panel. The circles with the crosses inside indicate the effect of changing the IMF from MW-type to bottom-heavy ( $x=3.5$ ).

Figure 4.13 shows that all the stacks appear to the right of the scaled-solar models which can be interpreted as an enhancement of the  $\alpha$ -elements or a slightly super-solar  $[\text{Fe}/\text{H}]$  for all systems. This Figure suggests that as  $\sigma$  increases, the metallicity of the population also increases.

To explore further the metallicity of these systems, Figure 4.14 shows the Fe5406-[MgFe] combination to distinguish  $\alpha$ -enhanced from scaled-solar populations. The stacked spectra appear close to the scaled-solar models and none of the stacks except the most massive ( $\sigma=310 \text{ km s}^{-1}$ ) are  $\alpha$ -enhanced according to this plot. This result is in disagreement to what was observed in  $\text{H}\beta$ -[MgFe].

The metallicity estimates derived from the  $\text{H}\beta$ -[MgFe] and the Fe5406-[MgFe] plots present some inconsistencies. Assuming that Fe5406-[MgFe] is the best combination to study the metallicity, I conclude that all the stacks are consistent with  $[\text{Fe}/\text{H}]\sim 0$  and

only the galaxies with  $\sigma \sim 300 \text{ km s}^{-1}$  are slightly  $\alpha$ -enhanced.

In Figures 4.13 and 4.14, the effects of IMF variations are shown for the oldest and youngest ages at each metallicity. The standard models assume a MW-IMF and the varying IMFs are represented with the circles with crosses inside. IMF variations are shown for a Salpeter,  $x = 3.0$  and  $x = 3.5$  slope. At any metallicity, a steepening of the IMF slope (larger fraction of low-mass stars) strengthens the measured [MgFe] value and affects the estimated metallicity of the population. As a result, at fixed [Fe/H] an SSP with  $x = 3.5$  will appear to have a larger total metallicity  $Z$  than the same population with a MW-IMF. In Figure 4.13 the effect of IMF variations on the scaled-solar models mimics the effect of  $\alpha$ -enhancement. The same effect is seen in Figure 4.14. This effect provides an alternative explanation for the  $\sigma \sim 300 \text{ km s}^{-1}$  stack; these galaxies might have a more ‘bottom-heavy’ IMF than the MW rather than a slight enhancement of the  $\alpha$ -elements.

The ages predicted by the models from the  $H\beta$  line are the luminosity-weighted values, and are lower limits to the ‘true’ population ages because they are biased by the presence of younger stars which are very bright and contribute more to the Balmer lines than older, more evolved stars (Trager et al., 2000). All the stacked spectra appear to be consistent with a roughly constant age between 10 and 13.5 Gyr, except for the  $\sigma = 150 \text{ km s}^{-1}$  stack that is  $\sim 7$  Gyr. Spiniello et al. (2014) found an increase in age with velocity dispersion.

### 4.2.3 IMF derivations and comparison to previous studies

In this section I use the optical combinations discussed in the GC section to estimate the IMF of the ETG samples. Figure 4.15 shows the model predictions in the optical compared to the data from Spiniello et al. (2014). In all the plots the lines indicate constant age (symbols) and metallicity (colours) and varying IMF (the IMF becomes more bottom-heavy as the index strengths increase). The analysis is restricted to the optical indices because there were the only indices available for the data set.

In this section I also compare the new estimates with the published results that are based on CvD12 models. The main ingredients of the CvD12 models are: a combination of stellar isochrones from the Dartmouth (Dotter et al., 2008), Padova (Marigo et al., 2008) and Lyon (Baraffe et al., 1998) libraries; and a combination of the spectral libraries MILES (optical, between 3500 and 7400 Å) and IRTF (infrared, between 8100 and 24000 Å). The IMF variations employed are the same as in Spiniello et al. with the only difference that I use a Kroupa IMF where they use a Chabrier-type.

### Optical indices

The optical combinations are shown in Figure 4.15. Since the previous analysis has shown that the stacks appear to have solar  $[\text{Fe}/\text{H}]$ , only the model predictions for  $[\text{Fe}/\text{H}] = 0$  scaled-solar and  $\alpha$ -enhanced abundances are included in the plots. The ages have different symbols and the metallicities are colour coded as indicated in the captions in the top panel.

The top panel of Figure 4.15 shows the bTiO-CaH1 indices. All the stacks appear closer to the youngest ages of the  $\alpha$ -enhanced population and are better modelled by a very bottom-heavy IMF ( $x = 3.5$ ). In the aTiO-CaH1 plot (middle panel), the stacks exhibit strong aTiO lines in comparison to what is predicted by the  $\alpha$ -enhanced models. The aTiO and bTiO strengths observed are more consistent with  $\alpha$ -enhanced mixtures and disagree with the previous conclusion that the stacks match scaled-solar abundances at  $[\text{Fe}/\text{H}] = 0$ . In TiO<sub>2</sub>-CaH1 (bottom panel) the stacks are better fitted by the scaled-solar models, in agreement with the metallicity estimates from Section 4.2.2, and they predict an IMF with  $x \sim 3.0$ .

It is possible that the models do not represent well the aTiO feature. In Chapter 3 aTiO was found to be the weakest feature and the least sensitive to IMF variations from all the IMF-indices. If that is the case and the scaled-solar predictions were to be shifted in the aTiO-CaH1 plane so that they overlap with the observations, then the stacks would be consistent with an IMF exponent  $\sim x = 3.0$ . Spiniello et al. (2014) found that the CvD12 PSM predict a steepening of the IMF (shift towards bottom-heavy slopes) that

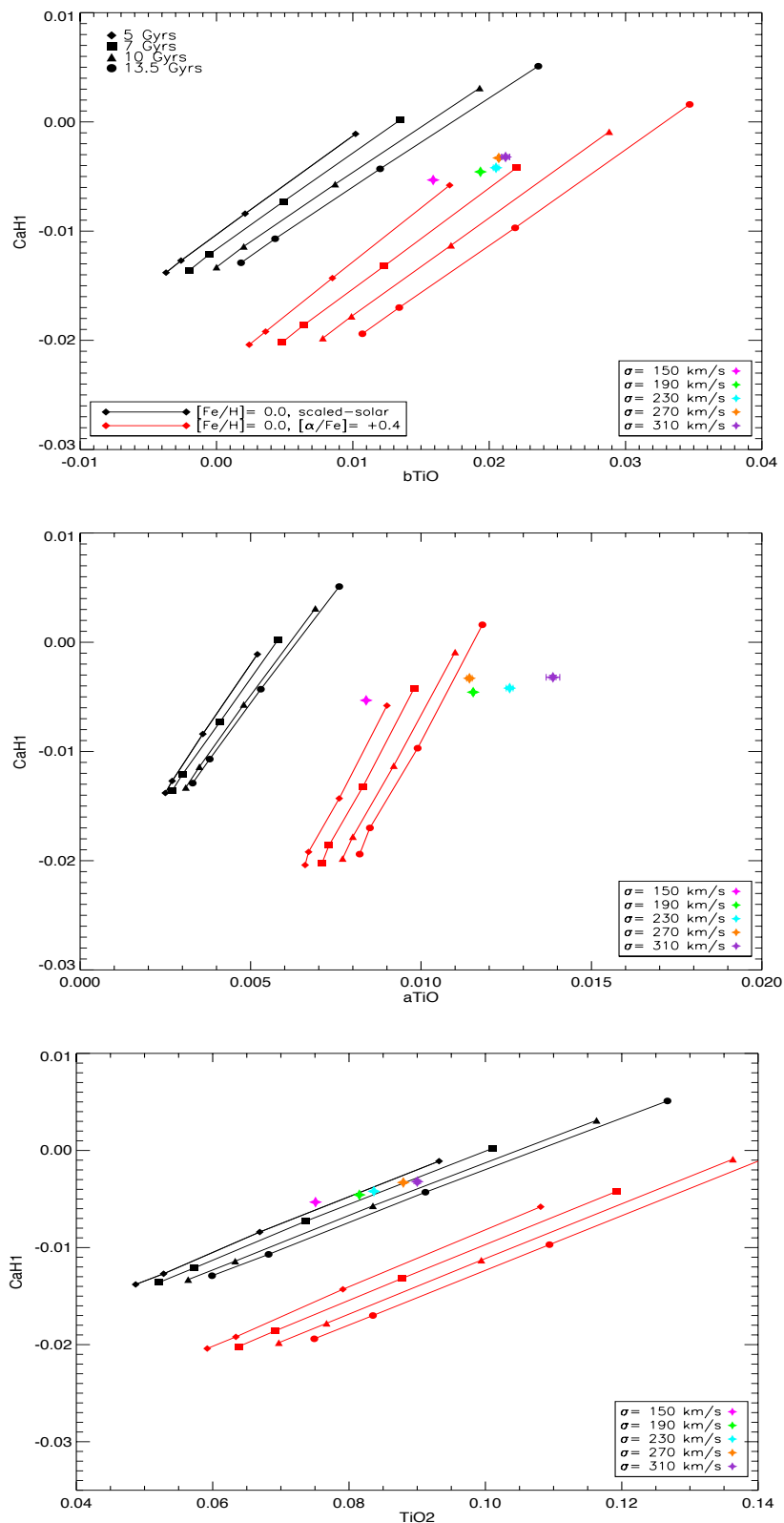


Figure 4.15: Optical index-index diagrams used to study the IMF of the stacks. The age symbols and colour-scheme of the models are described in the bottom panel. Only  $[\text{Fe}/\text{H}]=0$  models are shown for scaled-solar and  $\alpha$ -enhanced metal mixtures. The lines join SSPs with the same age and varying IMF. The error bars in the stacks are smaller than the symbol size.

correlates with galaxy mass or velocity dispersion,  $\sigma$ . With the PSMs from this work, CaH1 varies more due to IMF variations than the differences observed between stacks of different velocity dispersion. I do not find a significant variation of IMF with galaxy mass.

The overall result is that in all cases (despite the metallicity) the stacks are better fitted by a bottom-heavy IMF. In order to be consistent with the metallicity estimates derived previously, I conclude that in my models the best optical diagram to study the IMF is CaH1-TiO<sub>2</sub>. In Spiniello et al. (2014) the stacks appear to be slightly  $\alpha$ -enhanced in all the optical diagrams. In this work I based my conclusions trusting the predictions from H $\beta$ -[MgFe] and Fe5406-[MgFe] which have been used extensively and are well understood. In the GC analysis, this was also the only optical combination that was consistent with the metallicity estimates of the clusters.

### 4.3 Summary and conclusions

In this chapter I applied the PSM predictions to study the IMF of globular clusters and early-type galaxies. In this type of study the first step is always to derive estimates of the ages and metallicities of the populations. In every case I used H $\beta$ -[MgFe] and Fe5406-[MgFe] to explore the metallicities. The IMF was studied using the optical and infrared combinations discussed in the literature.

- **Ages and metallicities of the GCs.** I was able to derive ages and metallicities for most of the M31 GCs in the sample. I compared the results to the estimates from C+2011 when possible. I found that the solar-[Fe/H] sample appears younger than the original estimates. These predictions could be modified towards older ages if the metallicities of these clusters are better matched by models with a slightly sub-solar [Fe/H] and  $\alpha$ -enhancement. At lower [Fe/H] the clusters appear to have increasingly younger ages, this might be due to the presence of blue HB stars.

- **Dynamical evolution.** I studied the effect of dynamical evolution in the individual IMF-sensitive indices and in the overall model predictions when plotted in the index-index diagrams. Disruption timescales  $\leq 20$  Gyr modify the IMF of the population and it appears ‘bottom-light’ when retrieved with the original models. Dynamical evolution predictions can be used as long as the age and metallicity of the population are well constrained.
- **Blue HB.** The effect of a blue HB was tested on 13.5 Gyr population with  $[\text{Fe}/\text{H}] = -1.81$  assuming different IMFs. The effect was studied in the index-index plots. At this metallicity the indices are almost insensitive to the age of the population and the effect of a blue HB is not important.
- **IMFs of the M31 GCs.** The index-index diagrams in the optical suggest that the solar- $[\text{Fe}/\text{H}]$  clusters may have IMFs that are better matched with models that have IMFs heavier than Salpeter. The lower metallicity clusters appear to be consistent with standard IMF models (MW-type, Salpeter). In the infrared diagrams I found that the sodium indices are affected by the chemical anti-correlations. At low metallicities the infrared indices are only mildly sensitive to the IMF and it is difficult to derive IMF estimates for these clusters.
- **Ages and metallicities of the ETGs.** I used index measurements made on a sample of ETGs. Ages older than 10 Gyr are consistent with all the stacks except the least massive one which appears to be  $\sim 7$  Gyr. Their metallicities are best matched by models with  $[\text{Fe}/\text{H}] = 0$  and scaled-solar abundances. The most massive systems are slightly  $\alpha$ -enhanced.
- **IMFs of the ETGs.** Using the optical combinations of IMF-sensitive indices, in the  $\text{TiO}_2$ -CaH1 diagram (which is the best to study the IMF) the stacks appear to be bottom-heavy and  $x = 3.0$ . The strengths of aTiO in the models are probably under predicted.

# Chapter 5

## Summary & Conclusions

### 5.1 Summary

Population synthesis models are fundamental tools to study the star formation history of unresolved stellar populations. Using high resolution integrated spectra it is possible to constrain ages and metallicities of the underlying stellar population using absorption lines. In the last decades this technique has been extended to study the IMF. The theory of star formation cannot predict the shape of the IMF for a stellar population of a given age and metallicity. IMF determination remains an open problem in astronomy and great efforts are been made to try to constrain its shape in different stellar systems. An increasing number of studies are using PSMs and spectral features that are mainly sensitive to dwarf stars to determine the IMF of ETGs.

The principal aim of this work has been to construct new PSMs coupling theoretical isochrones to theoretical spectral libraries. The main application of these models is to perform IMF studies. To construct the models I explored the suitability of three theoretical libraries available from the literature. I used Lick-type indices and IMF-sensitive features to test the theoretical predictions from the libraries against observations of individual stars in the solar neighbourhood. I selected two libraries to cover the parameter space. I chose the BT-Settl library to sample the cool dwarfs in the low

main sequence and the Munari library to sample the rest of the evolutionary phases. The BaSTI+ isochrones were selected because they had been extensively tested against empirical CMDs of MW GCs and in other PSM predictions. I constructed PSMs for old SSP with ages between 5 and 13.5 Gyrs and  $[Fe/H]= 0, -1.31$  and  $-1.81$  with scaled-solar and  $\alpha$ -enhanced metal mixtures.

I studied the behaviour of indices that have been used in the literature as IMF indicators. I explored the sensitivity of these IMF features to age and metallicity with the new PSMs and tested the effect of uncertainties in the models (effective temperature and stellar evolution predictions). I explored which evolutionary phases are the main contributors to the individual index strengths.

In the last chapter I introduced the final application of the PSMs to derive IMF estimates in GCs and ETGs. The general procedure for this type of study is to first derive estimates for the ages and metallicities of the populations because the IMF indices are also sensitive to these parameters. The classical  $H\beta$ - $[MgFe]$  combination produces an excellent grid to separate age and metallicity effects. With respect to the metallicity, it is very important to determine the metal abundances and the best index-index plot to do that is  $Fe5406$ - $[MgFe]$ .

The GC analysis in this framework of IMF studies is completely novel. I explored the main issues regarding the modelling of GCs (HB morphology and dynamical evolution) and applied these uncertainties in the final model predictions. The model predictions were discussed using index combinations that had already been studied in the literature. The index-index plots combine IMF-sensitive features from the optical and infrared that try to disentangle the effects of age, metallicity and IMF slope. I used these diagrams to study the present-day MFs of the GCs using the standard PSMs. For the ETG analysis I used the same procedure in the optical regime with a data set from the literature.

## 5.2 Main results and conclusions

- BT-Settl is the best available theoretical spectral library to model the spectra of dwarf stars. The Munari library provides a good coverage of the parameter space and predicts the behaviour of the line indices in excellent agreement with the observed values.
- In the new PSMs all the optical and infrared features that have been defined in the literature as good IMF indicators, show a sensitivity to the IMF that is in agreement to what has been determined by other models.
- As expected, I found a strong degeneracy between age and metallicity in all indices and I emphasized the need to strongly constrain these parameters when applying PSMs to derive the IMF.
- The TiO bands and NaD are significantly affected by changes in the temperature of the isochrone. If the isochrones are cooler by  $\sim 150\text{K}$ , the strengths predicted by the models for these indices can mimic the effect of a bottom-heavy IMF in cases where the underlying population has a MW-type IMF. On the other hand, uncertainties in the temperature of the giants between 100 and 200K can produce values that lead to a misinterpretation of the IMF slope between a MW-type and Salpeter.
- An analysis of the effect of dynamical evolution on the individual indices showed that for disruption times  $\leq 20$  Gyrs, the IMF-indices match their predicted values for unevolved bottom-light IMFs.
- The effect of HB morphology in low  $[\text{Fe}/\text{H}]$  populations is negligible when studying the IMF in index-index plots.
- Using my PSMs the best optical combination to study the IMF is CaH1-TiO<sub>2</sub>. From these predictions, the IMF of the solar- $[\text{Fe}/\text{H}]$  GCs appear slightly bottom-heavy while the lower metallicity clusters are consistent with a standard IMF. Using this same combination the ETG stacks also appear to have bottom heavy

IMF. These are not conclusive results since the mismatches observed in the other index combinations should be explored further. At the time of writing this thesis, the available data and chemical abundances of the models did not allow these investigations.

- The infrared combinations used alone to study the IMF are not trustworthy because they are affected by sodium abundances which proved to be problematic in both GCs study. The sodium features appear to respond in different ways to changes in the sodium abundances.

### 5.3 Future work

- **Extend the range of chemical compositions.** It would be desirable to have a finer grid in the  $[\text{Fe}/\text{H}]$  range with models with  $[\text{Fe}/\text{H}] = \pm 0.5$  with scaled-solar and  $\alpha$ -enhanced abundances. At the same time, produce models that allow variations of the Na-abundances, since this issue appears to be crucial for the modelling of GCs and massive ETGs.
- **Explore the spectral regions of the IMF-sensitive indices where the models do not show good agreement with observed values.** Using empirical spectra of individual stars try to understand why the theoretical spectra fail to reproduce the strengths observed in FeH0.99. Using the same technique explore further the behaviour of all the optical IMF indices where it is not clear if the problems seen are due to the data or the PSMs.
- **Statistical Fluctuations.** The analytical integration of the IMF is only valid if the number of stars in the population is very large and every evolutionary phase is populated by at least one star. In reality clusters have lower masses and the later evolutionary phases (where stars evolve very rapidly) are poorly populated. This means that two SSPs with a fixed total mass can have their later evolutionary stages populated in very different ways and they will therefore produce two different integrated spectra. Statistical fluctuations affect mainly the post-

MS stars because along the main sequence the number of stars populating each evolutionary phase is much larger. It is possible to study the effect of statistical fluctuations on the integrated predictions using Monte-Carlo simulations. The effect on age and metallicity estimates has been studied in the literature but no one has yet explored the effect on the IMF-sensitive indices where the post-MS stars contribute mainly to the continuum.

- **Extend the grid of synthetic spectra to cover the tip of the RGB.** The available libraries did not cover these cool, low-gravity stars. These stars contribute significantly to the infrared emission in the integrated spectrum of a population and might explain some of the inconsistencies observed in the infrared indices.

# Bibliography

- Aihara, H., Allende Prieto, C., An, D., Anderson, S.F., et al. 2011, *ApJS*, 193, 29
- Asplund, M., 2005, *ARA&A*, 43, 481
- Alonso, A., Arribas, S. & Martínez-Roger, C., 1996, *A&ASS*, 117, 227
- Alonso, A., Arribas, S. & Martínez-Roger, C., 1996, *A&A*, 313, 873
- Alonso, A., Arribas, S. & Martínez-Roger, C., 1999, *A&AS*, 140, 261
- Allard, F., Homeier, D. & Freytag, B., 2012, *IAUS*, 282, 235
- Anders, P., Lamers, H.J.G.L.M., Baumgardt, H., 2009, *A&A*, 502, 817
- Arp, H.C., Baum, W.A. & Sandage, A.R., 1952, *ApJ*, 57, 4
- Baldry, I.K. & Glazebrook, K., 2003, *ApJ*, 593, 258
- Baraffe, I., Chabrier, G., Allard, F. & Hauschildt, P. H., 1998, *A&A*, 337, 403
- Baraffe, I., Chabrier, G., Allard, F. & Hauschildt, P., 2003, *IAUS*, 211
- Barber, R.J., Tennyson, J., Harris, G.J. & Tolchenov, R.N., 2006, *MNRAS*, 368, 1087
- Bastian, N., Covey, K.R. & Meyer, M.R., 2010, *ARA&A*, 48, 339
- Baugh, C.M., 2006, *Reports on Progress in Physics*, 69, 12, 3101
- Baumgardt, H. & Makino, J., 2003, *MNRAS*, 340, 227
- Bedin, L.R., Piotto, G., Anderson, J., King, I.R., Cassisi, S. & Momany Y., 2004, *Mem. S.A.It.Suppl.*, 5, 105

- Bennett, C.L., Bay, M., Halpern, M., Hinshaw, G., Jackson, C., Jarosik, N., Kogut, A., Limon, A., Meyer, S.S., Page, L., Spergel, D.N., Tucker, G.S., Wilkinson, D.T., Wollack, E. & Wright, E.L., 2003, *ApJ*, 583
- Bressan, A., Marigo, P., Girardi, L., Salasnich, B., Del Cero, C., Rubele, S. & Nanni, A., 2012, *MNRAS*, 427, 127
- Bruzual, G. & Charlot, S., 2003, *MNRAS*, 344, 1000
- Burrows, A., Marley, M., Hubbard, W. B., Lunine, J. I., Guillot, T., Saumon, D., Freedman, R., Sudarsky, D. & Sharp, C., 1997, *ApJ*, 491, 856
- Caffau, E., Ludwig, H.-G., Steffen, M., Freytag, B. & Bonifacio, P., 2011, *Sol. Phys.*, 268, 255
- Caldwell, N., Schiavon, R., Morrison, H., Rose, J.A. & Harding, P., 2011, *ApJ*, 141, 61
- Cappellari, M., McDermid, R. M., Alatalo, K., Blitz, L., Bois, M., Bournaud, F., Bureau, M., Crocker, A.F., Davies, R.L., Davis, T.A., de Zeeuw, P. T., Duc, P.-A., Emsellem, E., Khochfar, S., Krajnović, D., Kuntschner, H., Lablanche, P.-Y., Morganti, R., Naab, T., Oosterloo, T., Sarzi, M., Scott, N., Serra, P., Weijmans, A.-M. & Young, L.M., 2012, *Nature*, 484, 485
- Carretta, E. & Gratton, R.G., 1997, *A&AS*, 121, 95
- Carretta, E., Bragaglia, A., Gratton, R.G., D'Orazi, V. & Lucatello, S., 2009, *A&A*, 508, 695
- Carter, D., Visvanathan, N. & Pickles, A.J., 1980, *ApJ*, 311, 637
- Casagrande, L., Flynn, C. & Bessel, M., 2008, *MNRAS*, 389, 585
- Carpenter, J.M., 2001, *AJ*, 121, 2851
- Cassisi, S. & Salaris, M., 2013, *Old Stellar Populations: How to study the fossil record of galaxy formation.*

- Cassisi, S., Castellani, V., Ciarcelluti, P., Piotto, G. & Zoccali, M., 2000, MNRAS, 315, 679
- Cassisi, S., Salaris, M. & Pietrinferni, 2013, Mem. S.A.It., 84, 91
- Cenarro, A. J., Cardiel, N., Gorgas, J., et al. 2001, MNRAS, 326, 959
- Cenarro, A. J., Cervantes, J.L., Beasley, M.A., Marin-Franch, A. & Vazdekis, A., 2010, IAU, 10, 1017
- Chabrier, G., Baraffe, I., Allard, F. & Hauschildt, P., 2000, A&A, 542,464
- Chabrier, G., 2003, PASP, 115, 763
- Coelho, P., Percival, S.M. & Salaris, M., 2011, ApJ, 734, 72
- Cohen, J., 1978, ApJ, 221, 788
- Conroy, C., 2013, ARA&A, 97
- Conroy, C. & van Dokkum, P.G., 2012, ApJ, 747, 69
- Conroy, C. & van Dokkum, P.G., 2012, ApJ, 760, 71
- Dabringhausen, J., Hilker, M. & Kroupa, P., 2008, MNRAS, 386, 864
- De Marchi, G., Paresce, F. & Zwart, S.P., 2010, ApJ, 718, 105
- Diaz, A. I., Terlevich, E., & Terlevich, R. 1989, MNRAS, 239, 325
- Dotter, A., Chaboyer, B., Jevremović, D., Kostov, V., Baron, E. & Ferguson, J. W., 2008, ApJSS, 178, 89
- Dutton, A.A., Mendel, J.T. & Simard, L., 2012, MNRAS, 422, 33
- Faber, S.M. & French, H.B., 1980, ApJ, 235, 405
- Ferreras, I., La Barbera, F., de la Rosa, I.G., Vazdekis, A., de Carvalho, R.R., Falcón-Barroso, J. & Ricciardelli, E., 2013, MNRAS, 429, L15
- Girardi, L., Bressan, A., Bertelli, G. & Chiosi, C., 2000, A&AS, 141, 371

- Golimowski, D. A., Leggett S. K., Marley, M. S., Fan, X., Geballe, T. R., Knapp, G. R., Vrba, F. J., Henden, A. A., Luginbuhl, C. B., Guetter, H. H., Munn, J. A., Canzian, B., Zheng, W., Tsvetanov, Z. I., Chiu, K., Glazebrook, K., Hoversten, E. A., Schneider, D. P. & Brinkmann, J., 2004, *ApJ*, 127, 3516
- Gratton, R., Sneden, C. & Carretta E., 2004, *ARA&A*, 42, 385
- Gratton, R., Carretta, E. & Bragaglia, A., 2012, *A&AR*, 20, 50
- Gratton, R., Lucatello, S., Carretta, E., Bragaglia, A., D’Orazi, V., Al Momany, Y., Sollima, A., Salaris, M. & Cassisi, S., 2012, *A&A*, 539, A19
- Grevesse, N., Noels, A. & Sauval, A.J., 1993, *A&A*, 271, 587
- Grevesse, N. & Sauval, A. J., 1998, *Space Sci. Rev.*, 85, 161
- Gustafsson, B., Edvardsson, B., Eriksson, K., Jorgensen, U. G., Nordlund, Å. & Plez, B., 2008, *A&A*, 486, 951
- Hauschildt, P.H., Allard, F. & Baron, E., 1999, *ApJ*, 512, 377
- James, P.A., Salaris, M., Davies, J.I., Phillipps, S. & Cassisi, S., 2006, *MNRAS*, 367, 339
- Jeong, H., Yi, S.K., Kyeong, J., Sarzi, M., Sung, E-C., Oh, K., 2013, *ApJS*, 208, 7
- Jones, L. A., 1999, Ph.D. thesis, Univ. North Carolina
- Kennicutt, R.C., 1989, *ApJ*, 344, 685
- Kennicutt, R.C., 1998, *ASPC*, 142
- Kroupa, P., Tout, C.A. & Gilmore, G., 1993, *MNRAS*, 262, 545
- Kroupa, P., 2001, *MNRAS*, 322, 231
- Kruijssen, J.M.D., 2008, *A&A*, 486, L21
- Kruijssen, J.M.D. & Mieske S., 2009, *A&A*, 500, 785

- Kurucz, R.L., 1970, Smithsonian Astrophysical Observatory Special Report, 309
- Kurucz, R.L., 1979, *ApJSS*, 40, 1
- Kurucz, R.L., 1992, *AAS*, 24, 779
- Lamers, H.J.G.L.M, Anders, P. & de Grijs, 2006, *A&A*, 452,131
- Le Borgne, J.-F., Bruzual, G., Pelló, R. , Lançon, A., Rocca-Volmerange, B., Sanahuja, B., Schaerer, D., Soubiran, C. & Vílchez-Gómez, R., 2003, *A&A*, 402, 433
- Lee, Y-W, Demarque, P. & Zinn, R., 1994, *ApJ*, 423, 248
- Lee, H-C, Yoon, S-J & Lee, Y-W, 2000, *ApJ*, 120, 998
- Marigo, P., Girardi, L., Bressan, A., Groenewegen, M.A.T., Silva, L. & Granato, G.L., 2008, *A&A*, 482, 3, 883
- Martins, L.P., González Delgado, R.M., Leitherer, C., Cerviño, M., Hauschildt, P., 2005, *MNRAS*, 358, 49
- Martins, L.P. & Coelho, P., 2007, *MNRAS*, 381, 1329
- Miller, & Scalo, J.M., 1979, *ApJSS*, 41, 513
- Munari, U., Sordo, R., Castelli, F. & Zwitter, T., 2005, *A&A*, 442, 1127
- Navarro, J. F., Frenk, C. S. & White, S. D. M., 1996, *ApJ*, 462, 563
- Ohman, Y., 1934, *ApJ*, 80, 1710
- Percival, S.M., Salaris, M., Cassisi, S. & Pietrinferni, A., “A large stellar evolution database for population synthesis studies. IV Integrated properties and spectra”, 2009, *ApJ*, 690, 427
- Percival, S.M. & Salaris, M., 2011, *MNRAS*, 412, 2445
- Pietrinferni, A., Cassisi, S. & Salaris, M., 2004, *ApJ*, 612, 168
- Piotto, G., 2009, *IAUS*, 258, 233

- Plez, B., 1998, *A&A*, 337, 495
- Rabin, D., 1982, *ApJ*, 261, 85
- Rajpurohit, A.S., Reylé, C., Schultheis, M., Leinert, Ch., Allard, F., Homeier, D., Ratzka, T., Abraham, P., Moster, B., Witte, S. & Ryde, N., 2012, *A&A*, 545, 85
- Rajpurohit, A.S., Reylé, C., Allard, F., Homeier, D., Schultheis, M., Bessell, M.S. & Robin, A.C., 2013, *A&A*, 556, 15
- Rayner, J.T., Cushing, M.C. & Vacca, W.D., 2009, *ApJS*, 185, 289
- Reimers, D., 1975, *Mem. Soc. R. Sci. Liege*, 8, 369
- Riess, A.G., Nugent, P.E., Gilliland, R.L., Schmidt, B.P., Tonry, J., Dickinson, M., Thompson, R.I., Budavári, T., Casertano, S., Evans, A.S., Filippenko, A.V., Livio, M., Sanders, D.B., Shapley, A.E., Spinrad, H., Steidel, C.C., Stern, D., Surace, J. & Veilleux, S., 1998, *ApJ*, 560, 49
- Salaris, M. & Cassisi, S., 2005, *Evolution of Stars and Stellar Populations*, Wiley
- Salaris, M., Percival, S., Cassisi, S. & Pietrinferni, A., 2009, *Mem. S.A.It.*, 80, 387
- Salasnich, B., Girardi, L., Weiss, A., Chiosi, C., 2000, *A&A*, 361, 1023S
- Salpeter, E.E., 1955, *ApJ*, 121, 161
- Sánchez-Blázquez, P., Peletier, R.F., Jiménez-Vicente, J., Cardiel, N., Cenarro, A.J., Falcón-Barroso, J., Gorgas, J., Selam, S. & Vazdequis, A., 2006, *MNRAS*, 371, 703
- Sandage, A. & Wallerstein, G., 1960, *ApJ*, 131, 598
- Sandage, A. & Saha, A., 2002, *ApJ*, 123, 2047
- Sagar, R., 2002, *IAUS*, 207, 515
- Scalo, J.M., 1986, *FCP*, 11, 1
- Scalo, J., 2004, *ASSL*, 327, 23

- Schiavon, R.P., Barbury, B. & Singh, D., 1997, *ApJ*, 484, 499
- Schiavon, R.P., Barbury, B. & Bruzual, A., 2000, *ApJ*, 532, 453
- Schiavon, R.P., Rose, J.A., Courteau, S., & MacArthur, L.A., 2005, *ApJS*, 160, 163
- Schiavon, R., 2007, *ApJSS*, 171, 146
- Scwenke, D.W., 1998, *CPMGS*, 109, 321
- Silk, J., 1968, *ApJ*, 151
- Smith, R.J., Lucey, J.R. & Carter, D., 2012, *MNRAS*, 426, 2994
- Spiniello, C., Trager, S., Koopmans, L.V.E. & Chen, Y.P., 2012, *ApJ Letters*, 753
- Spiniello, C., Trager, S., Koopmans, L.V.E. & Conroy, C., 2014, *MNRAS*, 438, 1483
- Spinrad, H. & Taylor, B.J., 1971, *ApJSS*, 193, 445
- Tinsley, B.M., 1968, *ApJ*, 151, 547
- Trager, S.C., Worthey, G., Faber, S.M., Burstein, D. & González, J.J., 1998, *ApJSS*, 116, 1
- Trager, S.C., Faber, S.M., Worthey, G. & González, J.J., 2000, *ApJ*, 120, 165
- Trager, S.C. & Somerville, R.S., 2009, *MNRAS*, 395, 608
- Treu, T., Auger, M.W., Koopmans, L.V.E., Gavazzi, R., Marshall, P.J. & Bolton, A.S., 2010, *ApJ*, 709, 1195
- Valdes, F., Gupta, R., Rose, J.A., Singh, H.P. & Bell, D.J., 2004, *ApJS*, 152, 251
- van Dokkum, P.G. & Conroy, C., 2010, *Nature*, 468, 940
- van Leeuwen, F., 2007, *Ap&SSL*, 350
- Vazdekis, A., 2011, *ASCL*, 1104, 006
- Vazdekis, A., Ricciardelli, E., Cenarro, A.J., Rivero-González, Díaz-García, Falcón-Barroso, 2012, *MNRAS*, 424, 157

White, S.D.M. & Rees, M.J., 1978, MNRAS, 183

Worthey, G., Faber, S.M. & Gonzalez, J.J., 1992, ApJ, 398, 69

Worthey, G., 1994, ApJSS, 95, 107

Worthey, G., Faber, S. M., González, J. J. & Burstein, D., 1994, ApJS, 94, 687

Worthey, G. & Ottaviani, D. L., 1997, ApJS, 111, 377